PROTECTING EMBANKMENTS FROM EROSION USING WEDELIA TRILOBATA

MR. CHINNAKRIT OUNJAI

A THESIS SUBMITTED IN PARTIAL FULFILLMENT OF THE REQUIREMENTS
FOR THE DEGREE OF MASTER OF ENGINEERING IN
CIVIL ENGINEERING AND EDUCATION
DEPARTMENT OF WELDING ENGINEERING TECHNOLOGY
GRADUATE COLLEGE
KING MONGKUT'S UNIVERSITY OF TECHNOLOGY NORTH BANGKOK
ACADEMIC YEAR 2025

COPYRIGHT OF KING MONGKUT'S UNIVERSITY OF TECHNOLOGY NORTH BANGKOK

PROTECTING EMBANKMENTS FROM EROSION USING WEDELIA TRILOBATA

MR. CHINNAKRIT OUNJAI

A THESIS SUBMITTED IN PARTIAL FULFILLMENT OF THE REQUIREMENTS
FOR THE DEGREE OF MASTER OF ENGINEERING IN
CIVIL ENGINEERING AND EDUCATION
DEPARTMENT OF WELDING ENGINEERING TECHNOLOGY
GRADUATE COLLEGE
KING MONGKUT'S UNIVERSITY OF TECHNOLOGY NORTH BANGKOK
ACADEMIC YEAR 2025
COPYRIGHT OF KING MONGKUT'S UNIVERSITY OF TECHNOLOGY NORTH BANGKOK



Thesis Certificate

The Graduate College, King Mongkut's University of Technology North Bangkok

Title Protecting embankments from erosion using Wedelia trilobata

By Mr. Chinnakrit Ounjai

Accepted by the Graduate College, King Mongkut's University of Technology North Bangkok in Partial Fulfillment of the Requirements for the Master of Engineering in Civil Engineering and Education

..... Dean / Head of Department

(Assistant Professor Dr. Suphot Chunwiphat)

Thesis Examination Committee

..... Chairman

(Associate Professor Dr. Apiniti Jotisankasa)

..... Advisor

(Professor Dr. Panich Voottipruex)

..... Committee

(Associate Professor Dr. Raksiri Sukkarak)

..... Committee

(Assistant Professor Dr. Krairoj Mahannopkul)

Name : Mr. Chinnakrit Ounjai
Thesis Title : Protecting embankments from erosion using Wedelia trilobata
Major Field : Civil Engineering and Education
King Mongkut's University of Technology North Bangkok
Thesis Advisor : : Professor Dr. Panich Voottipruex
Academic Year : 2025

ABSTRACT

This thesis investigates the engineering potential of Wedelia trilobata (*W. trilobata*), a fast-growing creeping herb, for application in soil reinforcement and erosion control. The study is divided into two main parts. Part 1 focuses on the root system architecture and biomechanical behavior of *W. trilobata* grown for 90 days in two soil media (lateritic soil and rice husk ash). A rhizobox system was used to examine root distribution, side-root area ratio (RAR_s), root diameter, and orientation. Tensile tests were performed monthly to determine the tensile strength and Young's modulus of the roots, which were used to estimate the root cohesion (C_r) contributing to slope stability. The roots were uniformly distributed along the 1 m depth, with C_r values ranging between 3.56 and 3.92 kPa, demonstrating a strong reinforcing effect comparable to that of other species used in bioengineering works. Part 2 examines the erosion-reducing performance of *W. trilobata* under controlled rainfall conditions. A laboratory flume (2.50 m × 0.65 m × 0.25 m) was filled with lateritic soil compacted to dry densities of 1.30, 1.50, and 1.70 g/cm³. Vegetation treatments included bare soil and surfaces covered by plants grown for 1, 2, and 3 months, as well as decayed vegetation. Simulated rainfall of 87.4 mm/h was applied for 60 minutes using the Keifer and Chu distribution. Runoff volume and sediment yield were measured, and surface deformation was analyzed using photogrammetry and smartphone-based LiDAR DEMs. Results showed that *W. trilobata* substantially reduced runoff and sediment loss compared to bare soil, especially after 2–3 months of growth, confirming its effectiveness as an eco-friendly ground cover for erosion mitigation in tropical regions.

.

(Total 150 Pages)

Keywords : Wedelia trilobata, root system architecture, rhizobox, root cohesion, erosion control, rainfall simulation, smartphone LiDAR

_____ Advisor

ACKNOWLEDGEMENTS

This thesis has been successfully completed with the generous support, guidance, and valuable advice from many individuals to whom I am deeply grateful. I would like to express my sincere gratitude to Professor Dr. Panich Voottipruex, my thesis advisor, and Associate Professor Dr. Raksiri Sukkarak, for their kind guidance, insightful suggestions, and continuous assistance throughout this research. Their encouragement, wisdom, selflessness, and moral guidance have been truly invaluable in both my academic and personal development. I am also deeply thankful to Professor Dr. Suched Likitlersuang, Department of Civil Engineering, Faculty of Engineering, Chulalongkorn University, for kindly providing access to the laboratory facilities used in this research. My heartfelt thanks are extended to Associate Professor Dr. Sompote Youwai, Department of Civil Engineering, Faculty of Engineering, King Mongkut's University of Technology Thonburi, for his valuable advice on the application of artificial intelligence techniques for data analysis. In addition, I would like to express my sincere appreciation to Professor Dr. Pitthaya Jamsawang Department of Civil Engineering, Faculty of Engineering, King Mongkut's University of Technology North Bangkok for kindly providing the experimental site for the erosion behavior tests and for his constructive comments and suggestions, which greatly contributed to the successful completion of this research.

Finally, I wish to convey my deepest appreciation to all individuals mentioned above, as well as everyone who has contributed, in any way, to this study. Your help and support—whether great or small—have been instrumental in the successful completion of this research. I am truly grateful to you all.

Chinnakrit Ounjai

TABLE OF CONTENTS

Page

ABSTRACT ..... **iv**

ACKNOWLEDGEMENTS ..... **v**

TABLE OF CONTENTS ..... **vi**

LIST OF TABLES ..... **viii**

LIST OF FIGURES ..... **ix**

LIST OF ABBREVIATIONS ..... **xii**

CHAPTER 1 ..... **1**

INTRODUCTION **1**

1.1 Statement of problem 1

1.2 Objectives 3

1.3 Scopes and limitations 3

CHAPTER 2 ..... **4**

LITERATURE REVIEW **4**

2.1 Mechanism of soil erosion 4

2.2 Mechanisms of slope erosion 8

2.3 Mechanism of raindrop splash on soil surfaces 10

2.4 Mechanism of surface runoff 11

2.5 Rainfall 13

2.6 Road Embankment 23

2.7 Erosion Control 27

2.8 Wedelia trilobata 30

2.9 Photogrammetry 32

2.10 LiDAR and Close range photogrammetry 35

CHAPTER 3 ..... **39**

METHODOLOGY **39**

3.1 Testing Standard 39

3.2 Test Material 41

3.3 Experimental Procedure for Cultivating Wedelia trilobata 49

3.4 Preparation of the Erosion Testing Flume 50
3.5 Preparation of Artificial rainfall 51
3.7 Analyzing Erosion Behavior Using Digital Elevation Model Technique 57
3.8 Measurement of root architecture 59
3.9 Measurement root tensile strength and root cohesion (Cr) estimation 63
3.10 Root reinforcement estimation 67
3.11 The slope stability analysis 69
3.12 Data Analysis Using Heatmap 70
CHAPTER 4 72
ROOT BIOMECHANICAL RESULT 72
4.1 Result of root architecture 72
4.2 Root engineering properties 80
4.3 Application for slope stability analysis 84
CHAPTER 5 89
EROSION BEHAVIOR RESULT 89
5.1 Erosion result 89
5.2 Runoff rate and Sediment rate compared with Bare soil and Groundcover 107
5.3 Analyzing Erosion Behavior Using DEM 109
CHAPTER 6 112
CONCLUSION 112
6.1 Root biomechanical result 112
6.2 Erosion behavior result 114
REFERENCES 116
APPENDIX A 134
APPENDIX B 138
APPENDIX C 148
VITA 155

LIST OF TABLES

Page

TABLE 2-1 Frequency Analysis of Maximum Rainfall for Each Period at Rayong Met.Observation 1986-1998 (Source: DOH Thailand, 2012) 14
TABLE 2- 2 Frequency Analysis of Maximum Rainfall for Each Period at Rayong Met.Observation 1986-1998 (Source: DOH Thailand, 2012) 14

TABLE 3-1 Criteria for testing engineering properties 39
TABLE 3-2 Specified particle size distribution Standard No. of DH-S 205/2532 44
TABLE 3-3 Criteria for testing soil standard compaction. 45
TABLE 3-4 Soil Nutrient Results of Laterite soil and Rice husk ash 48
TABLE 3-5 Summary of the physical and chemical properties of the two selected growth media 60

TABLE 4-1 Summary of root architecture parameters of WT. in rice husk ash 60 days 74
TABLE 4-2 Summary of root architecture parameters of WT. in rice husk ash 90 days 74
TABLE 4-3 Summary of root architecture parameters of WT. in Laterite soil 60 days 75
TABLE 4-4 Summary of root architecture parameters of WT. in Laterite soil 90 days 75
TABLE 4- 5 Summary of root-induced cohesion values produced by W. trilobata 84

LIST OF FIGURES

Page

FIGURE 2-1 Graphical explanation of erosion and sediment formation 4
FIGURE 2-2 Raindrop impact on soil surface (Source : Fernández-Raga et al. 2017) 5
FIGURE 2-3 Landscape morphology at the Potshini catchment of the KwaZulu-Natal province (South Africa) and water erosion features (Source P. Dlamini et al. 2011) 6
FIGURE 2-4 Rill erosion at a construction site. (Source : M. Mamo) 6
FIGURE 2-5 Gully erosion (Source: Martin J. Potgieter & Benjamin Raselabe 2011) 7
FIGURE 2-6 Stream Channel erosion (Source: Snohomish 2018) 8
FIGURE 2-7 a. Erosive precipitation hits a slope surface b. Pore blockage c. Surface runoff with material transport (Source: www.naue.com/erosion-stable-road-embankments-design-and-selection-of-system-solutions/) 9
FIGURE 2- 8 Schematic diagram of the splash mechanism at (A) high shear-strength soil (B) Low shear-strength soil (Source:Al-Durrah and Bradford, 1982) 10
FIGURE 2-9 Diagram depicting the effects of force on soil particles in a water bed (Source:Voottipruex et al. 2013) 12
FIGURE 2-10 Diagram of raindrop shape depends on size (Source: USGS, 2018) 13
FIGURE 2-11 Rainfall Intensity Duration Frequency Curve at Rayong Met.Observation 1986-1998 (Source: DOH Thailand, 2012) 15
FIGURE 2-12 Mean monthly rainy day in eastern part of Thailand 16
FIGURE 2-13 Average yearly rainfall in eastern Thailand 17
FIGURE 2- 14 Ordinary or Standard Rain Gauge 18
FIGURE 2-15 Recording Rain Gauge 19
FIGURE 2-16 Cumulative percentage of rainfall and the distribution of rainfall over time at a 50% probability for a 1-hour and 3-hour 20
FIGURE 2-17 Derivation of the Chicago Design Storm (Source: Keifer and Chu 1957) 23
FIGURE 2-18 Construction of the embankment for exit from highway among the forest in Russia (Source:Yury Gubin 2013) 24
FIGURE 2-19 Road Embankment Material (Source: to-mats.lnwshop.com) 26
FIGURE 2-20 Road typical cross-section (DOH Thailand standard drawing 2015) 27
FIGURE 2-21 Model of the Interaction Behavior Between Soil and Vetiver Roots (Source: Montri & Kritsada, 2003) 29
FIGURE 2- 22 Model of root reinforcement in shear zone (Wu, 1976; Gray and Ohashi, 1983; Schmidt, Roering, et al., 2001) 30
FIGURE 2-23 Wedelia trilobata (Sphagneticola trilobata) 32
FIGURE 2-24 Example of data processing and integration using photogrammetry and 3D scanning systems.(Source: Beraldin, 2004) 34
FIGURE 2-25 The trail surface changed from 2016 to 2022 in the section repaired in August 2016 and August 2017 Source:(Kobayashi and Watanabe 2023) 35
FIGURE 2-26 Light detection and ranging (LiDAR) survey data acquisition (Muhadi et al. 2020) 36

FIGURE 2-27 Schematic of Structure from Motion (SfM) method. Photographs are taken at a variety of orientations; the matched features in multiple photographs are used to estimate relative camera position, which is then extrapolated to create a point cloud, or 3D model, of the scene. (Figure modified from Chris Sweeney, UCSB). 37

FIGURE 3-1 Flowchart 40
FIGURE 3-2 Laterite soil and Rice husk ash..... 41
FIGURE 3-3 Casagrande Apparatus..... 41
FIGURE 3-4 Atterberg Limit Result 42
FIGURE 3-5 Plastic limit sample 43
FIGURE 3-6 Laterite soil grain size 43
FIGURE 3-7 Show the particle size distribution 44
FIGURE 3-8 Show the Maximum dry density and Optimum moisture content..... 46
FIGURE 3-9 Show Cohesion and internal friction angle 47
FIGURE 3-10 SEM & EDX (QUANTA 450)..... 48
FIGURE 3-11 SEM & EDX Result of Laterite soil and Rice husk ash..... 49
FIGURE 3-12 Experimental Procedure for Cultivating Wedelia trilobata 50
FIGURE 3-13 Preparation of testing flume 51
FIGURE 3-14 Artificial rainfall systems schematic 52
FIGURE 3-15 IDF curve for rainfall stations in the eastern region..... 53
FIGURE 3-16 Rainfall intensity over 10-minute intervals within 1 hour 54
FIGURE 3- 17 Prepare Erosion Testing 56
FIGURE 3-18 Determining Photogrammetric Surveying Positions and Processing..... 58
FIGURE 3-19 a.Rhizobox system and b.digital camera system..... 60
FIGURE 3-20 Processing and analysis of Wedelia trilobata rhizobox images 61
FIGURE 3-21 Image processing for defining Root Area Ratio (RARs) 62
FIGURE 3-22 Experimental setup for root tensile strength test 65
FIGURE 3- 23 slope stability analysis incorporating root cohesion (C_r) zones in reinforced and unreinforced soil layers 70

FIGURE 4-1 Root diameter distribution of W.trilobata 73
FIGURE 4-2 Root architecture characteristics of W.trilobata grown in rice husk ash..... 76
FIGURE 4-3 Root architecture characteristics of W.trilobata grown in grown in laterite soil 77
FIGURE 4-4 Boxplots illustrating the distribution of root system parameters of W. trilobata grown in rice husk ash (RHA) and lateritic (LT) soils at 60 and 90 days of growth: (a) root area ratio (RAR_s), (b) root diameter, and (c) root orientation. 79
FIGURE 4-5 Correlation between tensile strength (Tr) and root diameter (d) of Wedelia trilobata 80
FIGURE 4-6 Correlation between Young's modulus and root diameter (d) of Wedelia trilobata 81
FIGURE 4-7 Relation Tensile strength and Young's modulus of Wedelia trilobata 82
FIGURE 4- 8 Slope analysis results soil without roots and soil with roots..... 85
FIGURE 4-9 Increase in percentage of safety factor..... 86
FIGURE 4-10 Correlation (heat map diagram) between various effective parameters on the FS..... 88

FIGURE 5-1 Summary of cumulative erosion result in each rainfall event 90
FIGURE 5-2 Total Sediment yield with Ground coverage in each rainfall event 97
FIGURE 5-3 Total Surface runoff with Ground coverage in each rainfall event 101
FIGURE 5-4 Total Infiltration with Ground coverage in each rainfall event 104
FIGURE 5-5 Runoff rate and Sediment rate compared with Bare soil and Groundcover 108
FIGURE 5-6 DEM characteristics of the erosion process bare soil (Before-after) 110
FIGURE 5-7 DEM characteristics of the erosion process groundcover (2 and 3 months) .. 111



LIST OF ABBREVIATIONS

MDD	Maximun dry density
OMC	Optimum moisture content
ρ	Soil density
Rr	Runoff rate
Sr	Sediment rate
Sc	Sediment concentration
G	Growth rate
C	Soil cohesion
φ	Soil friction angle
Cr	Soil cohesion with the root
Tr	Root tensile strength
RARs	Root area ratio (Side)
i	Root orientation
RSA	Root system architecture
FS	Factor of Safety

CHAPTER 1

INTRODUCTION

1.1 Statement of problem

Wedelia trilobata (*W. trilobata*), Creeping Daisy or Singapore Daisy is native to tropical America, a species of herbaceous plant characterized by its remarkable and rapid growth patterns, exhibiting a propensity for widespread distribution across tropical and subtropical geographical regions (Dai et al., 2016, 2024; Mei et al., 2022; Qin et al., 2015). It is renowned for its vigorous vegetative propagation and extensive root system, which allow it to quickly colonize disturbed soils and provide ground cover in a variety of ecosystems. *W. trilobata* notable adaptation to elevated thermal conditions is manifest, as it maintains superior photosynthetic efficiency and optimal water utilization under elevated temperature scenarios (Yu et al., 2024). *W. trilobata*'s ability to rapidly spread and bind soil makes it particularly valuable for soil erosion control (Dai et al., 2024), particularly in areas where rapid revegetation is necessary. However, studies specifically focusing on the root system architecture of *W. trilobata* remain very limited to date, despite its widespread use as a ground cover species and its potential for engineering applications.

Based on its advantageous engineering properties particularly its robust root architecture, rapid ground coverage, and erosion resistance *W. trilobata* was selected for vegetative reinforcement of the side slope of the earthen embankment. Field observations indicate that the use of this creeping plant significantly enhanced both slope stability and resistance to surface erosion. The dense vegetative mat formed by *W. trilobata* reduces the impact of raindrop splash and retards surface runoff, contributing to the long-term integrity of the slope surface. This case demonstrates the potential of nature-based solutions in geotechnical and hydraulic engineering applications, especially in tropical environments.

Numerous research efforts have examined the use of plant roots in engineering, especially grasses species and other deep-rooting species. The root system architecture (RSA) of grasses, such Vetiveria zizanoides (Chen et al., 2024; Nguyen et al., 2019;

Wang et al., 2023), Agrostis stolonifera (Lann et al., 2024), Cynodon dactylon (F. Chen et al., 2015; Leung et al., 2015; Xu et al., 2023) and Festuca arundinacea (Gong et al., 2024; Saadati et al., 2023) have been well-documented in the literature, with studies demonstrating that these species can significantly enhance slope stability by increasing the soil's resistance to shear forces. These studies suggest that the root system characteristics, such as root depth and density, play a fundamental role in improving soil cohesion and reducing the potential of slope failure. Furthermore, it is not only the different plant species that influence RSA, but also the soil type, which affects root growth and the surrounding soil structure. Several studies have shown that RSA is significantly influenced by the type of soil (i.e., rice husk ash, clay, laterite and hydroponics), affecting the strength provided by root reinforcement. Variations in soil composition, texture, structure, and nutrient availability, can either promote or limit root development, producing variable degrees of root system development (Helliwell et al., 2019; Likitlersuang et al., 2022b; Poeplau & Kätterer, 2017). Especially in engineering applications, these variations in root area and growth patterns directly affect the general efficiency of plant roots in developing soils.

According to the literature, however, *W. trilobata* has not been systematically explored, especially concerning its potential for slope stabilization and soil reinforcement. A comprehensive understanding of how *W. trilobata* roots interact with soil, alongside comparing its RSA to that of other commonly utilized species, is crucial for assessing its applicability in engineering contexts. In particular, the ability of its roots to penetrate deeper soil layers and create a dense network within the soil matrix could potentially provide enhanced reinforcement when compared to other ground cover plants.

Therefore, this study aims to investigate the engineering potential of *W. trilobata* for application in embankment reinforcement, focusing on both its biomechanical and erosion control characteristics. The research is structured in two major components. The first part involves a biomechanical engineering investigation, in which the root system architecture (RSA) of *W. trilobata* is examined through rhizobox experiments, combined with tensile and modulus testing to determine the root cohesion (C_r) parameter essential for slope stability analysis. The second part focuses

on the erosion control performance of *W. trilobata* through a series of laboratory flume experiments. In this part, erosion rates of bare soil and vegetated slopes with varying root densities and ground coverage ratios are compared. Moreover, point-cloud LiDAR technology is employed to quantitatively assess soil surface deformation and identify spatial patterns of erosion. Together, these complementary approaches provide a comprehensive evaluation of the potential of *W. trilobata* as a sustainable vegetation species for geotechnical and ecological engineering applications.

1.2 Objectives

The objectives of this research are as follows:

1. To study effectiveness of Wedelia Trilobata in preventing soil erosion.
2. To study the behavior of soil erosion using close-range photogrammetry method.
3. To study Soil Stabilization Potential of Wedelia Trilobata
4. To study Root System Characteristics of Wedelia Trilobata
5. To study Application of Wedelia Trilobata for slope stabilization
6. To study reinforcing effect of Wedelia Trilobata

1.3 Scopes and limitations

The scope and limitations of this research are as follows

1. The type of soil used in erosion testing is laterite soil
2. Testing Tray dimension is 2.50x0.65x0.30 m
3. Artificial Rainfall designed for 25-year return period
4. Root System Characteristics use Laterite soil and Rice husk ash
5. Root testing Growth period : 1 month, 2 months, 3 months, decaying
6. Erosion testing Growth period: baresoil 1 month, 2 months, 3 months, decaying

CHAPTER 2

LITERATURE REVIEW

2.1 Mechanism of soil erosion

Soil erosion is a significant environment natural process and is among the most critical environmental problems it is crucial to conduct. Rainfall and runoff detach and transport soil, causing water erosion. (J E Gilley 2005)Water erosion can be classified based on various characteristics as shown below

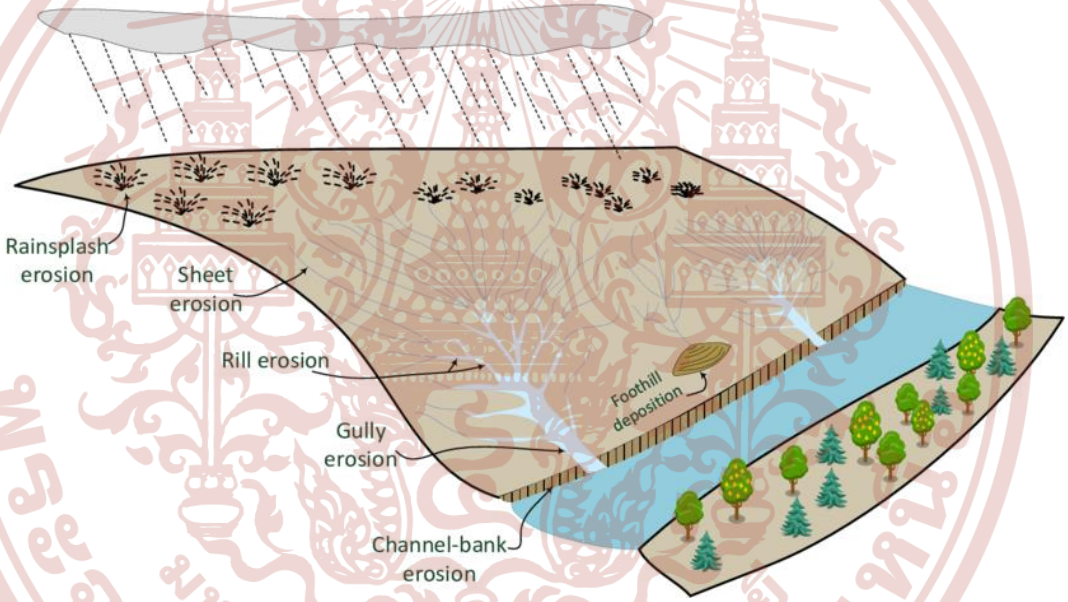


FIGURE 2-1 Graphical explanation of erosion and sediment formation

(Source : Klajdi Sotiri 2020)

2.1.1 Rain splash erosion

The term splash erosion comprises processes related to the impact of water drop on a substrate surface and transport of soil particles with or without the liquid from the hillslope. The impacting raindrop disrupts aggregates and ejects the downsized parts or single substrate particles outwards from the point of drop. (Marzen and Iserloh 2021)

Rainfall erosivity is the capability of rainfall to cause soil loss. Erosivity is based on rainfall intensities The science indicates the direct role of kinetic energy of rainfall as the driver of hillslope erosion (Nearing et al. 2017)

With increasing splash frequencies and raindrop diameters Aggregates splashed by 4.05 mm diameter raindrops After the broken aggregates blocked the pores, a dense and low permeable crust was formed on the topsoil, and it decreased the cumulative amount of infiltration and the infiltration rate (Ma et al. 2022)

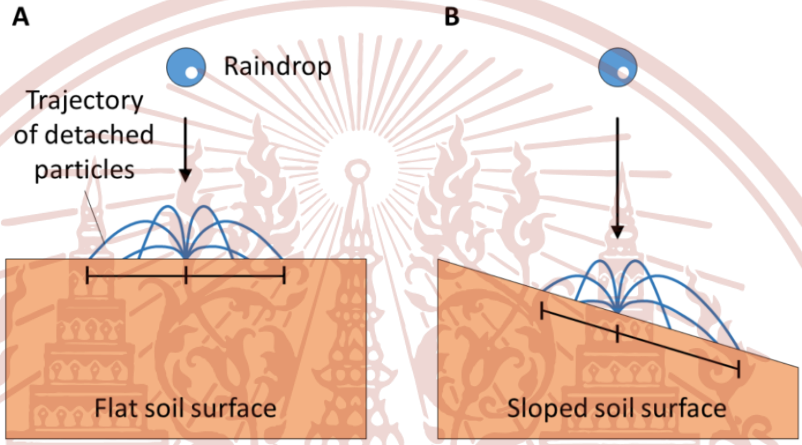


FIGURE 2-2 Raindrop impact on soil surface (Source : Fernández-Raga et al. 2017)

2.1.2 Sheet erosion

Sheet erosion happens when water flows over the surface of the land removing soil and sediment. Understanding runoff discharge and sediment concentration in hillslopes with varying geometries can provide better insights into hydrological processes in watershed systems.(Kiani-Harchegani, Talebi, and Kiani 2021)

Sheet erosion occurs when water flowing off an uncovered or bare field carries away soil particles, resulting in the uniform removal of soil in thin layers and loss of topsoil (Kenny, Westendorf, and Williams 2018)

The Correlation between slope angle and soil loss is best represented by a polynomial function. Other relevant factors, such as soil type, moisture levels, and surface soil characteristics, were kept constant. Rain splash and sheet were the main modes of transport studied, along with the thickness of surface water layers and the size and impact point of raindrops. (Bryan 1979)

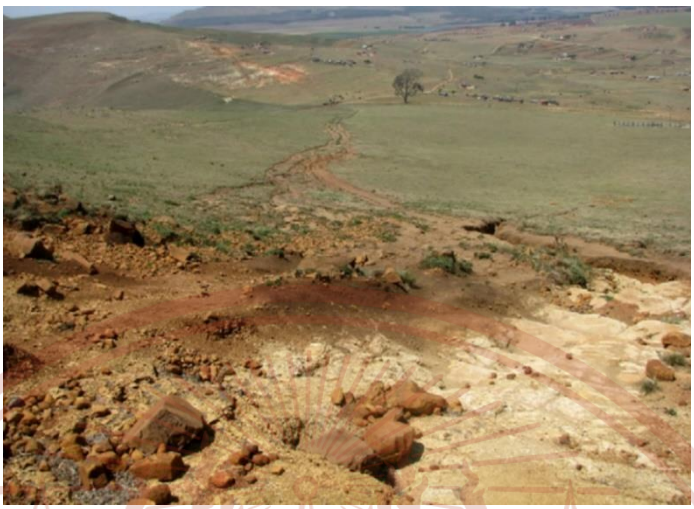


FIGURE 2-3 Landscape morphology at the Potshini catchment of the KwaZulu-Natal province (South Africa) and water erosion features (Source P. Dlamini et al. 2011)

2.1.3 Rill erosion

As overland flow moves downslope. Small channels or rills may form as the runoff velocity of overland flow Rills caused by runoff over erodible soil are usually irregular in profile and cross section and may not approximate any regular geometrical shape increasing average soil loss and the area is dominated by rill and inter-rill water erosion (Ketema and Dwarakish 2021)

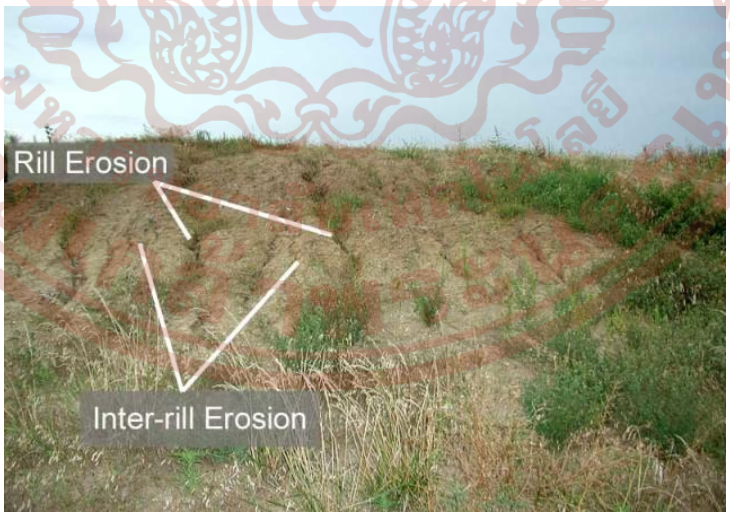


FIGURE 2-4 Rill erosion at a construction site. (Source : M. Mamo)

2.1.3.1 Rill erosion

As water flows downhill, it becomes more concentrated due to the shape of the ground. This can cause small channels or rills to form when water moves faster these tills often appear between rows of crops or along areas where the ground has been tilled. The amount of erosion caused by the flowing water and the properties of the soil can affect how these rills form. Usually, when the ground is tilled, the rills are removed.

2.1.3.2 Inter-rill Erosion

When raindrops hit the ground, they can cause tiny particles of soil to come loose in areas between ridges. These loose particles may then be carried away by shallow flowing water to deeper channels. The erosion of these inter-rill areas is affected by different factors such as the characteristics of the soil the intensity of the rainfall, and the slope of the land. Inter-rill erosion is often noticeable on the brighter upper areas of slopes that are slightly rounded, where plowing mixes the surface soil with the soil underneath.

2.1.4 Gully erosion

occurs where concentrated surface water scours out the regolith and underlying rock with the debris being either deposited downslope or transported into river systems creating major downstream problems. The gully form and severity are very dependent on the rock type. The very severe to extreme gully erosion is restricted to argillites mudstone, and fine siltstones with each rock type having its characteristic gully shape (I McIvor et al. 2017)



FIGURE 2-5 Gully erosion (Source: Martin J. Potgieter & Benjamin Raselabe 2011)

2.1.5 Stream channel erosion

When soil is removed from the banks or beds of streams, it causes erosion in steam channels. Although the affected areas are relatively small, The impact on highly productive soils can be severe. The erosion happens when water flows over the side of the stream bank or scours below the water surface, especially during severe floods. Stream Channel erosion is usually more significant on the outside of bends and meandering also causes erosion on stream banks. Additionally, reducing sediment delivery from upland areas through control practices or capturing sediment in water storage facilities may increase stream channel erosion (J E Gilley 2005)



FIGURE 2-6 Stream Channel erosion (Source: Snohomish 2018)

2.2 Mechanisms of slope erosion

Erosion often occurs on road embankments when there is a strong and constant impact of precipitation due to local weather phenomena. Likewise, dry periods cause the soil to hold together no longer in agglomerates due to a lack of cohesion of the soil particles but to fall apart. In the next step, high wind or water forces transport detached soil particles away. This may lead to visual obstructions due to dust accumulation or to silting and clogging by mud. If the transport forces decrease, the possibly contaminated soil material is deposited again in undesirable

places. This triad of erosion, transport, and deposition can lead to considerable problems

On slopes, surface or rill erosion usually occurs after a precipitation event has redistributed the surface. Figure 2-7a shows the raindrop transferring its kinetic energy to the slope surface as soon as it reaches the ground surface. In the process, the droplet disintegrates the soil particles. In Figure 2-7b. fine particles begin to clog the pores of the soil surface and reduce infiltration. Initial sloughing begins. Surface runoff has formed in Figure2-7c and downslope particle removal begins. Erosion, the start of the movement and subsequent transport, leads to familiar erosion phenomena, such as erosion of rills and gullies or surface erosion.

Slopes along heavily used traffic routes should be particularly protected against erosion. This is because spontaneous failure poses a risk to road users with costly consequences, e.g. expensive damage repair. Deconstruction costs can be high if deposited material impairs technical structures. It, therefore, makes sense to implement measures to reduce the erosion risk at an early stage. Thus, it is necessary to correctly understand the processes involved and develop targeted, project-specific solutions.(Anabell Klein 2022)

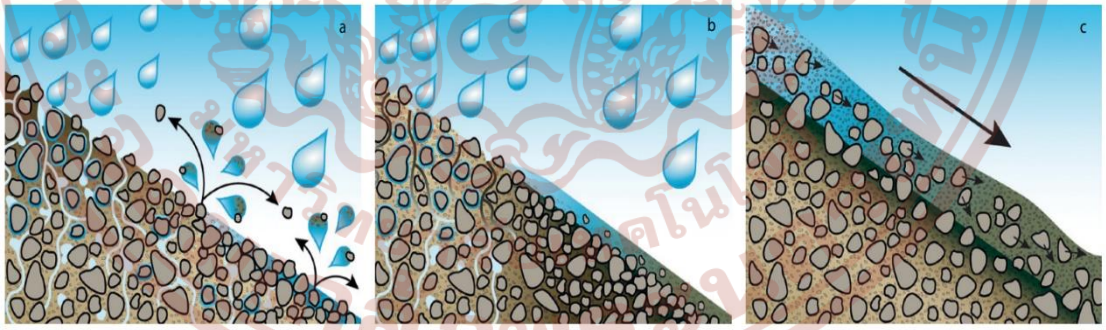


FIGURE 2-7 a. Erosive precipitation hits a slope surface b. Pore blockage c. Surface runoff with material transport (Source: www.naue.com/erosion-stable-road-embankments-design-and-selection-of-system-solutions/)

2.3 Mechanism of raindrop splash on soil surfaces

Rainfall impact is a crucial factor in the milling process. In a study by (Al-Durrah and Bradford 1982), the effects of rainwater shock were tested by dropping water droplets from a height of 890 centimeters onto different soil surfaces. The study used six types of soil, and high-speed photography was used to record the moment raindrops hit the ground surface. From the study, it was found that the splash angles ranged from 11 degrees for soils with a shear strength of 20 kPa to 40 degrees for soils with a shear strength of 1 kPa.

(Young and Wiersma 1973) also studied the effect of rainfall on the separation of soil grains and the induced soil mass. They showed that there was an 89 percent reduction in the energy of raindrop impact with no reduction in rain intensity. However, a reduction in rain intensity resulted in a 90 percent reduction in erosion (using water droplets and reducing the speed of impact for the impact effect of rainwater).

(Al-Durrah and Bradford 1982)described the process of the falling impact of rainwater on the soil surface, as shown in Figure 2-8

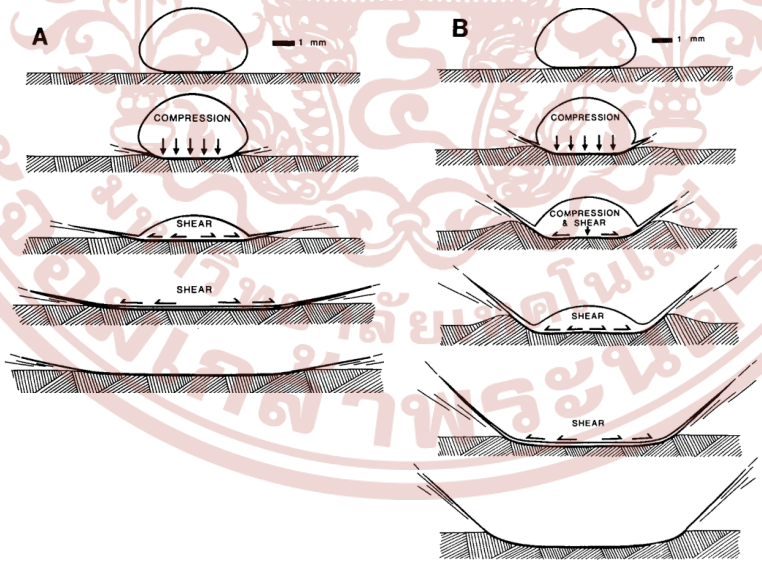


FIGURE 2- 8 Schematic diagram of the splash mechanism at (A) high shear-strength soil (B) Low shear-strength soil (Source:Al-Durrah and Bradford, 1982)

The angle at which raindrops hit the soil determines how much of the land gets splashed and how severe the impact is. The size of the raindrops is also important in this process. The soil's internal cohesion and clamping force affect how much the soil is deformed. If the soil has high internal cohesion strength, it will experience less loss from the impact of rainwater. As rainwater moves to the bottom, the impact force changes to shear force along the boundary between the soil mass and rainwater. The soil particles then break apart and spread out to the side due to radial velocity, which depends on the impact velocity. The amount of soil that separates depends on the deformation of the soil mass. (Al-Durrah and Bradford 1982)showed that the splash angle is related to the yield strength. Soil shear is shown in Equation 2-1

$$\theta_s = 40.5\tau^{-0.425}$$

When θ_s is The equation splash angle and τ is Shear Strength in question is independent of soil type It has been observed that there is a consistent increase in the amount of water retained in soil across different soil types. Equation 2-2 shows the relationship between the soil leakage inspection service provider and soil properties. This equation explains how the weight of water in a barn can be related to the kinetic energy system of the carrier and the chef's system. It also applies to soil that is underwater with no drainage.

$$S = a + b(K_E / \tau)$$

When S is the Volume of loose soil (mg/drop) K_E is Kinetic Energy a and b is cone fall of Swedish method

2.4 Mechanism of surface runoff

Research studies have identified two basic factors that contribute to erosion: 1) loosening of soil grains, and 2) movement of soil grains caused by resistance forces. When water flows through the soil, it generates a drag force, which is countered by the internal friction angle or the force of cohesion between soil grains. The magnitude of the pulling force depends on the speed and volume of the flow, as well as the shape and roughness of the soil grains. The resistance force is determined by the shear strength

properties of soil masses. There are four main factors that control erosion due to rainwater. There are four reasons listed below.(Voottipruex et al. 2013)

- Weather refers to atmospheric conditions including precipitation and storm frequency. Erosion is caused by rainfall.
- Soil type refers to the degree of susceptibility of a particular soil to erosion.
- Degrees of Slope
- Ground Coverage

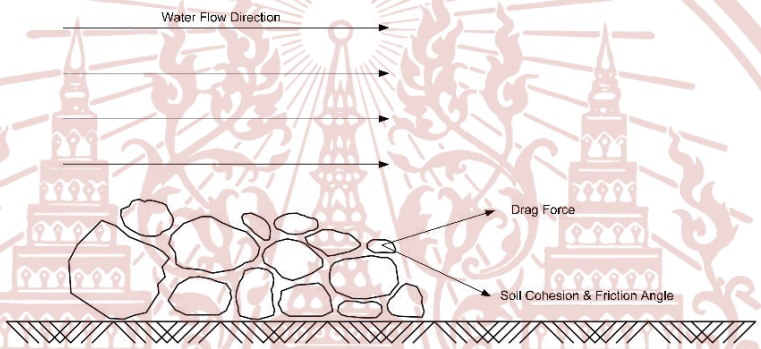


FIGURE 2-9 Diagram depicting the effects of force on soil particles in a water bed (Source:Voottipruex et al. 2013)

(Wischmeier W.H. and Smith 1978)rainstorms are responsible for erosion. The study measured erosion potential using the storm energy value (EI), which is calculated by multiplying the rain energy (E, measured in hundred foot-tons per acre) and the peak intensity over a 30 minute period (I30, measured in inches per hour). The E value can indicate rainfall and surface runoff. In some cases rainfall intensity is not the only factor that affects erosion. Even a low level of rainfall that lasts for a long period of time can have the same impact as heavy rainfall that occurs in a short period of time. When raindrops hit the ground, they not only cause erosion but also make the soil denser and less permeable. This reduces seepage pressure in the soil, which is a crucial factor that contributes to erosion. erodibility some types of soil, such as sandy sediment, are more prone to erosion than others, such as well-mixed coarse gravel. The presence of organic matter or clay in the soil can reduce its susceptibility to erosion. Nevertheless, the extent

of erosion depends on the land surface characteristics, including the moisture content and Void Ratio. Based on previous research, the order of erosion ability can be summarized as follows:

ML > SM > SC > MH > OL > CL > CH > GM > SW > GP > GW

The erosion process of bare soil is influenced by various factors such as soil type, rainfall intensity, and slope. Rainfall intensity and slope have inverse patterns over time, which means that as rain intensity and slope increase, the time for surface runoff occurrence decreases. In turn, this leads to a decrease in the runoff flow rate, sediment transport rate, and intensity sediment concentration in surface runoff flow. However, the quantity of soil erosion increases with time due to the greater sediment concentration. Additionally, the permeability of water in the soil mass affects the flow of surface runoff. Surface flow is the main form of soil loss, and most of the rainfall will be lost through soil infiltration. When the soil has a higher value of water permeability, the infiltration rate increases, which reduces the quantity of soil erosion(Deng et al. 2020).

2.5 Rainfall

Rainfall is a crucial factor that is used in the calculation and design of drainage systems. Rain is a type of precipitation that falls from the atmosphere in various forms, such as snow, hail, Sleet, and Drizzle. When the air is cool and humid, the water droplets in the clouds combine to form raindrops that are typically 2-5 millimeters in size and fall to the ground. The rainy season in Thailand typically lasts for about 5 months, with rain usually ending around mid-October. This is caused by the southwest monsoon, which brings moisture from the sea and covers Thailand. However, there can be variations each year due to the weather conditions. In some years, the rain may fall 1-2 months later or earlier. (DOH Thailand manual drain, 2012)

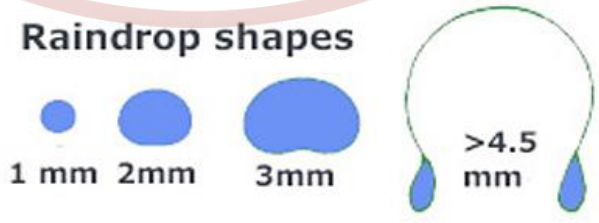


FIGURE 2-10 Diagram of raindrop shape depends on size (Source: USGS, 2018)

TABLE 2-1a Frequency Analysis of Maximum Rainfall for Each Period at Rayong Met.Observation 1986-1998 (Source: DOH Thailand, 2012)

Time (hr)	Rainfall amount (mm)								
	2 year	5 year	10 year	25 year	50 year	100 year	200 year	500 year	1000 year
0.25	23.0	28.9	32.7	37.6	41.3	44.9	48.5	53.2	56.8
0.50	37.3	44.2	48.7	54.5	58.8	63.0	67.3	72.9	77.1
0.75	46.3	57.8	65.4	75.0	82.1	89.2	96.3	105.5	112.6
1	52.7	66.9	76.4	88.3	97.1	105.9	114.7	126.2	134.9
2	60.7	78.8	90.9	106.1	117.3	128.5	139.7	154.4	165.5
3	62.9	81.4	93.6	109.0	120.5	131.9	143.2	158.2	169.5
6	66.5	88.4	102.8	121.1	134.7	148.1	161.5	179.2	192.6
12	72.3	93.4	107.3	125.0	138.0	151.0	163.9	181.0	193.9
24	81.0	102.5	116.7	134.7	148.1	161.4	174.6	192.0	205.2

TABLE 2- 2 Frequency Analysis of Maximum Rainfall for Each Period at Rayong Met.Observation 1986-1998 (Source: DOH Thailand, 2012)

Time (hr)	Rainfall amount (mm/hr)								
	2 year	5 year	10 year	25 year	50 year	100 year	200 year	500 year	1000 year
0.25	92.0	115.4	131.0	150.5	165.1	179.5	193.9	212.8	227.2
0.50	74.6	88.4	97.5	109.0	117.6	126.1	134.6	145.7	154.2
0.75	61.8	77.1	87.2	100.0	109.5	118.9	128.3	140.7	150.1
1	52.7	66.9	76.4	88.3	97.1	105.9	114.7	126.2	134.9
2	30.3	39.4	45.4	53.0	58.7	64.3	69.8	77.2	82.8
3	21.0	27.1	31.2	36.3	40.2	44.0	47.7	52.7	56.5
6	11.1	14.7	17.1	20.2	22.4	24.7	26.9	29.9	32.1
12	6.0	7.8	8.9	10.4	11.5	12.6	13.7	15.1	16.2
24	3.4	4.3	4.9	5.6	6.2	6.7	7.3	8.0	8.5

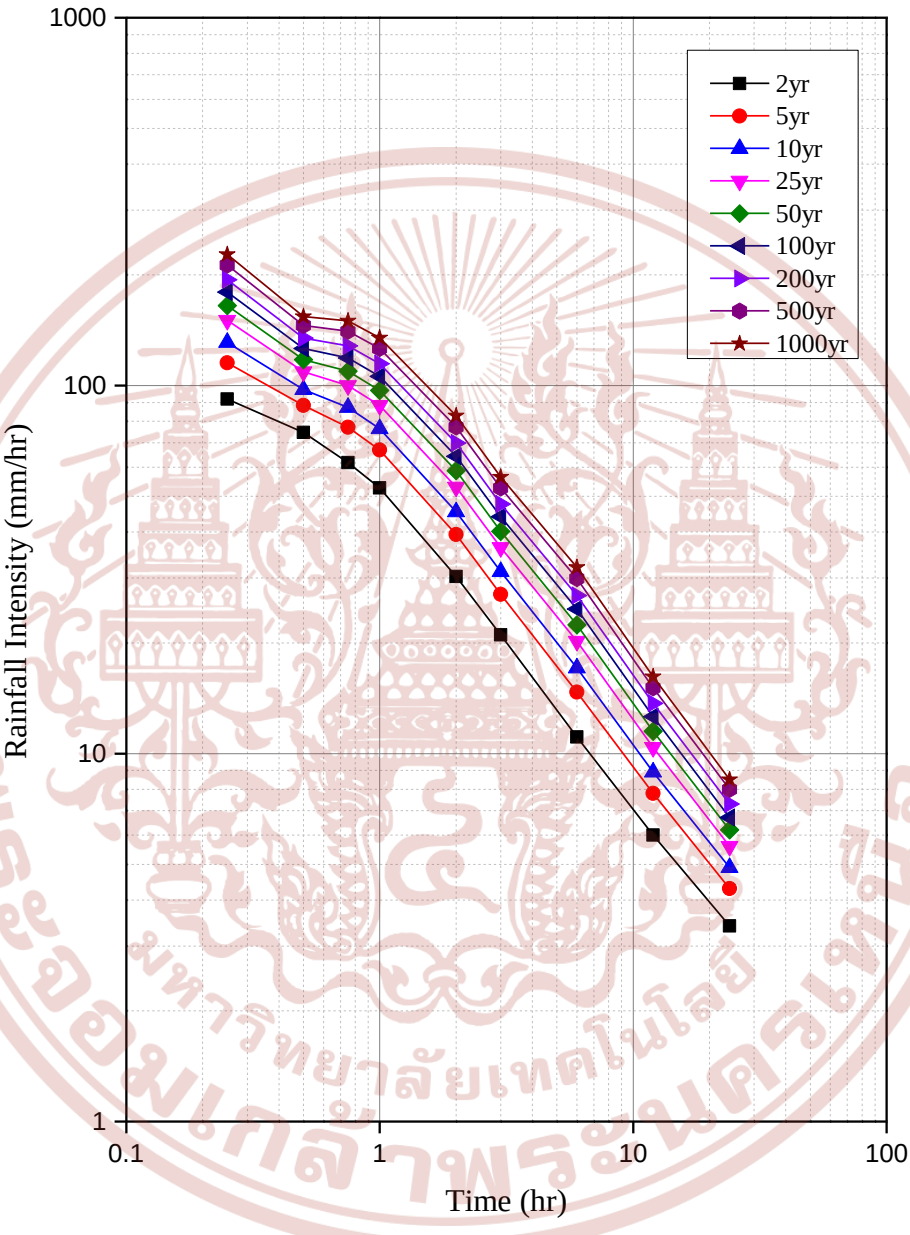


FIGURE 2-11 Rainfall Intensity Duration Frequency Curve at Rayong Met.Observation 1986-1998 (Source: DOH Thailand, 2012)

Eastern Thailand also receives abundant rain during this period. The wettest months in the region are from July to August. 2) Winter or northeast monsoon season (mid-October to mid-February). The northeast monsoon brings cold and dry air from China to upper Thailand. 3) Summer or premonsoon season, mid-February to mid-May. This is the transitional period from the northeast to the southwest monsoons. The weather becomes warmer, especially in upper Thailand. April is the hottest month for all regions of Thailand. as shown in Figure 2-12

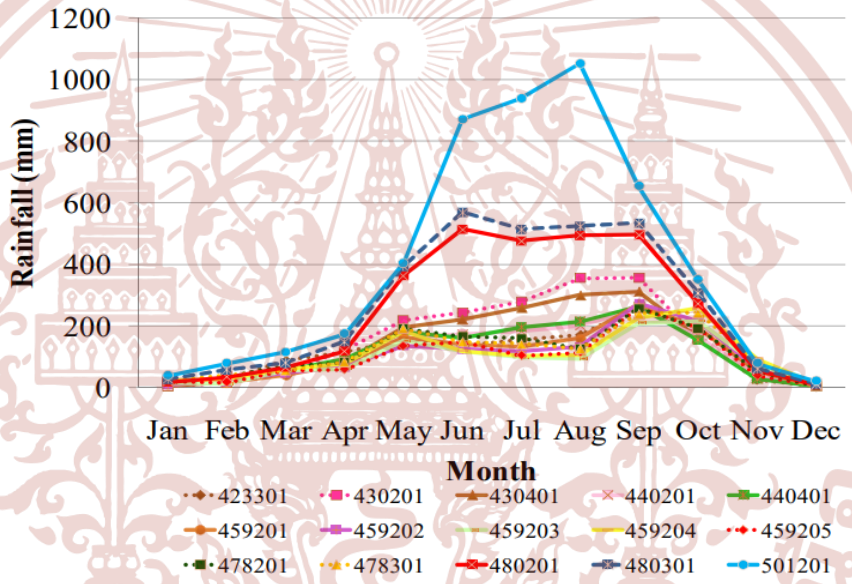


FIGURE 2-12 Mean monthly rainy day in eastern part of Thailand (Source: Nounmusig 2018)

The average annual rainfall in the eastern region of Thailand is 1921mm, based on a 40-year average. The linear trend indicates a tendency for the average annual rainfall to decrease. When the El Niño (La Niña) phenomenon is identified, the sea surface temperature anomalies (SSTAs) in the Niño34 region are above the threshold of +0.5°C (or below-0.5°C). Although the correlation between average yearly rainfall and Niño34 is weak (r =- 0.28), most of the average yearly rainfall is below normal during El Niño years, particularly in 1987, 1992, and 1997 (1,843

mm, 1,577 mm, and 1613mm, respectively). Rainfall variations in Eastern Thailand during La Niña years tend to be the opposite of those in El Niño years. The average yearly rainfall during La Niña years is mostly above normal, as seen in 1974, 1975, 1988, 1999, and 2000, with each year exceeding 2000 mm. Moreover, when considering only ENSO years (excluding normal years), it is found that the average yearly rainfall has a significant correlation with Niño34 (r =- 0.46), as shown in Figure 2-13

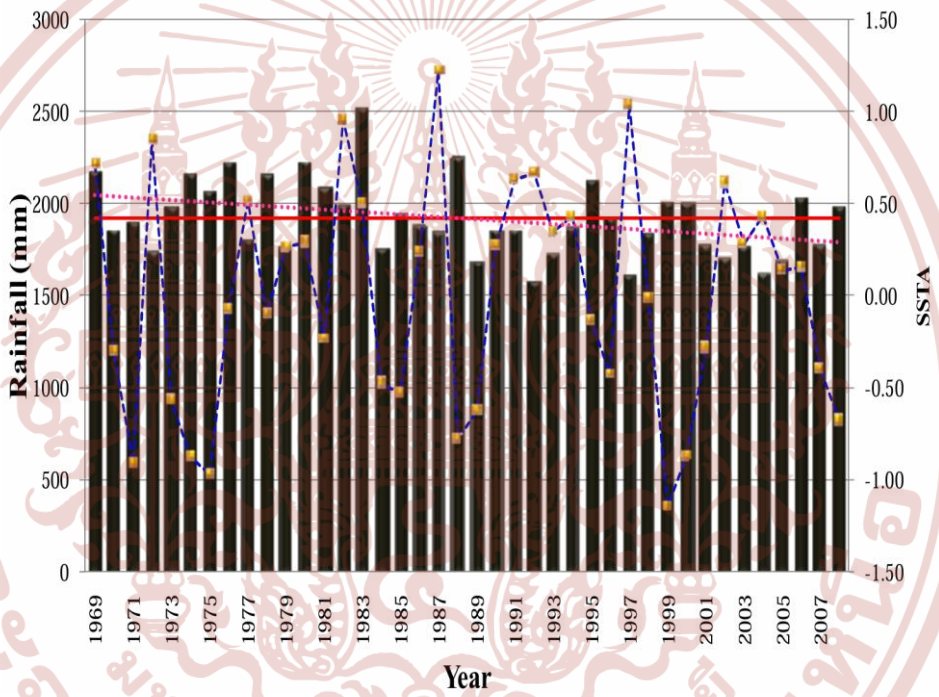


FIGURE 2-13 Average yearly rainfall in eastern Thailand (Source: Nounmusig 2018)

2.5.1 Rainfall measurement

Rainfall measurement over a specified period is expressed in terms of the depth of rainwater that falls over an area, assuming the rainfall is uniformly distributed and has an equivalent uniform depth covering the entire area. It is also assumed that there is no surface runoff, infiltration, or evaporation. The commonly used unit for measuring rainfall is millimeters (mm), though centimeters (cm) or

inches may also be used. Rainfall can be measured using rain gauges, weather radar, or meteorological satellites. Rain gauges, which are the primary instruments for measuring rainfall, can be classified into two types (Fienberg and Foufoula-Georgiou, 2009)

- Ordinary or Standard Rain Gauge:

  This type of rain gauge typically consists of a cylindrical container used to measure the total amount of rainfall during a particular event. It does not provide continuous data. While different countries may have different standards for such gauges, the principle remains the same: to measure the depth of rainfall over a given time interval.



FIGURE 2-14 Ordinary or Standard Rain Gauge

- Recording Rain Gauge:

  This type of rain gauge continuously records rainfall data over time onto a chart. The resulting graph is known as a hyetograph, which displays the distribution of rainfall intensity over time. The recording chart usually covers a 24-hour period and is replaced daily for data collection and analysis.

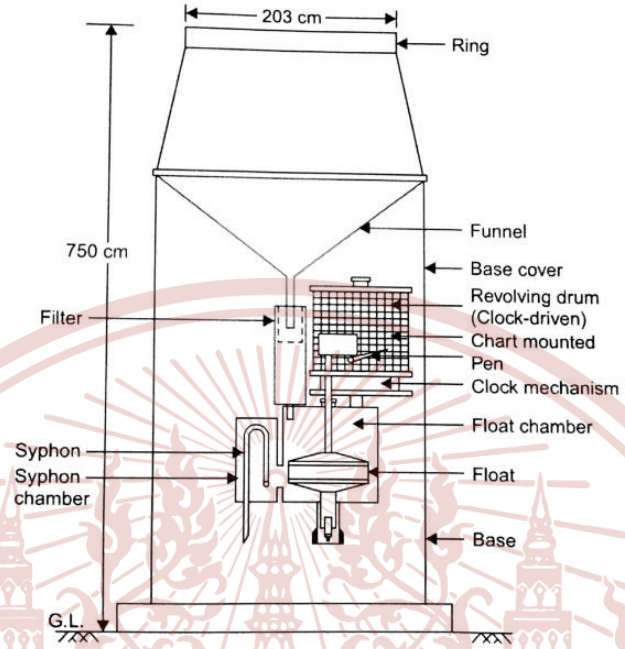
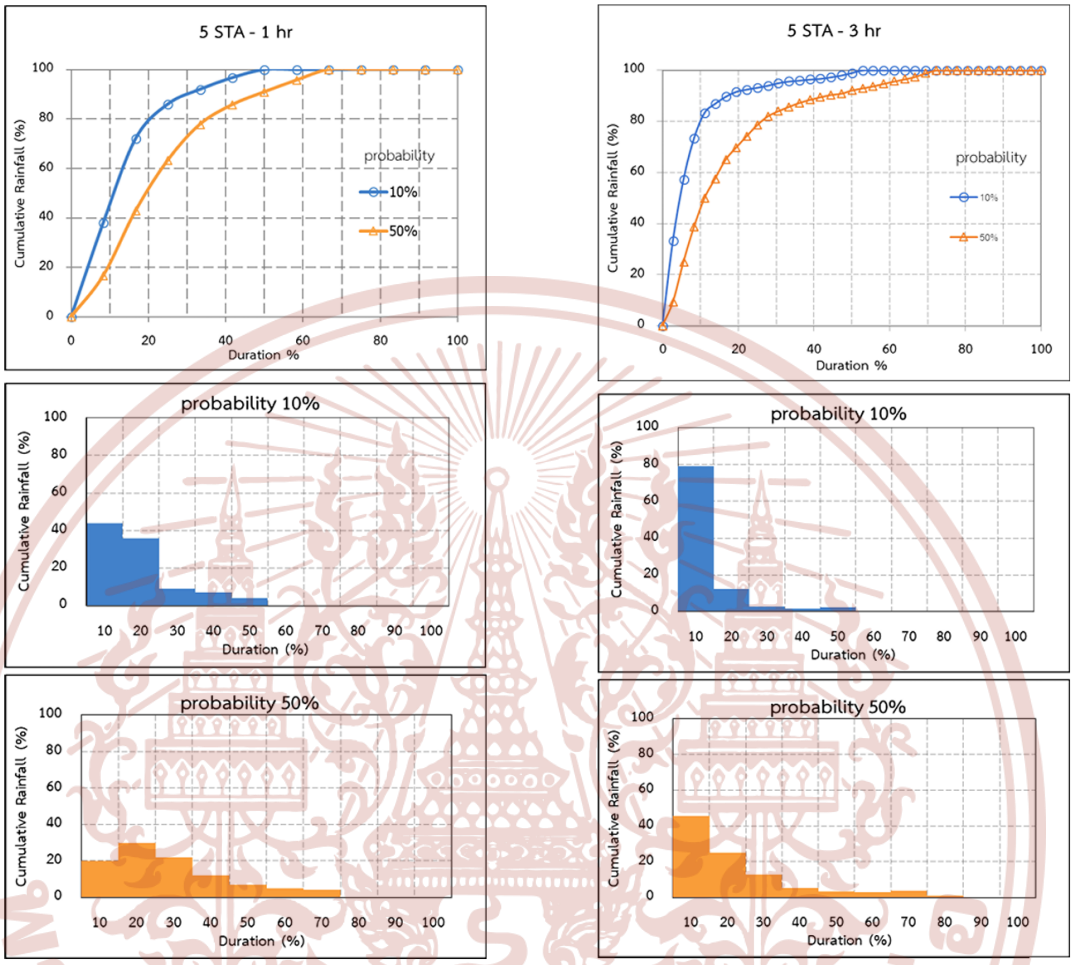


FIGURE 2-15 Recording Rain Gauge

2.5.2 Rainfall Pattern in thailand

(Ketkasem J. 2023) the temporal rainfall patterns in Bangkok to identify an appropriate model for designing urban drainage systems. Utilizing rainfall data collected at five stations across Bangkok from 2010 to 2017, the research analyzes the distribution of rainfall over different durations (1, 3, and 6 hours) at the first quartile (10th and 50th percentiles). The findings reveal that, at the 10% probability level, the total rainfall for 1- and 6-hour durations is approximately 76 and 78 times higher, respectively, than the patterns used in the United States for stormwater design. This indicates that flood peaks in Bangkok are likely to be more intense and occur more frequently than those predicted by U.S.-based models. The results underscore the necessity of adopting localized rainfall patterns for urban drainage design, particularly considering the potential impacts of climate change in the future.



(a) **(b)**

FIGURE 2-16 Cumulative percentage of rainfall and the distribution of rainfall over time at a 50% probability for a 1-hour and 3-hour

Figure 2-16a shows the cumulative percentage of rainfall and the distribution of rainfall over time at a 50% probability for a 1-hour duration across five stations in Bangkok. It illustrates that the cumulative rainfall percentages rise from 10% to 20%, and then to 30%, indicating how the accumulated rainfall varies over different time intervals. Figure 2-16b presents the cumulative percentage of rainfall and the distribution of rainfall over time at a 50% probability for a 6-hour duration across the same stations. Similar to Figure 6 but covering a longer period, this graph provides an overview of

rainfall distribution over an extended timeframe and allows for comparison between the rainfall patterns over 1 hour and 6 hours in Bangkok.

2.5.3 Artificial rainfall design

The assumption that the design storm should contain all rainfall maxima of a particular return period contradicts findings from actual storm data, including those in the original paper (Keifer and Chu 1957). It is noteworthy that Keifer and Chu recognized the weakness of their assumption and stated that the synthetic storm pattern would undoubtedly have a longer return period than the IDF curve from which it was derived. Recently, Hogg (1980) pointed out that the Chicago-type distribution is completely inappropriate for some Canadian climates and is not among the most probable distributions for the bulk of the country. Additional problems arise from determining the parameter r. Extensive analyses by Chen (1975) indicate that r is a random variable, with its mean value significantly affected by the selection of historical storms used to determine r. For example, using the Keifer and Chu data, the mean values of r for individual stations and durations vary from 0.323 to 0.583 for storms with return periods of 2-10 years. Such variations were overlooked when considering the entire set of 83 storms across 4 stations, resulting in a recommended value of r = 0.375 for further use. The Chicago design storm is developed from empirical IDF relationships. Keifer and Chu observed that if they had a continuous function representation of the instantaneous intensity and they integrated this function over a given duration, the rainfall volume occurring in that duration is obtained. The rainfall volume divided by the duration gives the average intensity. Therefore, multiplying the average intensity by the storm duration and differentiating with respect to the duration they obtained expressions for the instantaneous intensity:

$$i = \frac{a\left((1-c)t + b\right)}{\left(t + b\right)^{c+1}}$$

$$i = \frac{a\left((1-c)t^{b} + c\right)}{\left(t^{b} + c\right)^{2}}$$

These equations 2-3 and 2-4 for the shape of the storm hyetograph are for a storm pattern where the peak is at the beginning of the storm event. If the peak occurs after the beginning of the storm, the storm duration t is divided into two time periods, the time before the peak t_b and the time after the peak t_a. The ratio of the time to peak to the total storm duration is given by the equation 2-5

$$r = \frac{t_b}{t}$$

The storm duration in terms of the time before the peak and the time after the peak is given by equations 2-6

$$t = \frac{t_b}{r}$$

$$t = \frac{t_a}{1-r}$$

A typical shape for the Chicago design storm hyetograph is shown in the figure 2-17 where the intensity before the peak is given by i_b , and The storm hyetograph shape is shown in Equation 2-7

$$i_b = \frac{a\left((1-c)\frac{t_b}{r} + b\right)}{\left(\frac{t_b}{r} + b\right)^{1+c}}$$

$$i_a = \frac{a\left((1-c)\frac{t_a}{1-r} + b\right)}{\left(\frac{t_a}{1-r} + b\right)^{1+c}}$$

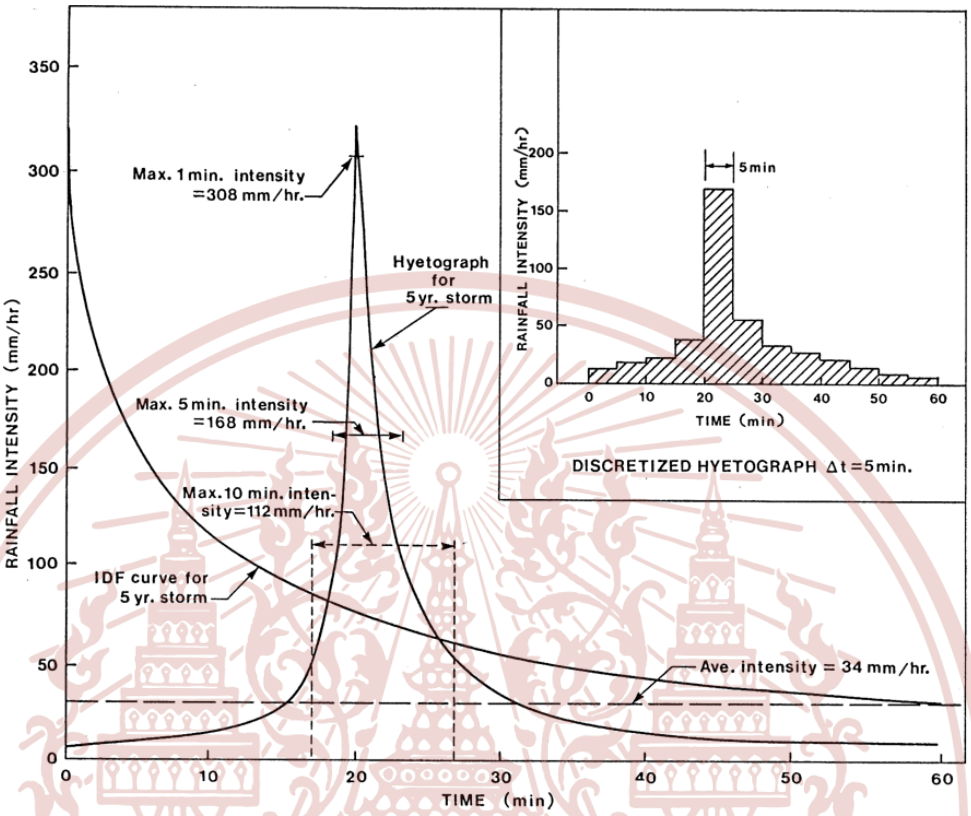


FIGURE 2-17 Derivation of the Chicago Design Storm (Source: Keifer and Chu 1957)

2.6 Road Embankment

An embankment refers to a volume of earthen material that is placed and compacted to raise the grade of a roadway (or railway) above the level of the existing surrounding ground surface. A fill refers to a volume of earthen material that is placed and compacted to fill in a hole or depression. Embankments or fills are constructed of materials that usually consist of soil, but may also include aggregate, rock, or crushed paving material. Normally, the coarser fill materials are placed at or near the bottom or base of the embankment to provide a firm foundation for the embankment and also to facilitate drainage and prevent saturation. The top portion of an embankment usually is constructed of relatively high-quality, well-compacted subgrade material that is capable of supporting the overlying pavement layers and imposed wheel loadings without deflection or undesirable movement. The fill material used throughout the remainder of

the embankment must be capable of meeting applicable specification quality requirements and be capable of being placed and compacted at or close to its maximum achievable density. The material is spread in relatively thin layers of 150 mm to 200 mm and each layer is compacted by rolling over it with heavy compaction equipment. (FHWA-RD-97-148)



FIGURE 2-18 Construction of the embankment for exit from highway among the forest in Russia (Source:Yury Gubin 2013)

2.6.1 Road Embankment Material

(M.T.C.H. 201-2545), Materials must have a Plasticity Index (PI) of zero and be free from clay lumps, topsoil, tree roots, leaves, or decomposed organic materials that may lead to future settlement. The particle size should not exceed 9.5 millimeters (3/8 inch). Additionally, fine particles passing through a 0.075- millimeter (No.200) sieve must comprise no more than 20% by weight, as determined by the particle size distribution test (Method T501.8). The California Bearing Ratio (CBR) value obtained from laboratory tests must be at least 10% at 95% of the maximum dry density, as established by the Modified Proctor method (Method T 501.3) or as per the construction

plans. Other material properties must meet the requirements set forth in the construction specifications.

For embankment materials, the CBR value from laboratory tests should not fall below 4% at 95% of the maximum dry density according to Standard Proctor tests. The maximum particle size should not exceed 50 millimeters. Additionally, swelling characteristics must remain within acceptable limits, not surpassing 4%, in accordance with the same Test Method T 501.3. 3. The material must also comply with other specifications detailed in the construction plans. Specifically for soil aggregate used in embankments, it must be durable and free from clay lumps, topsoil, roots, leaves, and any decomposed organic matter that could result in future settlement. The maximum particle size should be restricted to 50 millimeters. The standard for embankment materials, as outlined by the Ministry of Transport and Communications. stipulates that earth fill material should originate from borrow sources adjacent to existing roads or other approved locations while possessing required physical and mechanical properties. For general soil embankment material, the laboratory CBR value must be no less than 4% at 95% of the maximum dry density as determined by standard methods. Additionally, fine particles passing through the 0. 075 mm sieve must not exceed 35% by weight based on the particle size distribution test (Method T 501. 8). For specialized soil materials, the CBR value should be no lower than 8% at 95% of the maximum dry density according to Modified Proctor standards, with swelling limited to a maximum of 3%, in line with the same test method. Other relevant properties should also conform to the specifications outlined in the construction plans.



FIGURE 2-19 Road Embankment Material (Source: to-mats.lnwshop.com)

2.6.2 Road Embankment Side Slope

The side slope ratio of road embankments, as outlined by the Department of Highways (DOH) in Thailand, is influenced by factors like soil type, embankment height, and site conditions. Generally, typical earth embankments have a slope ranging from 1.5:1 to 2:1 (horizontal:vertical). For high embankments or soft soils, a more gradual slope of 2:1 or greater is recommended to promote stability. Conversely, for rock or more stable materials, steeper slopes like 1:1 or 1.5:1 can be employed. Additionally, the shoulder slope is usually designed with a gradient of 4% to 6% for effective drainage. These slope standards are intended to ensure road safety, maintain structural integrity, and manage water runoff efficiently.

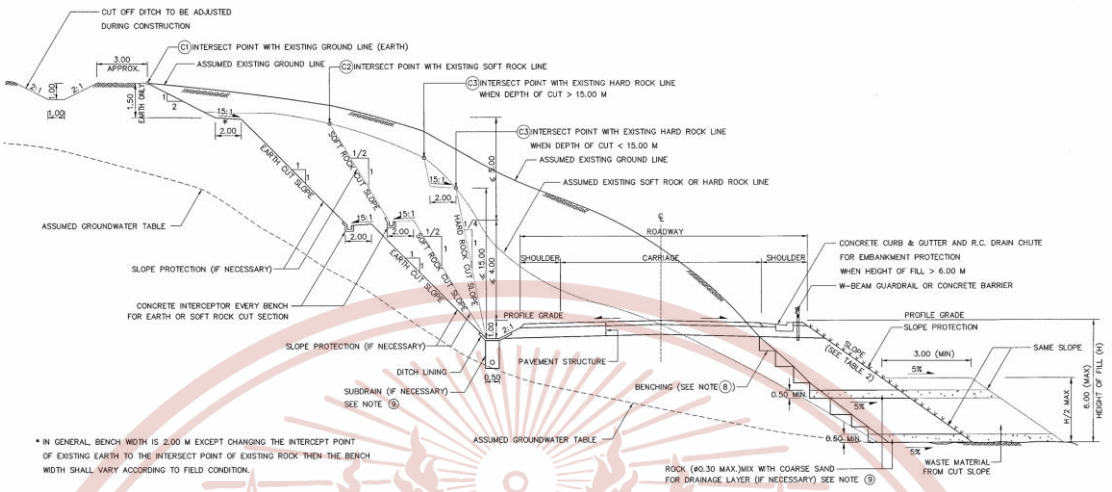


FIGURE 2-20 Road typical cross-section (DOH Thailand standard drawing 2015)

2.7 Erosion Control

There are various methods for preventing soil surface erosion, which can be categorized into **inorganic** and **organic** approaches (Gray and Sotir, 1996). Inorganic methods include the use of **shotcrete, rock riprap,** and **gabions**. These techniques are generally effective when properly applied; however, they are typically costly and require integrated drainage systems. If drainage becomes blocked, water pressure may build up within the soil mass, potentially leading to structural damage. On the other hand, **organic methods**, such as **planting ground cover vegetation** and using **erosion control blankets made from natural fibers** in combination with vegetation, offer a more sustainable long-term solution. However, these methods require time for plant root systems to establish before they can effectively reduce erosion and shallow mass movement.

2.7.1 Planting ground cover

(M.T.C.H. 201-2545), Materials must have a Plasticity Index (PI) of zero and be free from clay lumps, topsoil, tree roots, leaves, or decomposed organic materials that may lead to future settlement. The particle size should not exceed 9.5 millimeters (3/8 inch). Additionally, fine particles passing through a 0.075- millimeter (No. 200) sieve must comprise no more than

20% by weight, as determined by the particle size distribution test (Method T501.8). The California Bearing Ratio (CBR) value obtained from laboratory tests must be at least 10% at 95% of the maximum dry density, as established by the Modified Proctor method (Method T 501.3) or as per the construction plans. Other material properties must meet the requirements set forth in the construction specifications.

Vegetation plays a vital role in mitigating soil erosion caused by rainfall. The removal of plant cover whether by human activity such as deforestation or through natural processes like wildfires significantly increases the susceptibility of surface soils to erosion. Therefore, implementing conservation strategies or re-establishing vegetation in disturbed areas can effectively reduce topsoil loss and surface runoff. Certain grass species, particularly some cultivars of *Vetiveria zizanioides* (Vetiver grass), have been found to be especially effective due to their deep and dense root systems. These roots help reduce soil moisture content through water uptake, maintaining an unsaturated condition in the soil that contributes to slope stability. According to the Chaipattana Foundation (1996) and Voottipruex et al. (2008), Vetiver grass can reduce surface runoff by up to 73% and decrease soil erosion by as much as 95%.

Brachiaria ruziziensis (commonly known as Ruzi grass) has also been identified as an effective species for pasture improvement in tropical regions. It is propagated through seeds, which are relatively easy to establish in areas with high rainfall, and has been widely adopted in Thailand for erosion control and soil improvement purposes (Artidteang et al., 2016).

The use of vegetation for slope stabilization is commonly implemented through bioengineering techniques, which integrate plant-based methods with structural measures in a way that complements the natural landscape and local environmental conditions. These approaches not only enhance slope stability but also promote long-term soil and water conservation, especially in steep terrains (Thavorn et al., 2013). Erosion

control mechanisms associated with vegetation operate both above and below the soil surface. Above ground, dense and closely planted clumps of Vetiver grass act as natural barriers, slowing surface runoff and capturing sediments, organic matter, and nutrients. Over time, as sediment accumulates, the grass adjusts by producing new shoots above the rising soil surface. Below ground, Vetiver's root system extends both vertically and laterally up to approximately 50 centimeters forming a fibrous, interlocking network that reinforces the soil and effectively prevents erosion and shallow mass movement (Montri and Kritsada, 2003).

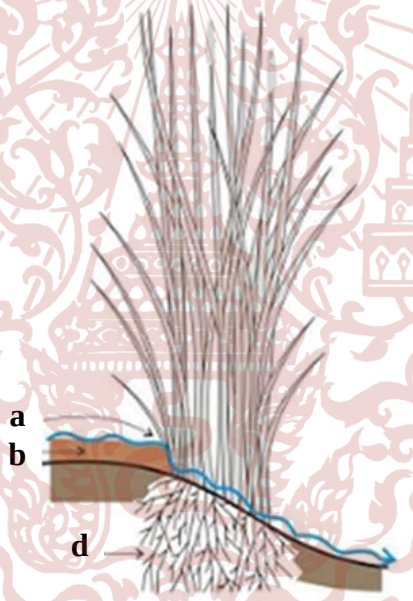


FIGURE 2-21 Model of the Interaction Behavior Between Soil and Vetiver Roots (Source: Montri & Kritsada, 2003)

2.7.2 Root reinforcement

Plant roots are essential for enhancing the mechanical stability of soils. A robust root system increases the confining stress within the soil mass by creating an interlocking network that binds soil particles together. This interaction between roots and soil boosts the overall shear strength of the soil. The presence of roots can be likened to an increase in soil cohesion. Wu et al.

(1979) indicated that plant roots provide an apparent cohesion, commonly known as root cohesion (Cr), which is affected by factors such as root tensile strength, root diameter, and root density—attributes that generally increase with the age of the plant. As stated by Coppin and Richards (1990), the value of root cohesion (Cr) may vary from 1 kPa to 17.5 kPa, depending on the specific plant species and soil characteristics. Additionally,

Panich Wuttipruk et al. (2005) introduced an empirical equation for estimating Cr in relation to slope stability analysis. In this context, roots serve as reinforcing agents that enhance the soil's resistance to shear forces, contributing to better slope stability and reduced susceptibility to failure. as shown in

$$\tau_{sr} = c_s + c_r + \sigma \tan\phi$$

$$C_r = t_r \left(\cos\theta \bullet \tan\phi' + \sin\theta\right)$$

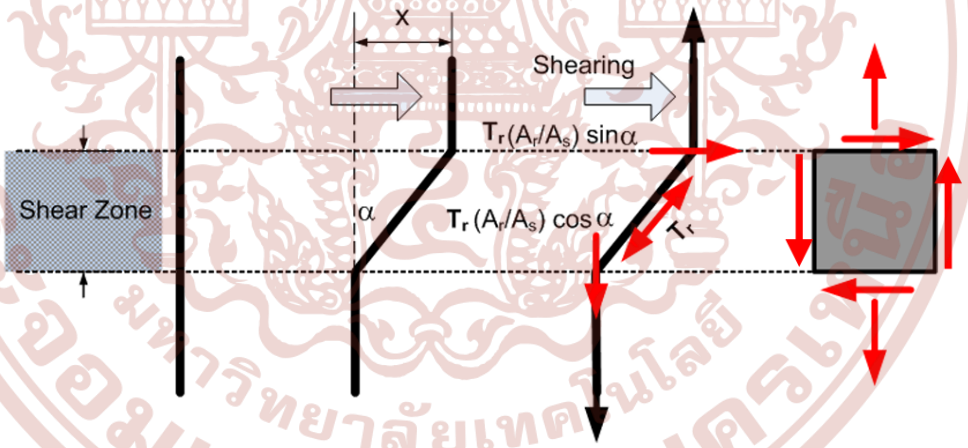


FIGURE 2-22 Model of root reinforcement in shear zone (Wu, 1976; Gray and Ohashi, 1983; Schmidt, Roering, et al., 2001)

2.8 Wedelia trilobata

Wedelia trilobata (syn. *Sphagneticola trilobata* (L.) Pruski), commonly known as creeping daisy or Singapore daisy, is a perennial herbaceous species of the family Asteraceae. It is native to tropical Central America and the Caribbean, extending from

Mexico to northern South America, and has been introduced globally as a popular ornamental ground cover (CABI, 2024; GISD, 2024). Historically, the species was classified under the genus *Wedelia*; however, molecular and morphological evidence has led to its reclassification under *Sphagneticola*, reflecting the polyphyletic nature of *Wedelia* sensu lato (Almeida et al., 2024). Phylogenetic analyses of the subtribe Ecliptinae (tribe Heliantheae, Asteraceae) confirmed that *Sphagneticola* forms a monophyletic lineage distinct from other *Wedelia* taxa (Almeida et al., 2024; PhytoKeys, 2023).

Molecular phylogenetic studies have provided significant insights into the evolutionary trajectory of *S. trilobata*. Almeida et al. (2024) demonstrated, through multilocus phylogeny and biogeographic reconstruction, that *Sphagneticola* originated in the Neotropical region before dispersing into other tropical regions.

Further studies have focused on the species' genetic adaptability. Xiao et al. (2023) revealed notable levels of genetic and epigenetic variation among *S. trilobata* populations, indicating that epigenetic plasticity may enhance its adaptive potential in novel environments. Such genetic flexibility, coupled with efficient vegetative propagation, contributes to its invasive success.

Ecological studies highlight the species' exceptional adaptability and competitive traits. *Sphagneticola trilobata* primarily reproduces vegetatively through stem fragmentation and rooting, forming dense mats that outcompete native flora (CABI, 2024; GISD, 2024). Javed et al. (2020) reported that *W.trilobata* exhibits strong morphological plasticity and superior competitive ability under varying environmental conditions. Additionally, its interactions with endophytic microorganisms and possible hybridization with native congeners may further promote local adaptation and ecological dominance (Xiao et al., 2023). These factors collectively underpin its successful naturalization across Asia, Africa, and the Pacific.

Currently, *Sphagneticola trilobata* is listed among the "100 of the World's Worst Invasive Alien Species" (GISD, 2024). It aggressively invades disturbed ecosystems such as roadsides, riverbanks, and coastal dunes, forming thick vegetative mats that suppress native regeneration and alter community structure (CABI, 2024). Its

rapid vegetative spread and allelopathic potential make it a major ecological concern in tropical ecosystems. To mitigate its spread, management programs emphasize early detection, physical removal, and ecological restoration of invaded areas (CABI, 2024; GISD, 2024). These strategies underscore the importance of integrating molecular, ecological, and management perspectives to address the species' ongoing invasion.



FIGURE 2-23 Wedelia trilobata (Sphagneticola trilobata)

2.9 Photogrammetry

Photogrammetry originates from the Greek words Phos (light), Gramma (drawing or writing), and Metron (measurement), which collectively refer to the technique of "measuring with light." According to Paisarn Santithammanont (2010), photogrammetry is defined as a science and technology utilized for surveying and mapping, serving as a method for generating geospatial information. This technique employs imagery to survey and document surface features, such as land cover, land use, buildings, infrastructure, and specific objects of interest. These features are captured as three-dimensional (3D) models, enabling users to virtually revisit conditions when the images were taken. Photogrammetry represents both a science and an art, involving intricate processes that necessitate advanced calculations, specialized optical and mechanical devices, and thorough understanding, training, and experience.

Contemporary photogrammetry further incorporates computer systems and advanced software for data processing and interpretation. The results from photogrammetric processing yield 3D coordinates, object dimensions, and shapes, with some systems also integrating surface texture data to create highly realistic 3D models. One significant advantage of photogrammetry is that surveyors can measure objects remotely without needing physical contact. Data can be collected quickly and efficiently over extensive areas. However, the whole process demands precision and expertise, since the goals of each model may differ based on specific applications. Software such as Agisoft Metashape supports various model applications, and a proper grasp of parameter settings is crucial—for instance, generating topographic maps often requires height field models or the placement of markers to enhance spatial accuracy.

Schenk (2005) noted that photogrammetry combines numerous images to reconstruct 3D data. In expansive open areas, natural lighting is vital for capturing fine details, as photogrammetry depends on image consistency taken concurrently and under similar lighting conditions. A minimum image overlap of 60% is necessary to achieve precise 3D reconstruction.

Albertz (2007) chronicled the historical progression of photogrammetry, tracing its origins to 1840 when Aimé Laussedat, a French scientist, conducted pioneering experiments with image-based surveying. He introduced the term Iconometrie to describe his technique, which involved reading images and manual perspective sketching with a device known as Camera Lucida, the forerunner of modern photogrammetric cameras. He subsequently renamed the discipline Metrophotographie. Laussedat's contributions gained recognition through his publication Die Photometrographie in the journal Wochenblatt des Architektenvereins zu Berlin. He later produced aerial photographs documenting Paris from rooftop perspectives, which were displayed at the 1867 Paris Exposition, earning him the title of "Father of Photogrammetry."

The progression of photogrammetry experienced a significant boost due to technological advances in computers and the onset of digital cameras, which established the groundwork for present-day Digital Photogrammetry. In 1996, the

International Society for Photogrammetry and Remote Sensing (ISPRS) proclaimed the slogan “Digital photogrammetry ready for take off” at its congress in Vienna, Austria.

Beraldin (2004) examined the progress of 3D modeling technologies through laser scanning and close-range photogrammetry, highlighting their expanding applications and future potential in several sectors.

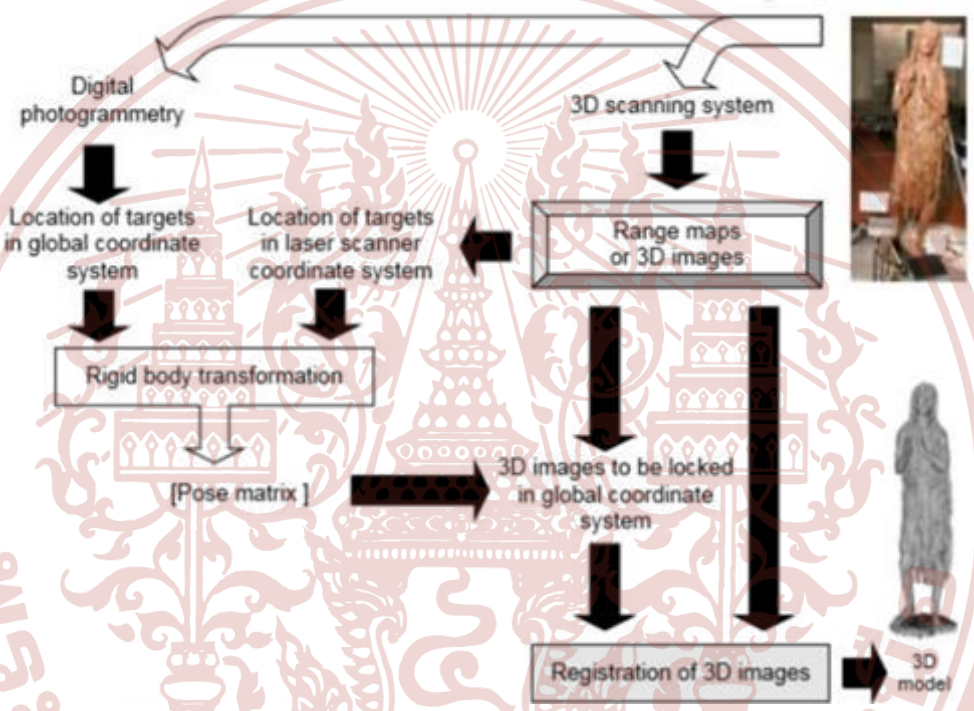


FIGURE 2-24 Example of data processing and integration using photogrammetry and 3D scanning systems.(Source: Beraldin, 2004)

A study was conducted to assess soil erosion in the Kuro-dake campsite area within Daisetsuzan National Park, Japan. The research utilized Structure-from-Motion (SfM) photogrammetry along with ground control points (GCPs) to create high-resolution digital elevation models (DEMs) with spatial resolutions between 0.015 and 0.025 meters. By comparing DEMs produced at various time intervals, the researchers accurately evaluated changes in surface elevation and quantified soil loss over time. The findings showed that SfM photogrammetry serves as an effective and precise method for identifying and tracking campsite-induced erosion,

providing a non-invasive, cost-effective solution for environmental management in protected area.

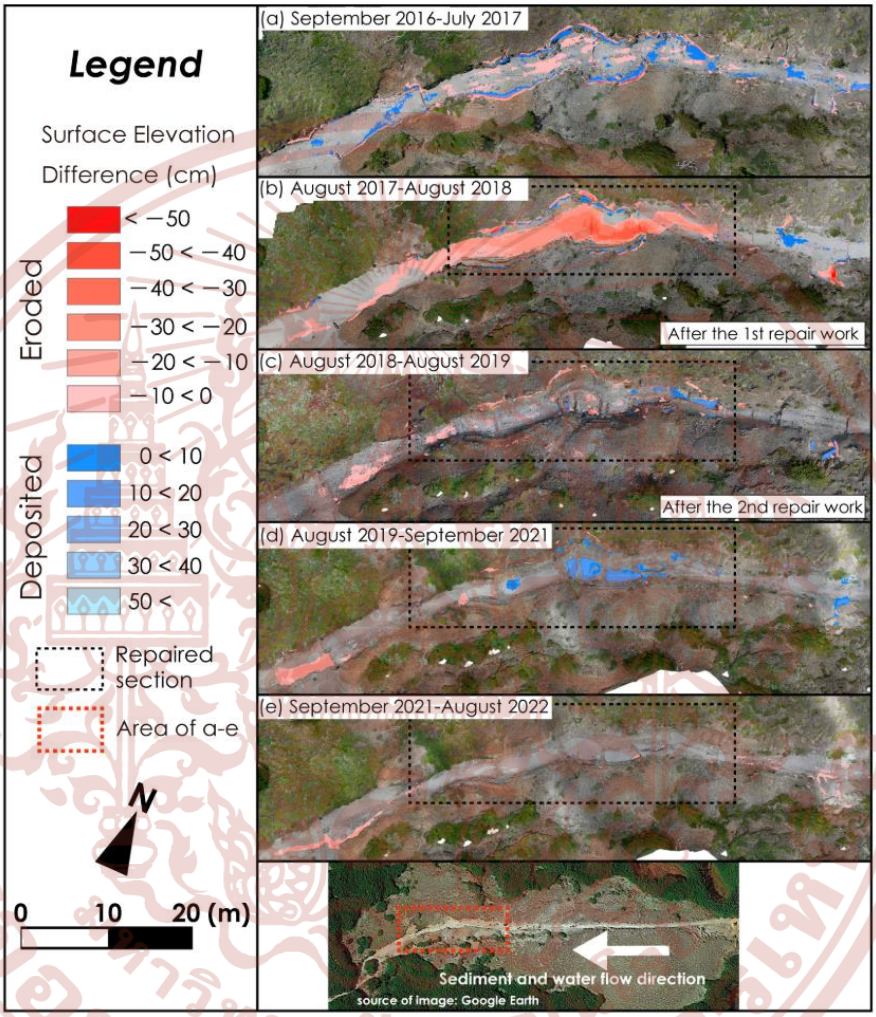


FIGURE 2-25 The trail surface changed from 2016 to 2022 in the section repaired in August 2016 and August 2017 Source:(Kobayashi and Watanabe 2023)

2.10 LiDAR and Close range photogrammetry

Light Detection and Ranging (LiDAR) technology determines distance by measuring the travel time of laser pulses between the sensor and the target surface. The range RRR is computed as R=(c×Δt)/2R = (c \times \Delta t)/2R=(c×Δt)/2, where ccc is the speed of light and Δt\Delta tΔt is the two-way travel time of the pulse. Modern

airborne and terrestrial LiDAR systems emit up to several million laser pulses per second, each pulse providing a precise 3D point when combined with position and orientation information from the Global Navigation Satellite System (GNSS) and Inertial Measurement Unit (IMU) (Aguilar et al., 2010; NOAA, 2012). After acquisition, LiDAR point clouds are processed through filtering, classification, and interpolation steps to extract ground points and reconstruct the bare-earth surface. Common interpolation techniques include Triangulated Irregular Network (TIN) formation, kriging, or inverse distance weighting (IDW), which generate a continuous Digital Elevation Model (DEM) from discrete ground points. The accuracy of LiDAR-derived DEMs depends on pulse density, flight altitude, surface roughness, and classification algorithms (Aguilar et al., 2010).

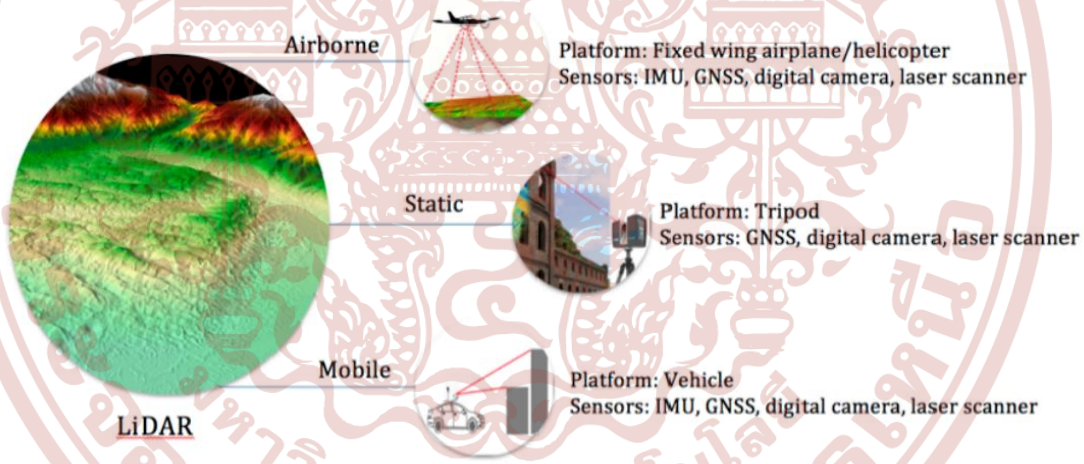


FIGURE 2-26 Light detection and ranging (LiDAR) survey data acquisition (Muhadi et al. 2020)

Close-range photogrammetry, particularly Structure-from-Motion (SfM) combined with Multi-View Stereo (MVS), reconstructs three-dimensional geometry by identifying and matching common features across multiple overlapping images (Westoby et al., 2012). The relative position and orientation of each image are refined using bundle adjustment, which minimizes reprojection error to achieve

consistent camera geometry. Distances to scene points are derived through geometric triangulation, where intersecting image rays from multiple viewpoints define each 3D point (Goetz et al., 2018) To convert relative coordinates to a real-world reference frame, Ground Control Points (GCPs) or GNSS measurements are introduced, allowing georeferenced and scaled DEM generation. Postprocessing steps, such as point cloud densification, noise filtering, and surface interpolation, follow similar workflows to LiDAR-derived DEM production, although SfM accuracy is more sensitive to lighting, image overlap, and surface texture (Bhushan et al., 2021).

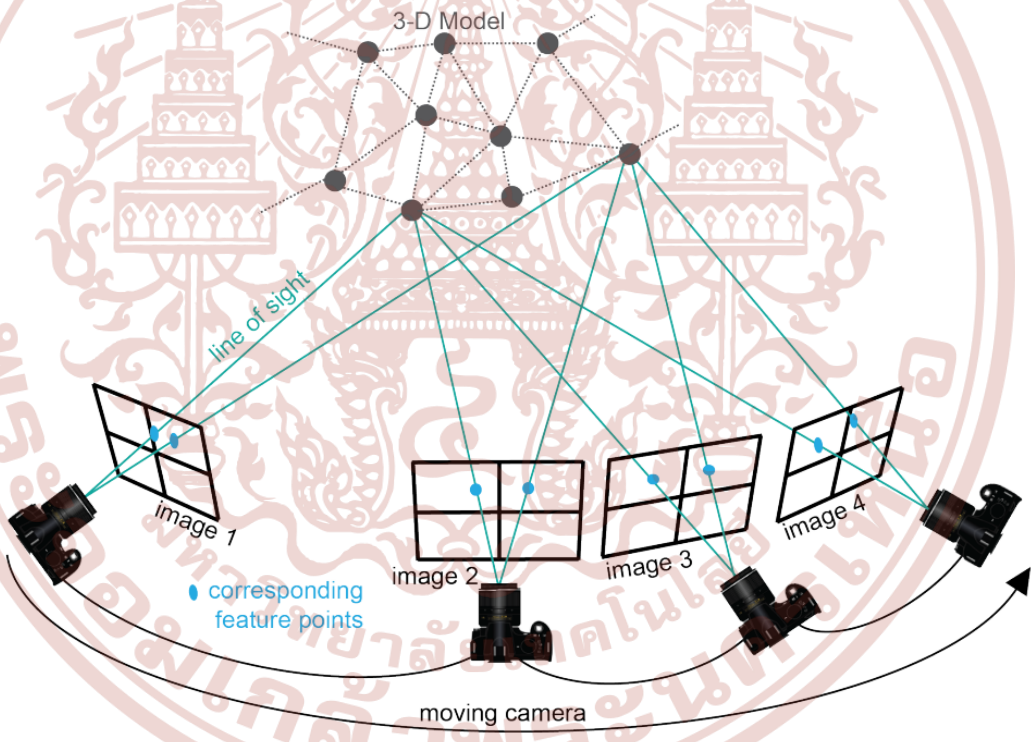


FIGURE 2-27 Schematic of Structure from Motion (SfM) method. Photographs are taken at a variety of orientations; the matched features in multiple photographs are used to estimate relative camera position, which is then extrapolated to create a point cloud, or 3D model, of the scene. (Figure modified from Chris Sweeney, UCSB).

Both LiDAR and photogrammetric workflows converge on a similar DEM production pipeline: (1) sensor orientation and georeferencing, (2) point cloud generation and cleaning, (3) classification of ground versus non-ground points, and (4) interpolation into a continuous elevation raster (Aguilar et al., 2010; Westoby et al., 2012). DEM accuracy depends on sampling density, acquisition geometry, and the interpolation algorithm used. Fusion approaches—integrating LiDAR and photogrammetric point clouds—can enhance vertical accuracy and spatial completeness while reducing uncertainty in complex terrains (Goetz et al., 2018). Validation using independent checkpoints remains essential for quantifying vertical and horizontal errors in DEM products.

CHAPTER 3

METHODOLOGY

To study the effectiveness of Wedelia Tribata for slope erosion control at varying densities for reduction in runoff, soil erosion, and Inflitation, These experiments were conducted under simulated rainfall using Keifer and Chu's method to design artificial rainfall. in terms of Erosion Pattern, using photography techniques to assess the erosion pattern based on the Digital Elevation Model (DEM). Including to define The Root properties was adopted to grow with rice husk ash and laterite soil in a rhizobox system to define Root system architecture characteristics of Wedelia Trilobata following root system architecture characteristics in each soil type. After that collected roots from rhizoboxes were measured for tensile strength by using a universal testing machine.

3.1 Testing Standard

To study basic properties of soil for testing erosion under simulated rainfall

TABLE 3-1 Criteria for testing engineering properties

Sequence	Equipment, tools and testing methods	Testing Standard
1	Atterberg Limits	ATSM-D 427
2	Grain Size Determination of Sieve Analysis	ASTM D-422
3	Determination of Compaction Test	ASTM D1557-15
4	Direct Shear Test	ASTM D 3080-98
5	Scanning Electron Microscope	-

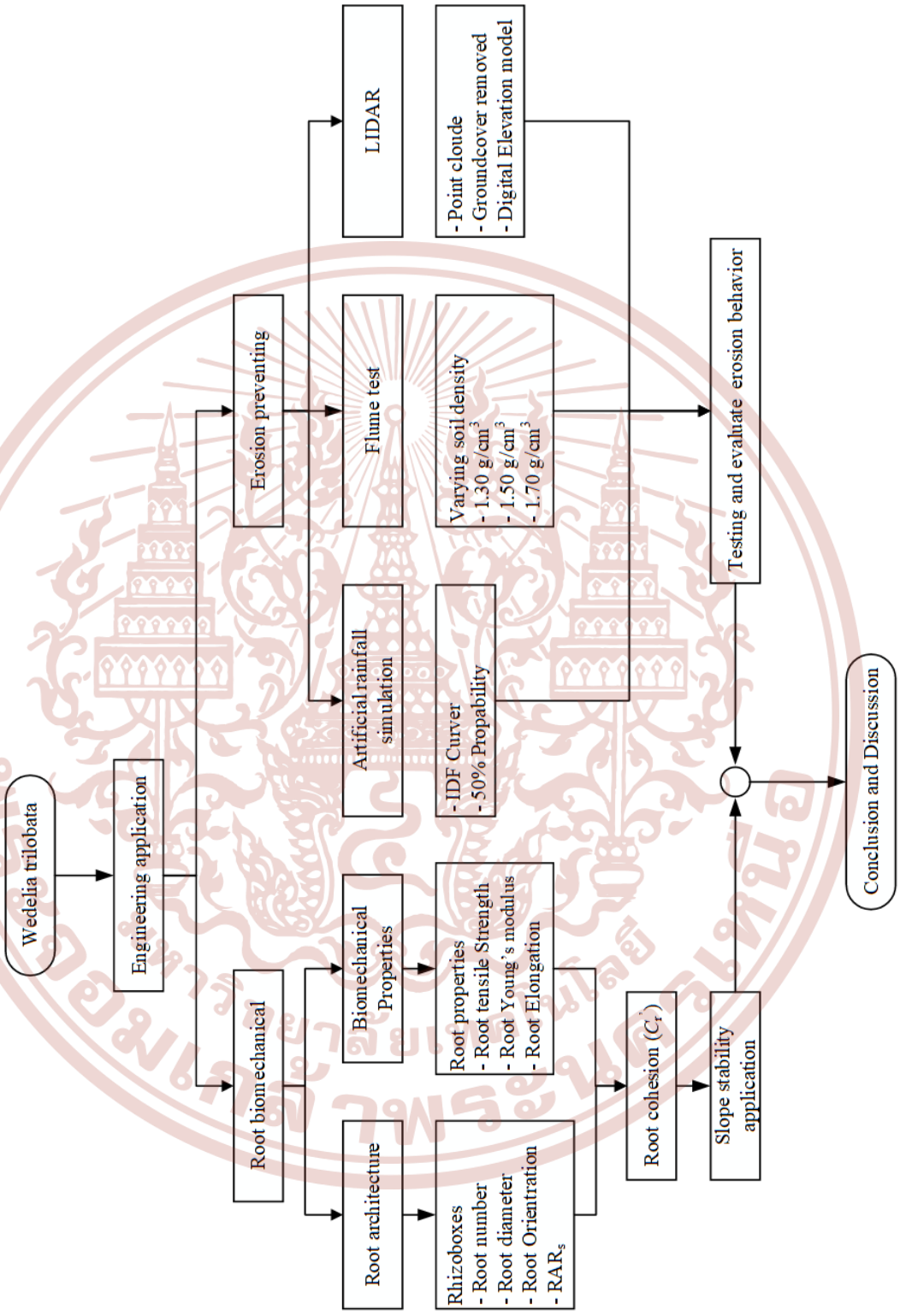


FIGURE 3-1 Flowchart

3.2 Test Material

This study requires an analysis of the materials' properties. It examines two types of soil: 1. Laterite Soil and 2. Rice Husk Ash, both of which need an assessment of their fundamental engineering characteristics. For Laterite Soil, it is essential to explore the basic engineering properties and the optimal moisture content of both the Laterite Soil and Rice Husk Ash.

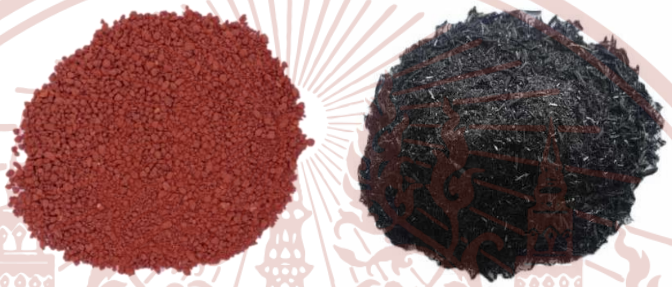


FIGURE 3-2 Laterite soil and Rice husk ash

3.2.1 Atterberg Limit

Test according to ASTM standard: D 4318-84 to determine the moisture content in the soil mass from the viscous fluid state to the semi-solid state.From a viscous fluid state to a semi-solid state, which includes the following tests The following tests



FIGURE 3-3 Casagrande Apparatus

1. Liquid Limit (LL)

Test according to ASTM standard: D 4318-84 to find the amount of water present in the soil that will make the soil transition from a plastic state to a liquid state. To determine the water content at which the soil changes from a plastic state to a liquid state, expressed as a percentage of the dry weight of the soil. The experiment can be conducted by taking a soil sample that has passed through a 40-mesh sieve, mixing it with water, and then placing it in the testing apparatus.(Liquid Limit Apparatus) Smooth the surface and divide the soil into two parts with a Grooving Tool. Let the test cup impact the machine base at a speed of 2 times per second, a total of 25 times, at the impact distance. Maximum 10 millimeters until the separated soil moves to a distance of 12.7 millimeters. Take the soil sample. Dry to calculate the moisture content.

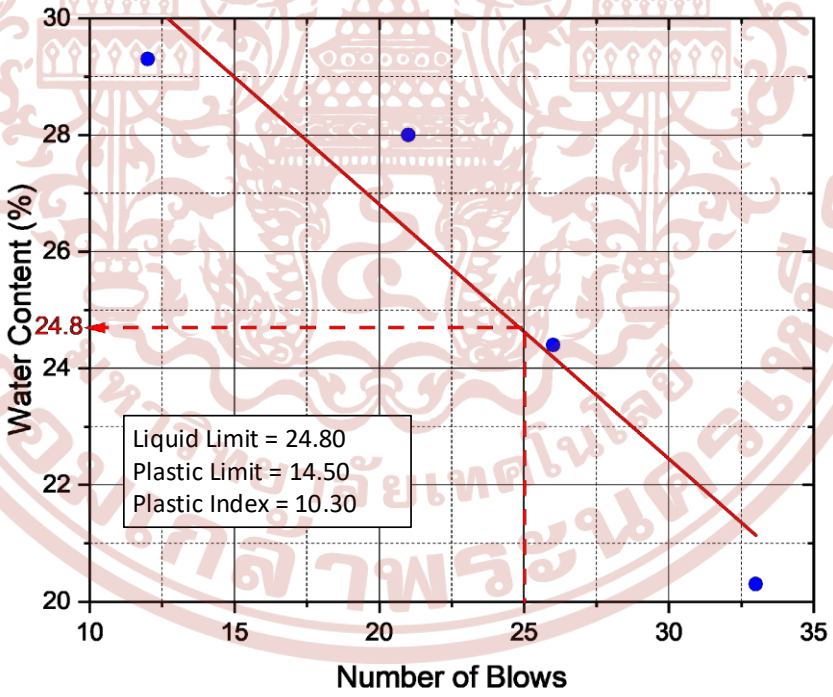


FIGURE 3-4 Atterberg Limit Result

2. Plastic Limit (PL)

According to the ASTM testing standard: D 4318-84, it determines the amount of water present in the soil during the transition from the plastic state to the semi-solid state. The test is conducted by rolling the soil to a diameter of 3.2 millimeters until cracks begin to form. The moisture content of the soil calculated at this point is the plastic limit of the soil used in the test.

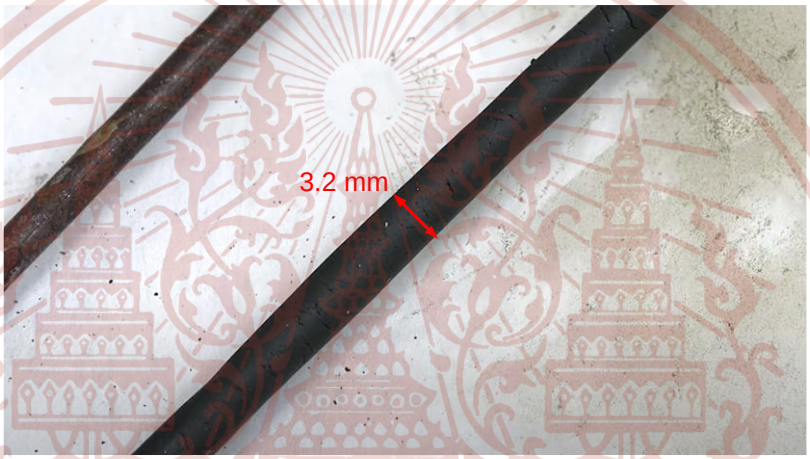


FIGURE 3-5 Plastic limit sample

3.2.2 Sieve Analysis

Testing for particle size distribution consists of testing for soil particle size using the sieve analysis method according to the standard. ASTM D6913 and the hydrometer tests according to ASTM D 422-63 standard are used to classify and identify soil types based on soil particle size, including gravel, Sand, silt, and clay



FIGURE 3-6 Laterite soil grain size

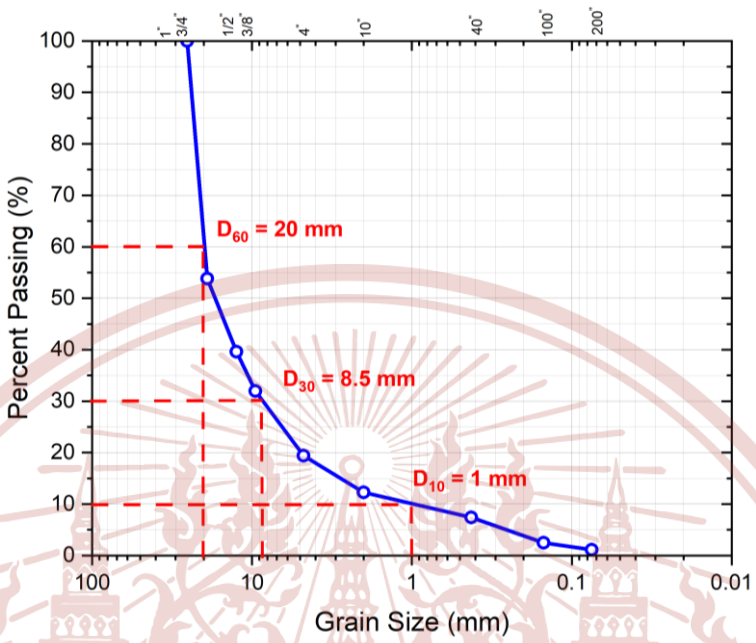


FIGURE 3-7 Show the particle size distribution

In Thailand, the Department of Highways (DOH) sets specific gradation requirements for various construction materials used in road infrastructure projects. These specifications are crucial for ensuring the quality, performance, and durability of pavement layers, embankments, and other road components. For research focused on materials used in Thai road construction, it is imperative to refer to the latest editions of the Department of Highways Standard Specifications for Highway Construction.

TABLE 3-2 Specified particle size distribution Standard No. of DH-S 205/2532

Sieve Size		Percentage by Mass Passing Sieve				
(Millimeters)	(Inches / Mesh)	A	B	C	D	E
50	(2")	100	100	-	-	-
25	(1")	-	-	100	100	100
9.5	(3/8")	30-65	40-75	50-85	60-100	-
2	(No. 10)	15-40	20-45	25-50	40-70	40-100
0.425	(No. 40)	8-20	15-30	15-30	25-45	20-50
0.075	(No. 200)	2-8	5-20	5-15	5-20	6-20

3.2.3 Compaction Test

The optimum moisture content and maximum dry density are determined through the Standard Compaction Test, following the (ASTM D698/AASHTO T99), to establish the relationship between dry density and moisture content of the soil. This involves specific criteria outlined in Table 3-3 In this research,

TABLE 3-3 Criteria for testing soil standard compaction.

Specification	**Method C**
Dimension Mold	101.6 mm
Volume of Mold	941.5 cm^3
Hammer weight	2.5 kg
Hammer dropped	305 mm
Blows per layer	25
Layers	3
Energy	595 kJ/m^3
Soil	Passing sieve No. 4

The moisture content used for testing soil compaction higher than the standard includes levels at 6, 8, 10, 12, and 14 percent. The optimum moisture content can be determined by plotting a graph depicting the relationship between the dry density of the soil and the moisture content during soil compaction. The moisture content corresponding to the maximum dry density will be considered the optimum moisture content. All tests in this research will utilize the maximum dry density after compaction $\rho_{dry\ (max)}$ and the value of Optimum Moisture Content (OMC) obtained from these tests.

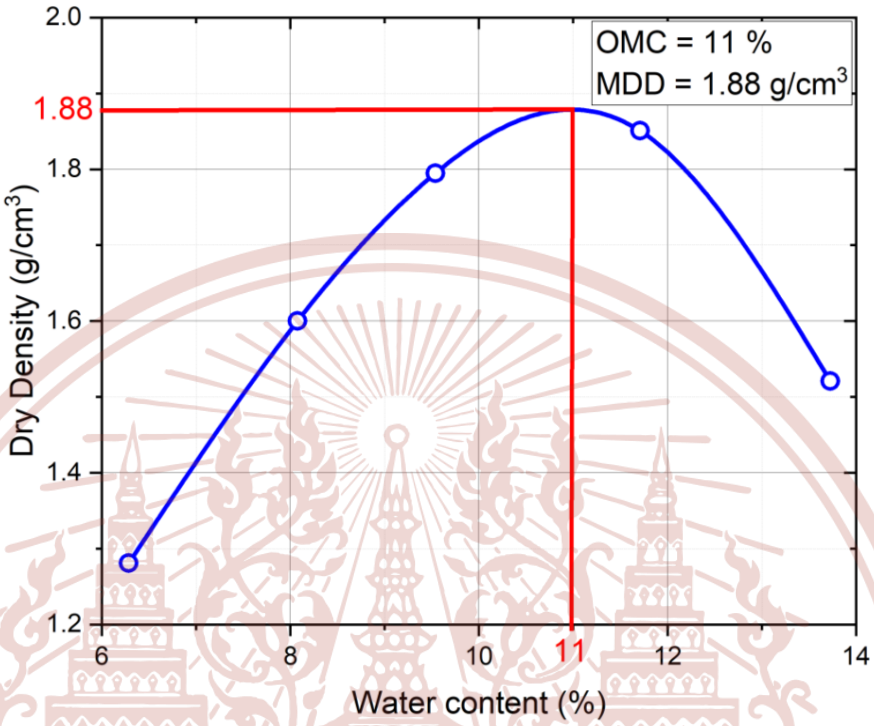


FIGURE 3-8 Show the Maximum dry density and Optimum moisture content

3.2.4 Direct Shear Test

The Direct Shear Test, conducted in accordance with ASTM D3080, is a fundamental laboratory method used to determine the shear strength of soil. This test is specifically designed to impose a direct shear plane within a soil specimen, allowing for precise measurement of its resistance to shear forces.

ASTM D3080 specifies that both square and circular shear boxes can be used. Common specimen dimensions for the direct shear test are typically 60 mm x 60 mm or 100 mm x 100 mm for square specimens, and 50 mm or 60 mm in diameter for circular specimens. The standard also recommends that the specimen width (or diameter) should be at least 10 times the maximum particle size (D_{max}) to minimize boundary effects and ensure a more uniform stress distribution. The height of the specimen is typically one-half of its width, to maintain a suitable aspect ratio. For

research involving coarser-grained soils, larger shear boxes might be necessary to accommodate the particle size requirements.

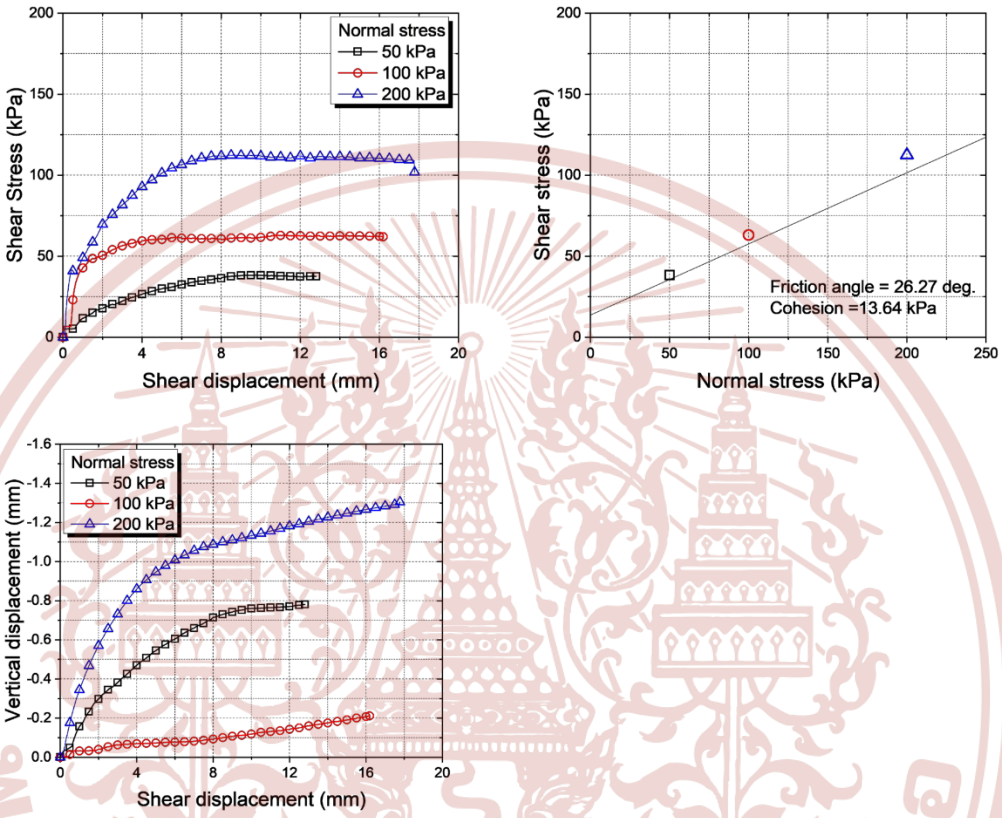


FIGURE 3-9 Show Cohesion and internal friction angle

3.2.5 Soil Analysis for Micro-Structural and Elemental Composition (Scanning Electron Microscopy - SEM)

This section details the methodology for analyzing soil samples using Scanning Electron Microscopy (SEM) coupled with Energy Dispersive X-ray Spectroscopy (EDS) to investigate their micro-structural characteristics and elemental composition. While the initial prompt mentions "nutrients," SEM-EDS primarily focuses on morphology and elemental makeup rather than direct nutrient quantification.

For the SEM-EDS analysis, a representative composite sample was prepared from each area. The researcher collected samples from at least two distinct points within

the same area. These two samples were then thoroughly homogenized to create a single representative sample for that specific location.

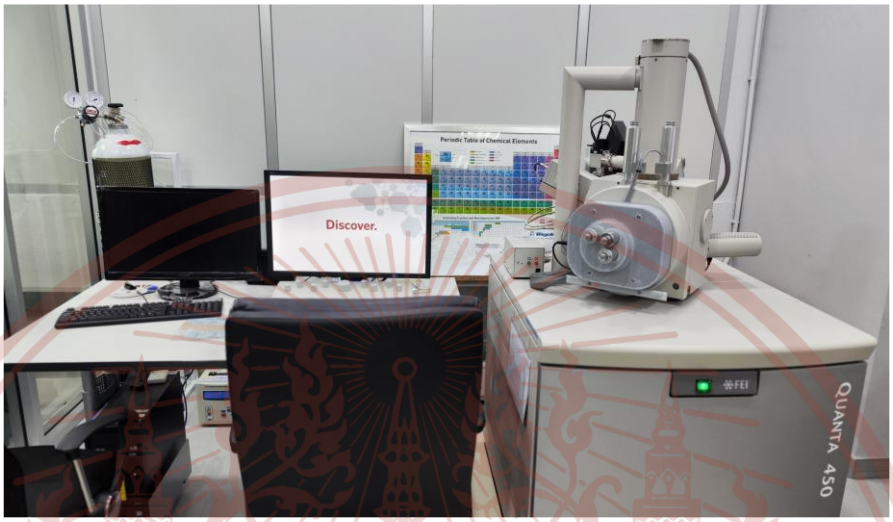


FIGURE 3-10 SEM & EDX (QUANTA 450)

The prepared soil samples were analyzed using a Scanning Electron Microscope (SEM), specifically a Tescan Mira 3 model, equipped with an Energy Dispersive X-ray Spectroscopy (EDS) system. The SEM was operated at an accelerating voltage of 25 kV in high vacuum (HV) mode. Micro-structural characteristics of the soil particles were observed and analyzed at magnifications of 150x and 500x. The integrated EDS system was utilized to perform elemental mapping and quantitative analysis of the soil's constituent elements, providing insights into the mineralogical and chemical composition of the particles.

TABLE 3-4 Soil Nutrient Results of Laterite soil and Rice husk ash

Element	Laterite soil			Rice husk ash		
	Weight %	Atomic %	Net Int.	Weight %	Atomic %	Net Int.
N K	1.0	1.4	0.9	1.6	2.2	2.6
P K	2.1	1.4	5.1	0.6	0.4	2.5
K K	2.0	1.1	4.1	0.9	0.5	3.0

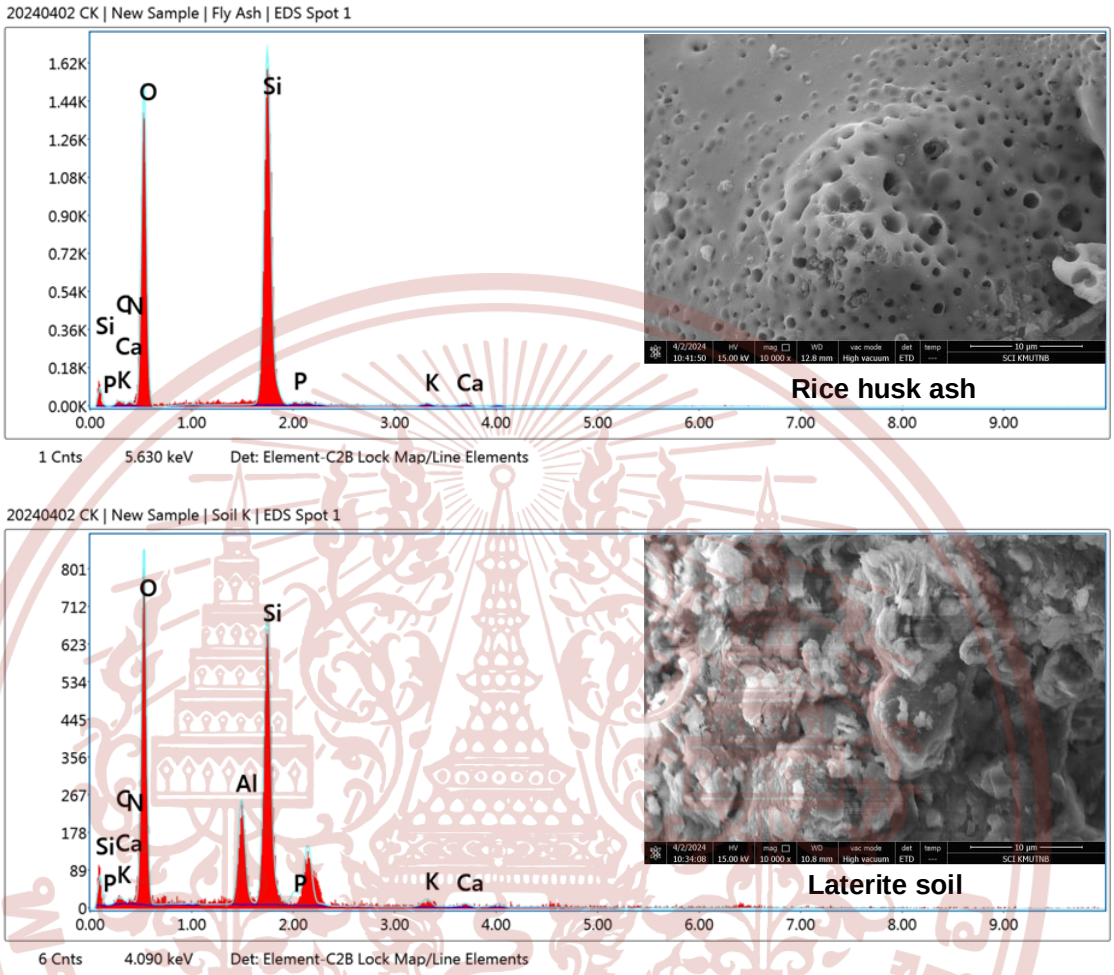


FIGURE 3-11 SEM & EDX Result of Laterite soil and Rice husk ash

3.3 Experimental Procedure for Cultivating Wedelia trilobata

wedelia trilobata cultivation experiment, plants were grown in a greenhouse to control environmental conditions as shown in Figure 3-9a, including daily water supply. Subsequently, the growth of Wedelia trilobata was observed using different soil types and proportions. This preliminary cultivation aimed to select the optimal soil ratio for good plant growth as shown in Figure 3-9b, before the plants were transplanted for the actual testing in the next phase. After that lateritic soil, Rice husk ash and potting soil were sieved through a No. 4 sieve. The sieved soils were then mixed in the following lateritic soil to potting soil ratios: 1:0, 1:1, 1:2, and 1:4. The soil mixtures were thoroughly homogenized and then used to fill small pots for planting. The

propagation of Wedelia trilobata was carried out using stem cuttings. Cuttings approximately 10 cm in length were taken from the brownish, more mature sections of the stems. These cuttings were then soaked in a rooting hormone solution for at least 12 hours before being planted in the prepared soil as shown in Figure 3-9c. plant growth within the greenhouse was observed. During this period, the plants were watered daily using a misting system for 5 minutes. Observations were recorded at 1-week, 2-week, and 3 weeks intervals as shown in Figure 3-9d

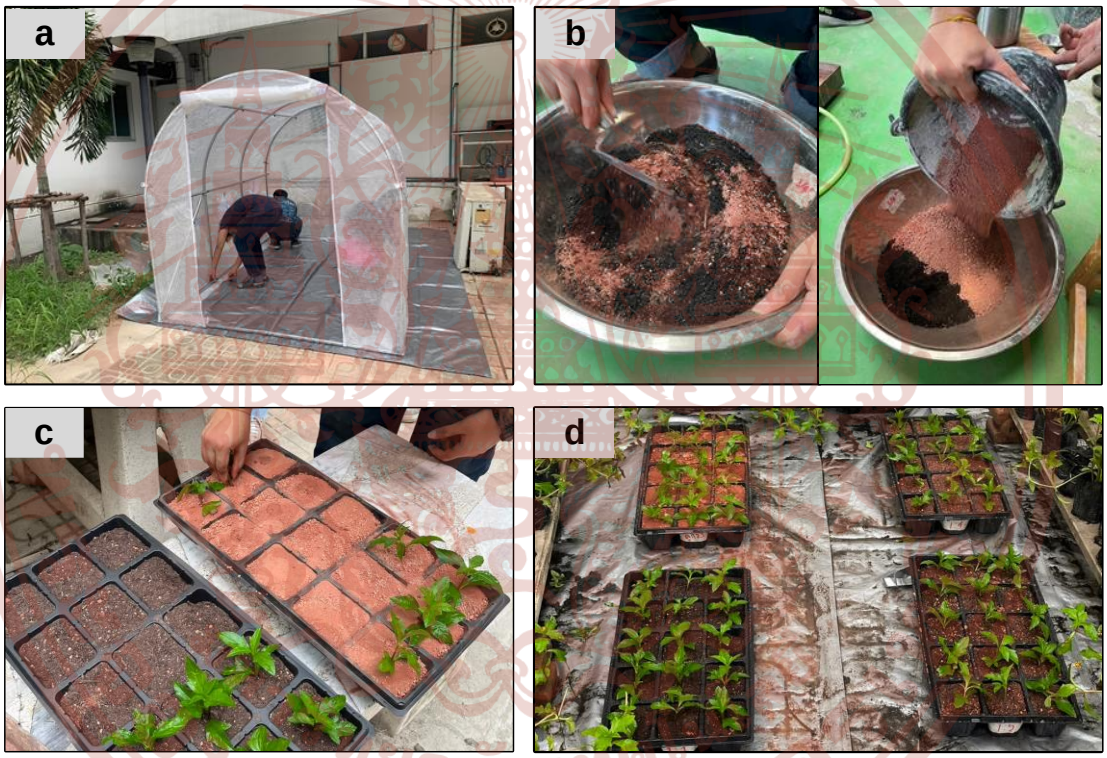


FIGURE 3-12 Experimental Procedure for Cultivating Wedelia trilobata

3.4 Preparation of the Erosion Testing Flume

For this research, a testing flume with dimensions of 0.65 x 2.50 x 0.3 m will be used, as shown in Figure 3-10a. Prior to testing, both the flume and the underlying filter layer mesh must be thoroughly cleaned, as depicted in Figure 3-10b and 3-10c

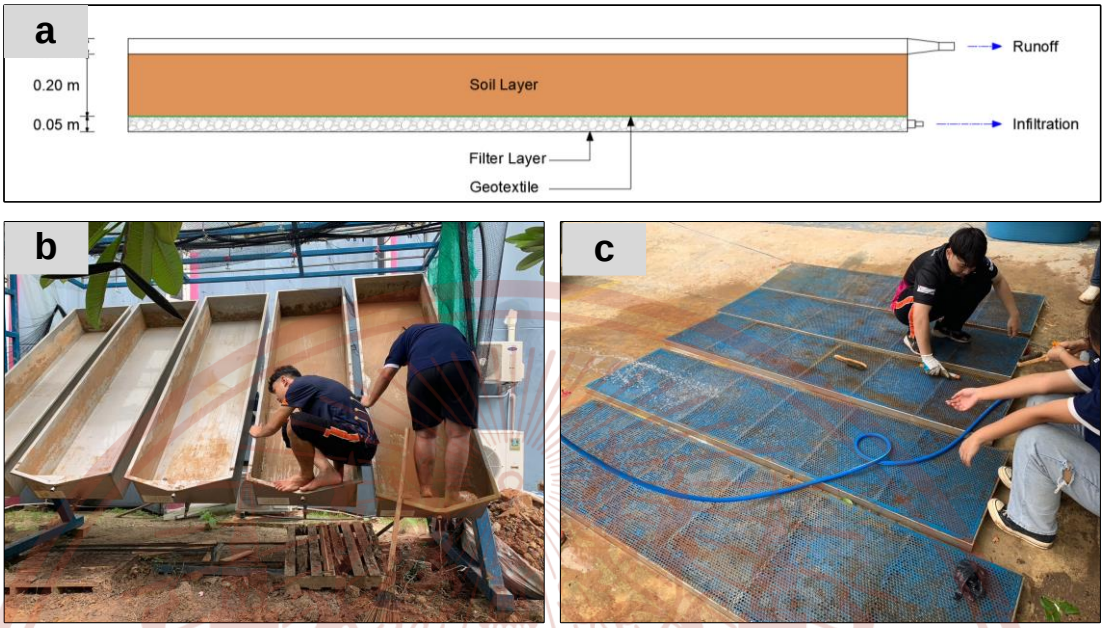


FIGURE 3-13 Preparation of testing flume

3.5 Preparation of Artificial rainfall

The design of artificial rainfall systems can vary significantly to suit different experimental requirements. While methods like drip irrigation exist, a nozzle-based system offers greater complexity in simulating droplet aggregation, allowing for the integration into artificial rainfall simulation systems that control various environmental components (humidity, sunlight, temperature). The impact distance of raindrops is a crucial factor influencing their impact velocity.

In this study, the rain distribution system was designed to produce droplets approximately 2-5 mm in size, achieved by selecting sprinkler nozzles that emit spray as close as possible to this specified size. Water is drawn from a storage tank and then pressurized by a pump. The pressure is precisely controlled by a pressure valve before the water enters the sprinklers, as illustrated in Figure 3-11.

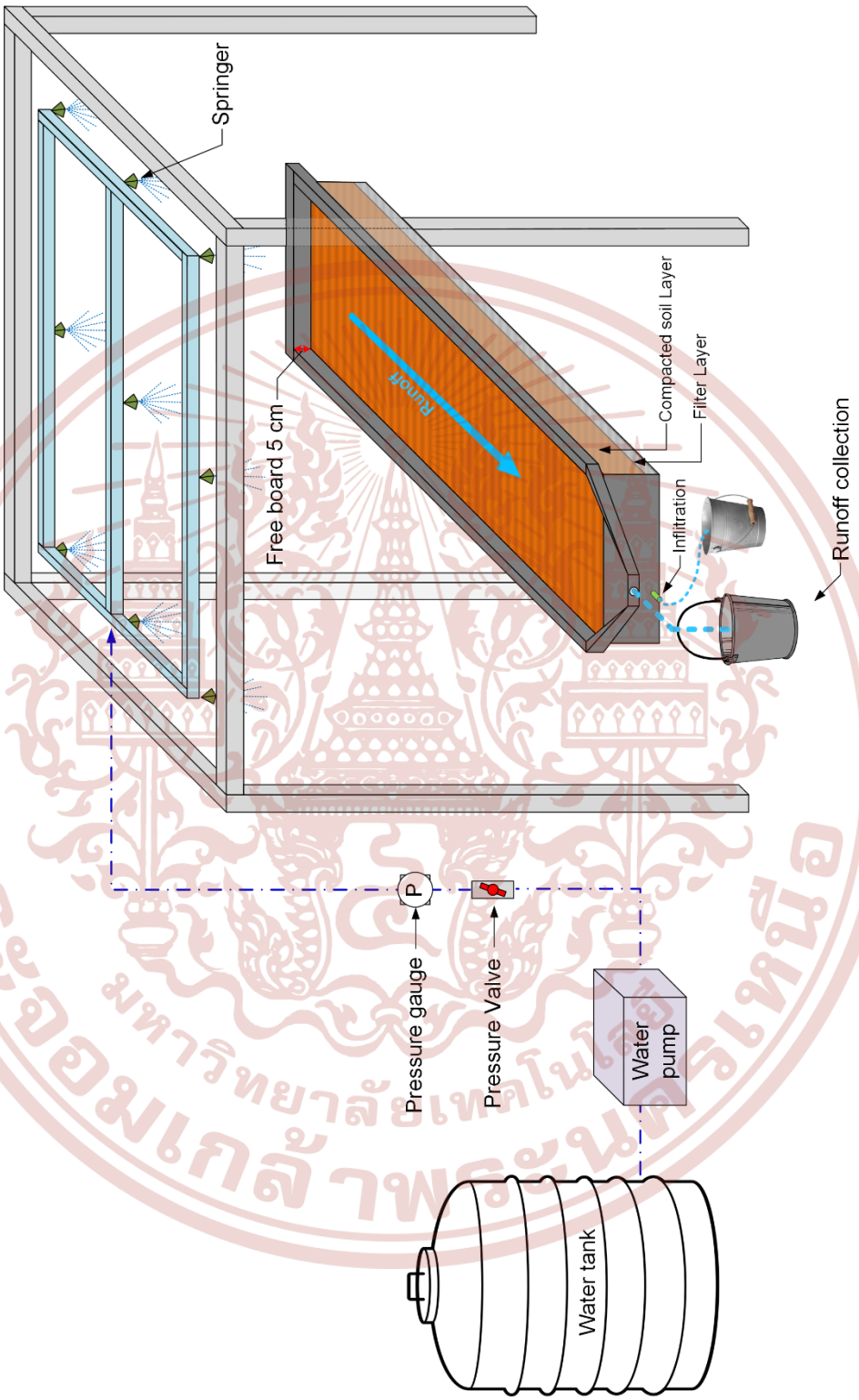


FIGURE 3-14 Artificial rainfall systems schematic

3.5.1 Rainfall Simulation on The Models

Raindrop sizes in Thailand generally vary between 2 and 5 millimetres. In Thailand, the monsoon season covers from June to late September. The distribution pattern of rainfall intensity in Thailand is similar to that measured in Illinois, USA. Therefore, the current researchers examined a model to match the temporal distribution of accumulated rainfall with the observed rainfall patterns in Thailand. as shown in Figure 3-12

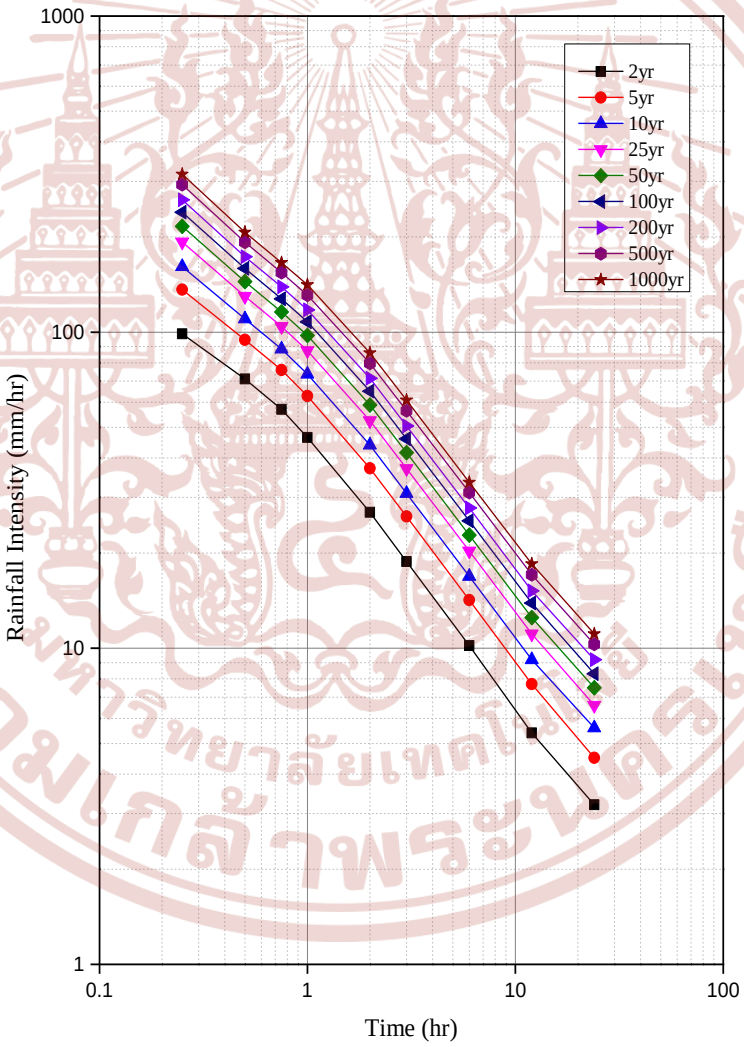


FIGURE 3-15 IDF curve for rainfall stations in the eastern region

This study uses the Intensity-Duration-Frequency (IDF) curve from rainfall stations in the eastern region with a recurrence interval of 25 years, corresponding to a value of 87.4, This is to correspond with the expected lifespan of road and pavement constructions. The graph illustrates the percentage of accumulated rainfall over time, the distribution of rainfall with a 50% probability within 1 hour, and the rainfall intensity for the 25-year recurrence interval in the eastern region. The rainfall intensity values are distributed every 10 minutes for the simulation, as shown in Figure 3-13

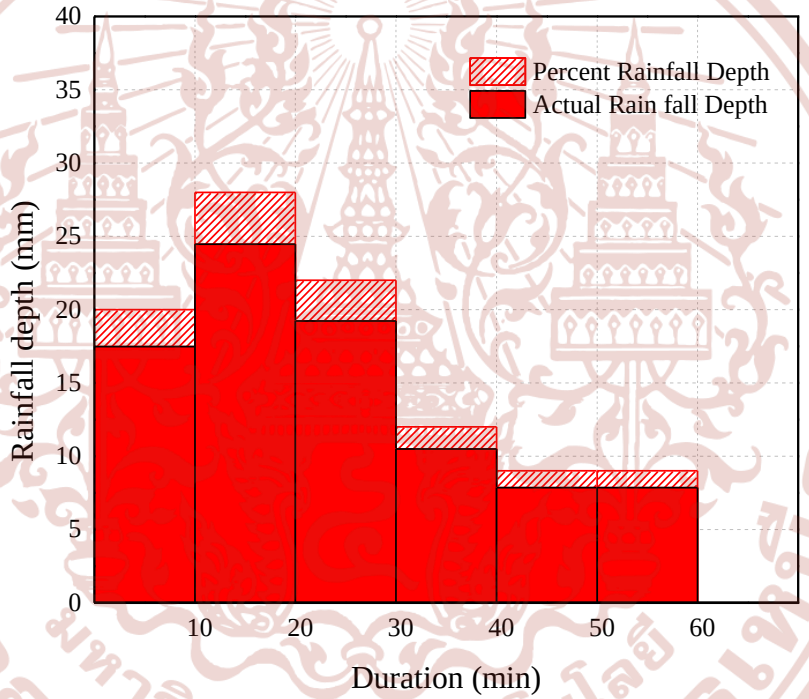


FIGURE 3-16 Rainfall intensity over 10-minute intervals within 1 hour

3.6 Soil Erosion Testing

The soil in each test flume had different dry densities of 1.30, 1.50, and 1.70 grams per cubic centimeter. All test flumes were set at a 45-degree slope, as shown in Figure 6. After the bare soil tests were completed, plants were cultivated using cuttings for one month. In this research, initial soil suction was not measured before testing due

to the limited sample thickness. Instead, initial water content before testing was considered a crucial factor.

(Figure 3-14a) Lay crushed stone as a water filter layer.

(Figure 3-14b) Place a steel mesh between the water filter layer and the soil.

(Figure 3-14c) Insert 6 mm smooth round steel bars to prevent soil slippage before testing.

(Figure 3-14d) Lay geotextile fabric to prevent soil from flowing into the filter layer.

(Figure 3-14e) Weigh the soil for filling the test flumes.

(Figure 3-14f) Compact the first layer to the specified density.

(Figure 3-15g) Compact the other layers up to the designated level.

(Figure 3-16h) Adjust the flume to a 45-degree slope.

พระจอมเกล้าพระนครเหนือ มหาวิทยาลัยเทคโนโลยี

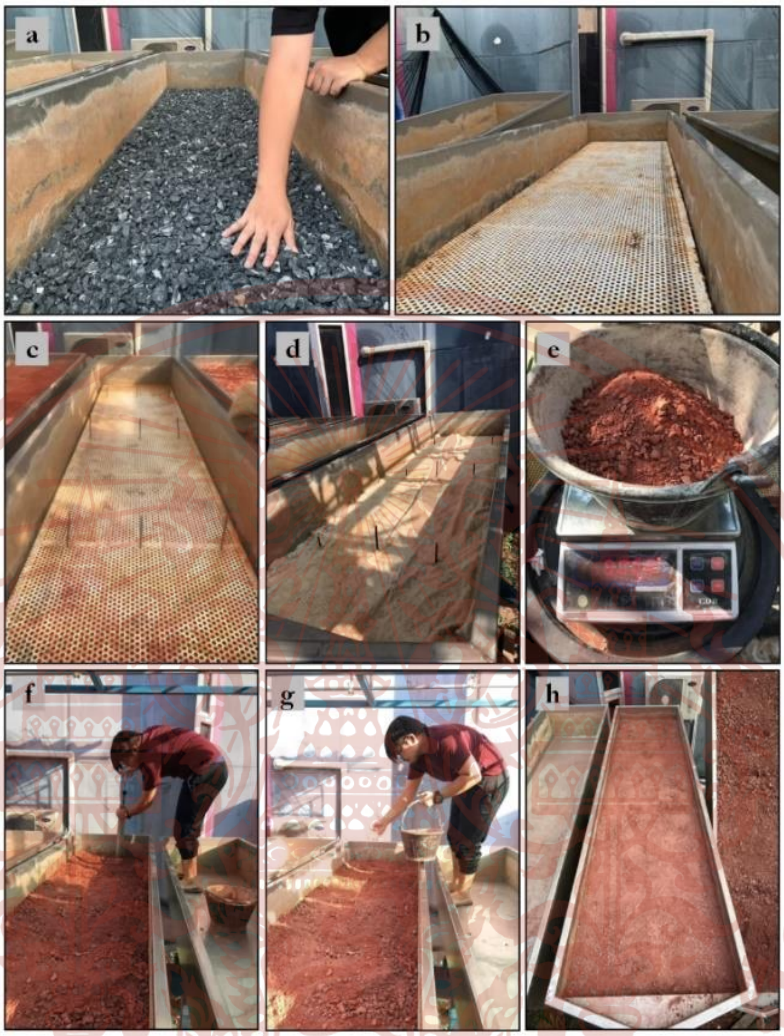


FIGURE 3- 17 Prepare Erosion Testing

3.6.1 Guidelines for Analyzing Erosion Behavior

Deng et al. (2019) studied soil erosion due to rainfall by analyzing variables to compare the runoff rate (Rr). Their study calculated the amount of runoff per second for the test flume area using Equation (3-1)

$$R_r = \frac{V}{BLT} \qquad \text{Equation (3-1)}$$

Where:

- **Rr** is the runoff rate in (ml/(m^2•sec))

- **V** is the volume of runoff (ml)
- **B** is the width of the test flume (meters)
- **L** is the length of the test flume (meters)
- **T** is the time taken to collect runoff (seconds)

The sediment rate (Sr) can be calculated as the mass of sediment per minute for the test flume area using Equation (3-2):

$$S_r = \frac{W}{BLT} \qquad \text{Equation (3-2)}$$

Where:

- **Sr** is the sediment rate in g/(m2•sec)
- **W** is the weight of the sediment (grams)

Sediment concentration S_c, in units of (g/l) is defined as the mass of sediment divided by the volume of water flow, according to Equation (3-3)

$$S_c = \frac{W}{V} \qquad \text{Equation (3-3)}$$

3.7 Analyzing Erosion Behavior Using Digital Elevation Model Technique

In geotechnical engineering, monitoring and assessing changes in field conditions can be challenging due to the extensive areas involved, which complicates damage evaluation and can lead to delays. The presence of vegetation further complicates measurements. Many engineering projects have adopted close-range photogrammetry techniques to create 3D models for simulating areas and tracking changes in soil slopes. The data obtained from close-range photogrammetry techniques have centimetre-level accuracy.

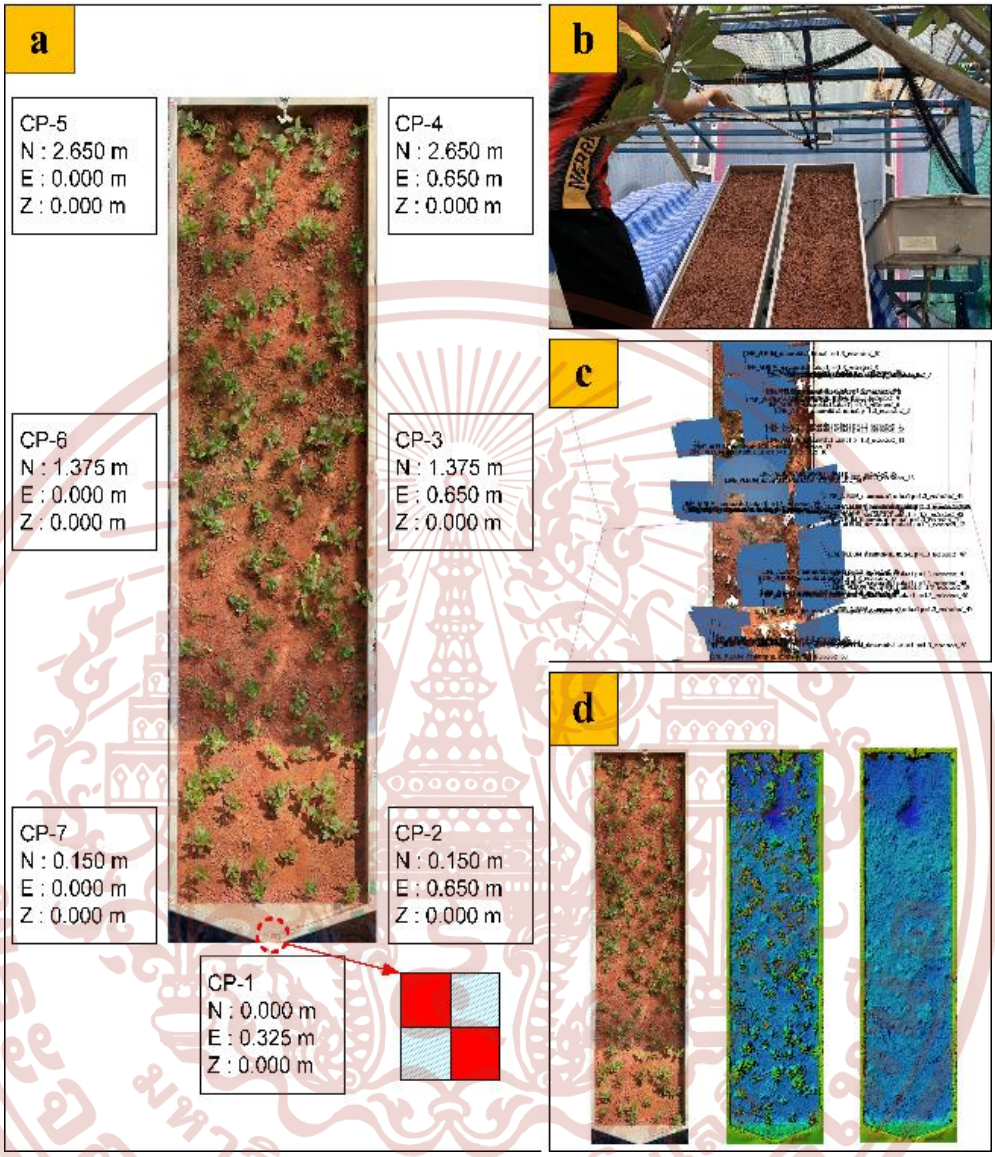


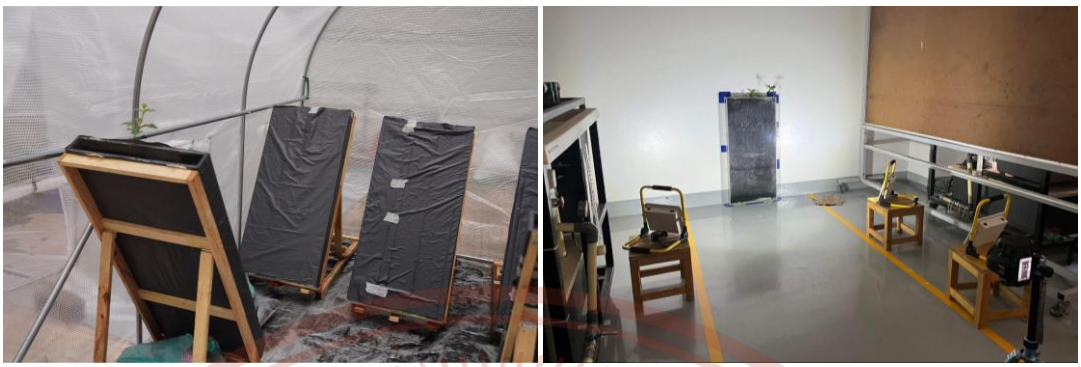
FIGURE 3-18 Determining Photogrammetric Surveying Positions and Processing

To establish the positions of photo control points, they must be visible, discernible in each photograph, and fixed to serve as reference points. First, measure and determine their coordinates as shown in Figure 14A. Then, take pictures covering all positions of the photo control points as illustrated in Figure 14B, and import the pictures into Agisoft Metashape software. The processing requires more than 30 images, as depicted in Figure 14C., using the initially defined coordinates to control scale and accuracy. Excess photos are removed once the software processes the images into a Point Cloud,

leaving only those from the test area. The analysis begins by removing vegetation cover using the “Specify Ground Point” function, then creating a Digital Elevation Model (DEM) as shown in Figure 14D. In experimental plots, accuracy is assessed by using the “Specify Ground Point” method, which involves detecting Point Clouds with RGB values of green within the specified range. Reconstruction of DEMs is generally less precise when vegetation cover is present compared to cases without vegetation. The calibration demonstrated that the accuracy of depth measurements achieved is below a 5% error margin. The collected results can be presented as a Digital Elevation Model showing erosion patterns.

3.8 Measurement of root architecture

Two types of growth media, namely, rice husk ash and lateritic soil, were prepared for *Wedelia trilobata* cultivation. Table 1 presents a comparative summary of the physical and chemical properties of two selected growth media used in the rhizobox experiments. The measured specific gravity values were 2.70 and 2.11 for lateritic soil and rice husk ash, respectively. The dry density was observed to be higher in lateritic soil (1.35 g/cm^3) compared to rice husk ash (0.95 g/cm^3). Grain size distributions characterized by D_{60}, D_{30}, and D_{10} revealed that both media are classified as poorly graded sand, with lateritic soil showing a finer gradation profile than rice husk ash. The pH values measured using a standard buffer solution were slightly acidic for both media, with lateritic soil at 6.9 and rice husk ash at 6.5. From a nutrient perspective, lateritic soil contained significantly higher concentrations of phosphorus (5.1 ppm) and potassium (4.1 ppm) compared to rice husk ash (2.5 ppm and 3.0 ppm, respectively). However, rice husk ash had a notably higher nitrogen content (2.6 ppm) than lateritic soil (0.9 ppm), suggesting differences in nutrient availability that could influence root development. These parameters provide a foundational understanding of the growth environments, which are critical to interpreting plant-soil interactions and root system development within the experimental setup.



(a) **(b)**

FIGURE 3-19 a.Rhizobox system and b.digital camera system

TABLE 3-5 Summary of the physical and chemical properties of the two selected growth media.

Parameter	Growth media		Reference
	Lateritic soil	Rice husk ash	
Specific gravity, G_s	2.70	2.11	Specific Gravity test (ASTM D854)
Dry density (g)	1.35	0.95	Standard compaction test (ASTM D698)
Void ratio, *e*	1.08	1.22	
Porosity, *n*	0.52	0.55	
D60 (mm)	1.70	1.50	Sieve analysis (ASTM D2487)
D30 (mm)	0.50	1.00	
D10 (mm)	0.15	0.30	
Texture	Poorly graded sand	Poorly graded sand	
pH	6.9	6.5	Standard buffer solution
Phosphorus, P (ppm)	5.1	2.5	
Potassium, K (ppm)	4.1	3.0	
Nitrogen, N (ppm)	0.9	2.6	

The root system of the WT. was observed weekly to determine the average growth rate. The root system image at the end of planting period (90 days) was analysed to obtain the root system architecture. To avoid the influence of sunlight, the root architecture of the vetiver species was imaged in a dark room using a digital camera

system. The camera system consists of a digital camera and two 50 W LED floodlights (Figure 3-19a). The captured root images then were analysed using Adobe Photoshop and ImageJ software. The flowchart of the root system architecture analysis is illustrated in the (Figure 3-20).

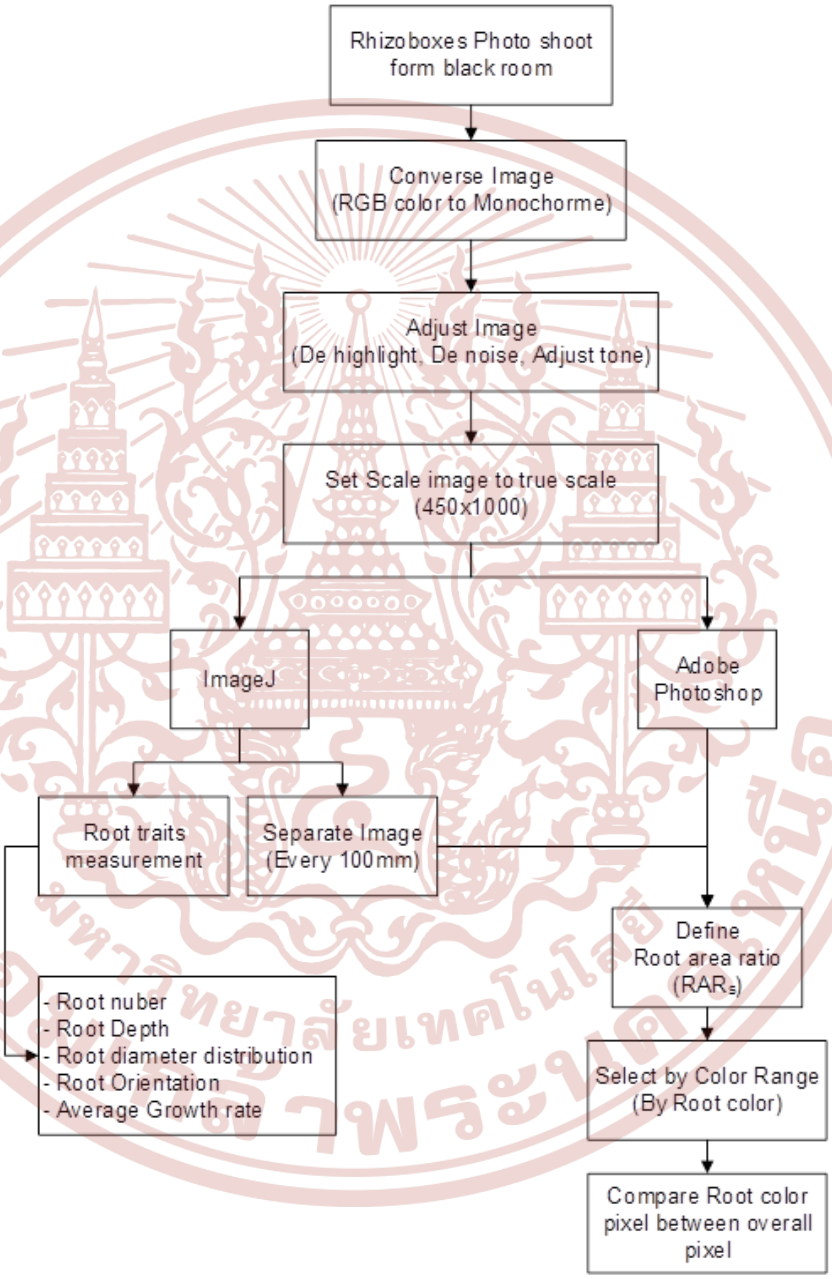


FIGURE 3-20 Processing and analysis of Wedelia trilobata rhizobox images

Firstly, import image to Adobe Photoshop for convert RGB to grey image and adjust root tone and reduce white noise from the original root images, which may influence the measurement results. then were set scale and divided into ten images (450 × 1000 mm) to measure the root architecture characteristics at 100 mm depth interval. Lastly, the following root architecture characteristics were measured: side RAR (i.e., RAR S, ratio between area of roots (i.e., white colour) and total area), orientation (i.e., W, angle between root direction and horizontal plane), and diameter (d) of individual root segments. In addition, the average growth rate (G, mm/day) of the root system of WT. was estimated as follows:

$$G = \frac{L}{n \times t} \qquad \text{Equation (3-4)}$$

where L is the total length of root system (mm), n is the number of roots and t is the growing period (day).

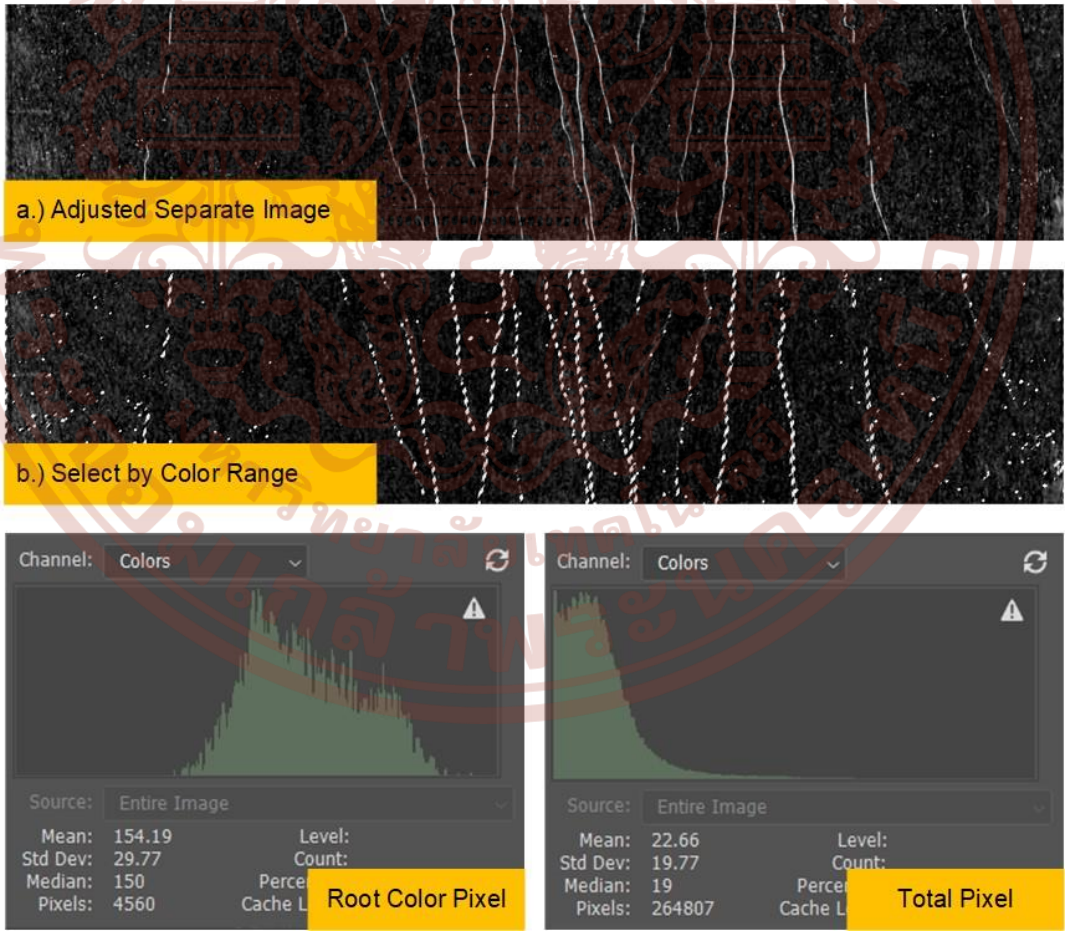


FIGURE 3-21 Image processing for defining Root Area Ratio (RARs)

In parallel, the “side” root area ratio (RAR_S) was calculated utilizing color range separation and pixel-based comparison methods to evaluate the ratio of root pixels to the total observed area, as depicted in Figure 3-17 displays the modified root images post-separation, whereas Figure 3-17 illustrates pixel selection according to color range to delineate root-specific regions. The histogram analysis below presents a comparative pixel count of root color pixels against total image pixels, allowing accurate RARs calculation. The analytical approach emphasized both morphological and spatial parameters, allowing a thorough evaluation of the RSA of *W. trilobata*, essential for assessing its soil-reinforcement capacity in varied substrates such as lateritic soil and rice husk ash.

3.9 Measurement root tensile strength and root cohesion (Cr) estimation

To quantify the tensile strength of *W. trilobata* roots, a total of 25 root segments, each approximately 20 cm in length, were carefully extracted from the rhizobox systems for each growth period . Selection criteria ensured that only roots with minimal physical damage with soaked condition, relatively straight alignment, and a nearly uniform diameter along their length were chosen to maintain measurement consistency. Particular attention was given to selecting sections located 2–3 cm from the root tip to avoid the influence of extreme tapering or immature tissue, which could bias the tensile strength results.

Each prepared root segment was mounted in a mini universal testing machine (model: L1-550× Digital Force Tester; Starrett), as shown in Figure 3-22 The roots were secured at both ends using pneumatic clamps, maintaining a consistent gauge length of 100 mm between clamps to standardize the test span across all specimens. To minimize slippage and root breakage at the clamping points, care was taken to align the root axis precisely with the loading direction.

The tensile load was applied at a constant crosshead displacement rate of 5 mm/min until the root failed. Throughout the test, tensile force and elongation data were continuously recorded using a data logger connected to a monitoring laptop, enabling real-time observation and accurate capture of breaking points. A high-

resolution camera system was also employed to capture the root deformation and failure process visually. This rigorous experimental setup ensured reliable measurement of the tensile strength, which is a critical mechanical parameter for evaluating the soil-reinforcing potential of *W. trilobata* roots under different soil conditions and growth durations.. The root tensile strength (T_r) is determined by the following equation.

$$T_r = \frac{F}{\pi\left(\frac{d^2}{4}\right)} \qquad \text{Equation (3-5)}$$

where F is the maximum force required to break a root, and d is the mean diameter of the root segment (i.e., the average diameter of three points along the root segment), the gradient of the initial linear part of a tensile stress-strain curve.

พระจอมเกล้าพระนครเหนือ มหาวิทยาลัยเทคโนโลยี

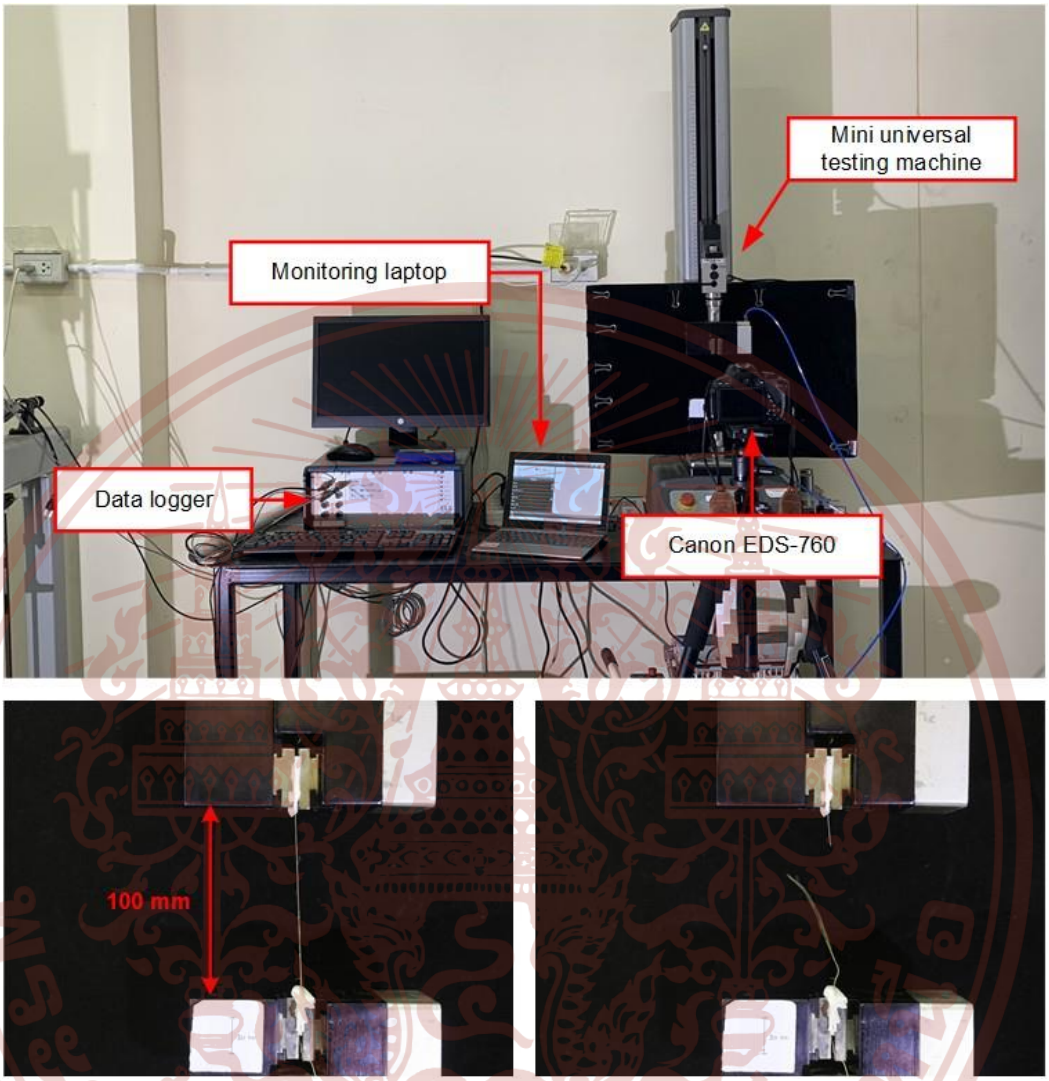


FIGURE 3-22 Experimental setup for root tensile strength test

From the mechanical perspective, the contribution of vegetation roots to soil shear strength is represented as root reinforcement or root cohesion (C_r). This concept highlights the importance of root systems in enhancing soil stability, particularly in geotechnical applications (Jian et al., 2024b; Lv et al., 2024b; Meijer et al., 2023). Incorporating root reinforcement into slope stability models can significantly improve predictions of soil behavior under various conditions, ultimately enhancing the safety and reliability of engineered slopes (Gentile et al., 2010). Quantifying root reinforcement, however, remains challenging due to soil opacity and environmental

variability. Thus, several theoretical root soil models have been proposed for root reinforcement. The first simple root reinforcement model, which assumes roots are perpendicular to the shear plane and break simultaneously, was proposed considering root (i.e., fiber) orientation (Wu et al., 1979). Based on this concept, Gray & Ohashi (1983) later provided an estimation method for root reinforcement.

$$C_r = T_r \times RAR \times \left[\sin\left(90 - \Psi\right) + \cos\left(90 - \Psi\right) \times \tan\phi \right] \quad \text{Equation (3-6)}$$

$$\Psi = \tan^{-1}\left[\frac{1}{\frac{x}{z} + \left(\tan^{-1} i\right)^{-1}} \right] \quad \text{Equation (3-7)}$$

where T_r is the root tensile strength, *RAR* is the root area ratio, φ is the soil friction angle, *i* is the root orientation, *x* is the shear displacement, and *z* is the shear zone thickness. The root area ratio, also known as *RAR*, is the ratio that is calculated by dividing the area of the root along the observed plane by the total area covered by the viewed plane.

To improve the accuracy of estimating root reinforcement, the root bundle model (RBM) was introduced by Cohen et al. (2011) as a more advanced approach compared to earlier simplified models. In as compared to Wu's model, which assumes the simultaneous failure of all roots aligned perpendicularly to the shear plane, the RBM enables progressive root breakage within a bundle and incorporates the actual distribution of root diameters as rather than depending solely on the root area ratio (RAR). This model enhances the accuracy of predictions by considering that root reinforcement is affected not only by the tensile strength of individual roots a metric often expressed in the literature but also by the spatial distribution and geometric configuration of the root system, including orientation, diameter, and density (Mickovski & van Beek, 2009; Phan et al., 2021b; Vergani et al., 2014).

Root system architecture (*RSA*), defined as the spatial configuration of roots within a soil matrix, is inherently sensitive to growth conditions and can vary

significantly both within and between species (Alastair Fitter, 2002). Despite its importance, characterizing RSA remains a significant challenge due to the opaque nature of soil. Traditional field-based methods, such as profile wall excavations and soil core sampling (Pagès & Pellerin, 1994), provide limited resolution and are labor-intensive. Several laboratory-based methods have been promoted to capture 2D root system architecture, which was grown in Petri plates, containers, and rhizoboxes with soil and non-soil media (French et al., 2009). To overcome these limitations, controlled laboratory techniques have been developed using 2D observation systems such as Petri dishes, transparent containers, and rhizoboxes filled with soil or artificial growth media (Devienne-Barret et al., 2006; Enyew et al., 2023; Maan et al., 2023; Mašková & Klimeš, 2020; Phan & Likitlersuang, 2024). These systems facilitate direct visualization and capture of root development. Root images obtained through flatbed scanners or digital camera setups are commonly analyzed using image processing tools such as ImageJ (Flavel et al., 2012), enabling quantification of *RSA traits* including *RAR*, root length, branching patterns, and orientation. These advances in imaging and analysis are critical for integrating realistic root behavior into geotechnical models that simulate vegetative soil reinforcement.

3.10 Root reinforcement estimation

In this study, root reinforcemnt of *W. trilobata* species at different growth periods was estimated using the combination of modified Wu' model (Gray & Ohashi, 1983) and RBMw (Schwarz et al., 2013). The RBMw estimates the tensile force of roots by assuming roots in the bundle behave as linear elastic elements, aligned in parallel and breaking at different displacements. In this model, the tensile force of single roots (F_s) is calculated using empirical relationships of tensile strength (T–d), secant modulus (E–d), and root length (L–d) with root diameter, together with the frequency distribution of diameters as follows:

$$F_S\left(d,\Delta x_r\right)=\frac{r\pi d^2E_0}{4L_0}\left(\frac{d}{d_0}\right)^{\beta-\gamma}\quad \Delta x;F_S\left(d,\Delta x_r\right)<F_{S,\max}(d)$$

Equation (3-8)

where d (mm) is root diameter, d_0 (mm) is the reference diameter and assumed to equal 1 mm, L_0 (mm), E_0 (MPa mm) are the scaling factors; γ , β (dimensionless) are the power law exponents; D_{xr} (mm) is the root displacement; and r (dimensionless) is the tortuous coefficient taken as 0.5 (Schwarz et al., 2013).

Tensile force of the root bundle ($F\left(\Delta x_r\right)$; N) is then estimated by summing the tensile force of each root multiplied by the survival function ($S(\Delta x_r^*)$), the tensile force can be obtained as follows:

$$F\left(\Delta x_r\right)=\sum_{i=1}^{n}\left[F_S\left(d_i,\Delta x_{r,i}\right)S(\Delta x_{r,i}^*)\right] \qquad \text{Equation (3-9)}$$

where n is the number of roots in the root bundle; and d_i (mm) is diameter of the i^{th} root in the bundle. The detailed in the Weibull survival function determination can be found in Schwarz et al. (2013). It is important to highlight that the $F\left(\Delta x_r\right)$ obtained from the RBMw is the tensile force of root, thus it is needed to convert the tensile force to shear reinforcement ($C_r(\Delta x)$) (i.e., in the direction parallel to the shear plane), which can be directly added to the Mohr-Coulomb criteria (Equations 3-10 and 3-11) for the stability analysis of vegetated slopes. Therefore, the orientation of roots in the bundle needs to be integrated in the process of conversion. The modified Wu's model, proposed by Gray & Ohashi (1983), was adopted to convert the pull-out resistance ($F_r(\Delta x)$) to shear reinforcement ($C_r(\Delta x)$) as follows:

$$C_r(\Delta x)=\frac{F_r(\Delta x)}{A_s}(\sin(90-\psi)+\cos(90-\psi)\tan\phi') \qquad \text{Equation (3-10)}$$

$$\psi=\tan^{-1}\left[\frac{1}{\frac{\Delta x}{Z}+\frac{1}{(\tan^{-1}\Omega)}}\right] \qquad \text{Equation (3-11)}$$

$$\Delta x_r = \sqrt{\left(\Delta x + \frac{Z}{\tan(180-\Omega)}\right)^2 + Z^2} - \frac{Z}{\sin(180-\Omega)} \qquad \text{Equation (3-12)}$$

where A_s (mm^2) is the cross-section area of the shear plane; Δx_r (mm) and Δx (mm) are the axial displacement of roots and shear displacement of soil, respectively; Z (mm) is the thickness of shear zone; Ω (º) is the initial average root orientation.

3.11 The slope stability analysis

This study integrates experimentally derived root cohesion values into a limit equilibrium analysis using SLOPE/W to evaluate the stabilizing effect of vegetation. Root zones were modeled with varying cohesion based on plant age, allowing assessment of their contribution under different slope geometries.

Figure 3-23 illustrates the conceptual model employed for the slope stability analysis conducted in this study using the GeoStudio software suite, specifically the SLOPE/W module. The slope profiles were modeled with varying inclinations of 30°, 35°, 40°, and 45°, and heights ranging from 2 to 6 meters to simulate practical embankment conditions encountered in infrastructure projects. The material parameters used in the analysis, including unit weight, internal friction angle, The analysis incorporated vegetative root reinforcement effects by defining two distinct zones within the slope body. The reinforced zones, highlighted in gray, represent the areas influenced by the root systems of *W. trilobata*, with different cohesion values assigned to the upper (C_{r1}) and lower (C_{r2}) root zones based on experimental data derived from 60 and 90 days of plant growth durations. The presence of these zones was intended to simulate the mechanical contribution of roots to shear resistance in shallow and intermediate slope depths.

The Janbu simplified method was selected as the limit equilibrium analysis approach, in combination with the grid and radius technique to identify the critical slip surface and compute the factor of safety (FoS). The effects of both slope geometry and vegetative reinforcement on FoS were systematically evaluated to understand how root

cohesion contributes to overall slope performance. Results of this parametric study, as indicated in Figure 3-19, demonstrate the beneficial influence of vegetative root systems on slope stability, especially under moderate to steep slope inclinations.

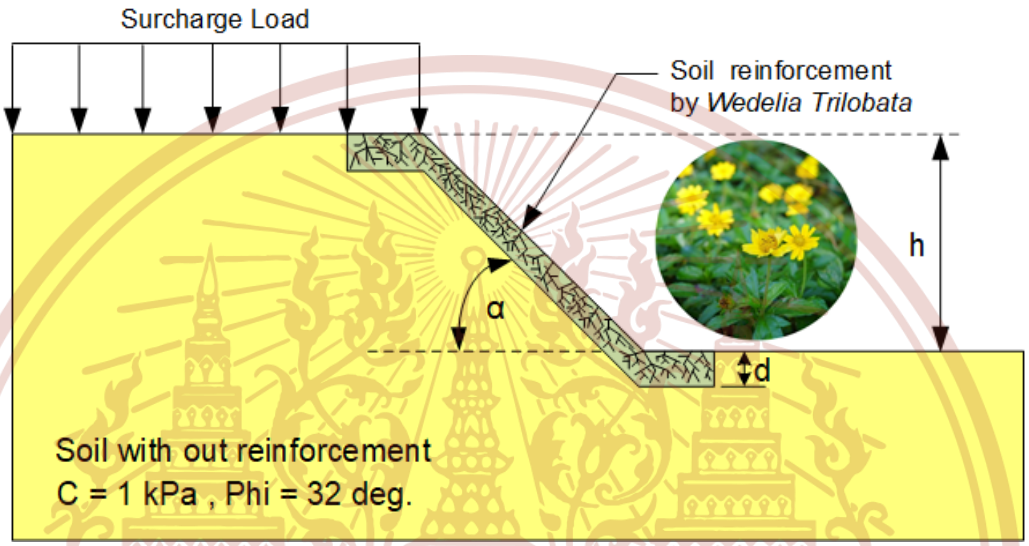


FIGURE 3- 23 slope stability analysis incorporating root cohesion (C_r) zones in reinforced and unreinforced soil layers

3.12 Data Analysis Using Heatmap

The Heatmap graph illustrates the relationships between various input variables and the output variable, Factor of Safety (FS). Each cell in the Heatmap represents the correlation coefficient between a pair of variables, with values ranging from –1 to 1.

- A value close to 1 indicates a strong positive correlation between two variables, meaning that as one variable increases, the other tends to increase as well.
- A value close to –1 indicates a strong negative correlation, meaning that as one variable increases, the other tends to decrease.
- A value close to 0 suggests no correlation or a very weak relationship between the variables.

This visualization technique allows for an intuitive understanding of how different parameters interact and influence the Factor of Safety in slope stability analysis.

Code Python for correlation heatmap (Example : for slope 1:1 height=2m)

```
import pandas as pd

import seaborn as sns

import matplotlib.pyplot as plt
# Load the data from the first sheet
file_path = "/content/Data FoS Correlation 1-1 only 2m.xlsx"
data = pd.ExcelFile(file_path)
df = data.parse('Sheet1')

# Select the columns for correlation analysis
selected_columns = ["Age", "Cr", "hr", "d", "RAR", "FS",]
df_selected = df[selected_columns]

# Calculate the correlation matrix
corr_matrix = df_selected.corr()

# Create the Heatmap
plt.figure(figsize=(8,6))

# Adjust font size for the numbers inside the heatmap
sns.heatmap(corr_matrix, annot=True, cmap="magma", vmin=-1,
vmax=1, center=0, cbar=True, annot_kws={"size": 15})

# Adjust font size for the x and y axis labels
plt.xticks(fontsize=15)
plt.yticks(fontsize=15)

# Set the title
plt.title("Slope 1:1 Height=2m", fontsize=18)

plt.show()
```

CHAPTER 4

ROOT BIOMECHANICAL RESULT

This chapter presents the evaluations of mechanical properties of root reinforcement and root architecture (i.e., ‘side’ root area ratio, root diameter and root orientation), also the tensile strength was measured via uniaxial tensile tests every month with two types of growth media. this study integrates experimentally derived root cohesion values into a limit equilibrium analysis using SLOPE/W to evaluate the stabilizing effect of vegetation. Root zones were modeled with varying cohesion based on plant age, allowing assessment of their contribution under different slope geometries

4.1 Result of root architecture

4.1.1 Root distribution

Figure 4-1 illustrates the root diameter distribution of Wedelia trilobata grown in two distinct substrates laterite soil and rice husk ash (RHA) at 2 and 3month intervals. The results indicate a notable contrast in root system characteristics between the two media. Specifically, plants cultivated in RHA produced a higher number of roots across nearly all depth intervals, reflecting a more prolific and finely branched root network. This observation aligns with the earlier discussion regarding the looser structure and lower density of RHA, which facilitates easier root penetration and expansion. Conversely, roots developed in laterite soil exhibited a greater proportion of thicker roots, particularly those exceeding 2.00 mm in diameter. Together, these patterns highlight the distinct adaptive strategies of W. trilobata in response to substrate properties: RHA promotes extensive root branching and elongation, whereas laterite supports the development of fewer but structurally more robust roots. Tables 4-1 to 4-4 present a detailed summary of the root architectural characteristics of W. trilobata grown in RHA and lateritic soil at two growth stages: 2 and 3 months. The key parameters include the number of roots, root area ratios (RARs), average root diameter, and orientation angles across 100 mm depth intervals from the surface to 1000 mm.

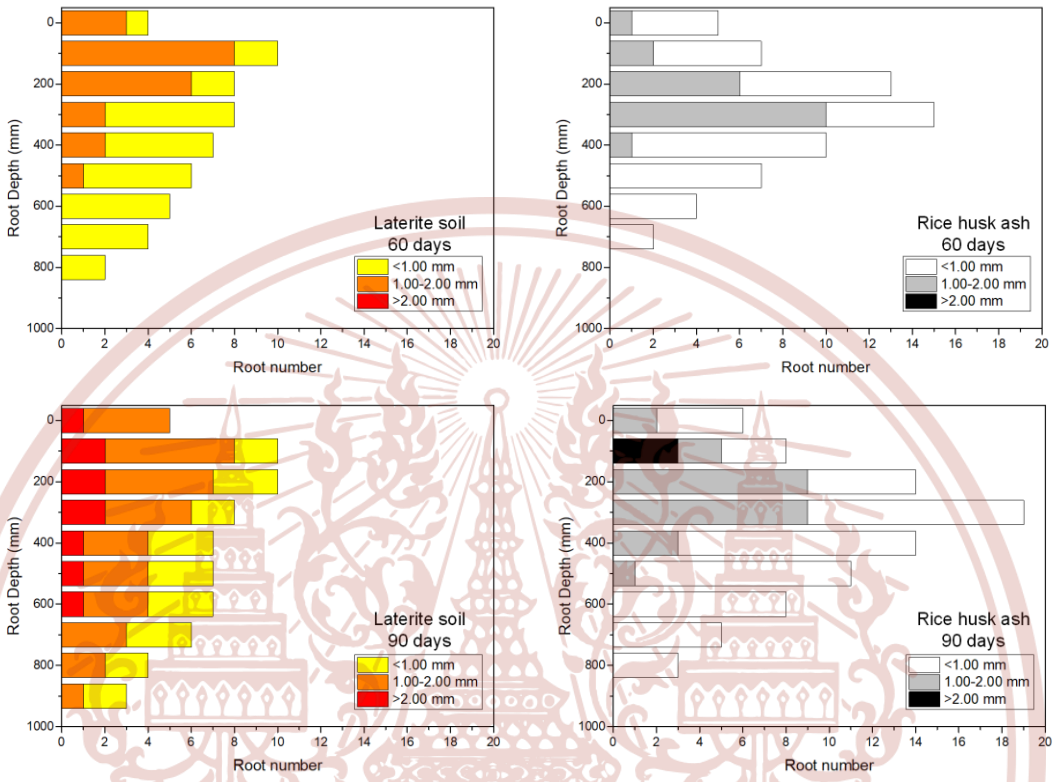


FIGURE 4-1 Root diameter distribution of W.trilobata

TABLE 4-1 Summary of root architecture parameters of WT. in rice husk ash 60 days

Species	*Wedelia trilobata*			
Depth (mm)	Number of roots (*n*)	RARs (%)	Diameter (d, mm)	Orientation (Ω, o)
0-100	5	0.737	0.813±0.764	77.122±18.453
100-200	7	2.080	0.903±0.628	76.453±21.386
200-300	13	2.650	0.995±1.178	75.053±19.835
300-400	15	2.566	1.049±0.891	77.620±24.453
400-500	10	2.734	0.830±0.564	82.988±22.239
500-600	7	1.646	0.766±0.662	81.770±27.551
600-700	4	0.588	0.632±0.423	81.163±16.793
700-800	2	0.432	0.516±0.102	80.657±7.599
800-900	-	-	-	-
900-1000	-	-	-	-
Total	63	1.679		

TABLE 4-2 Summary of root architecture parameters of WT. in rice husk ash 90 days

Species	*Wedelia trilobata*			
Depth (mm)	Number of roots (*n*)	RARs (%)	Diameter (d, mm)	Orientation (Ω, o)
0-100	6	1.037	0.942±0.942	64.886±15.340
100-200	8	2.899	1.739±0.803	73.559±9.441
200-300	14	4.004	1.077±1.440	81.487±16.028
300-400	19	4.983	1.033±1.375	79.828±23.784
400-500	14	3.954	0.908±1.063	81.206±19.960
500-600	11	2.780	0.853±1.171	84.337±14.582
600-700	8	1.202	0.673±0.766	84.630±13.776
700-800	5	0.934	0.664±0.774	86.333±6.057
800-900	3	0.724	0.676±0.529	86.635±3.723
900-1000	-	-	-	-
Total	88	2.502		

TABLE 4-3 Summary of root architecture parameters of WT. in Laterite soil 60 days

Species	*Wedelia trilobata*			
Depth (mm)	Number of roots (*n*)	RARs (%)	Diameter (d, mm)	Orientation (Ω, o)
0-100	4	2.013	1.205±0.981	74.069±10.931
100-200	10	2.284	1.228±1.502	77.037±22.188
200-300	8	2.238	1.105±1.582	81.083±17.696
300-400	8	1.576	0.894±1.186	80.318±16.918
400-500	7	0.983	0.895±1.070	78.042±17.507
500-600	6	1.124	0.931±1.062	83.051±14.504
600-700	5	1.001	0.741±0.923	85.874±6.030
700-800	4	0.902	0.713±0.764	82.106±5.149
800-900	-	-	-	-
900-1000	-	-	-	-
Total	52	1.515		

TABLE 4-4 Summary of root architecture parameters of WT. in Laterite soil 90 days

Species	*Wedelia trilobata*			
Depth (mm)	Number of roots (*n*)	RARs (%)	Diameter (d, mm)	Orientation (Ω, o)
0-100	5	2.686	1.229±1.071	78.777±14.563
100-200	11	3.126	1.267±1.309	76.918±23.362
200-300	10	2.628	1.105±1.122	75.049±29.412
300-400	8	2.149	1.103±0.921	80.854±26.403
400-500	7	1.602	0.981±0.912	81.433±17.882
500-600	8	1.580	0.952±0.978	81.086±19.088
600-700	6	1.613	0.860±0.581	83.754±13.362
700-800	5	0.902	0.765±0.655	79.240±15.578
800-900	5	0.698	0.607±0.485	78.310±5.560
900-1000	-	-	-	-
Total	65	1.887		

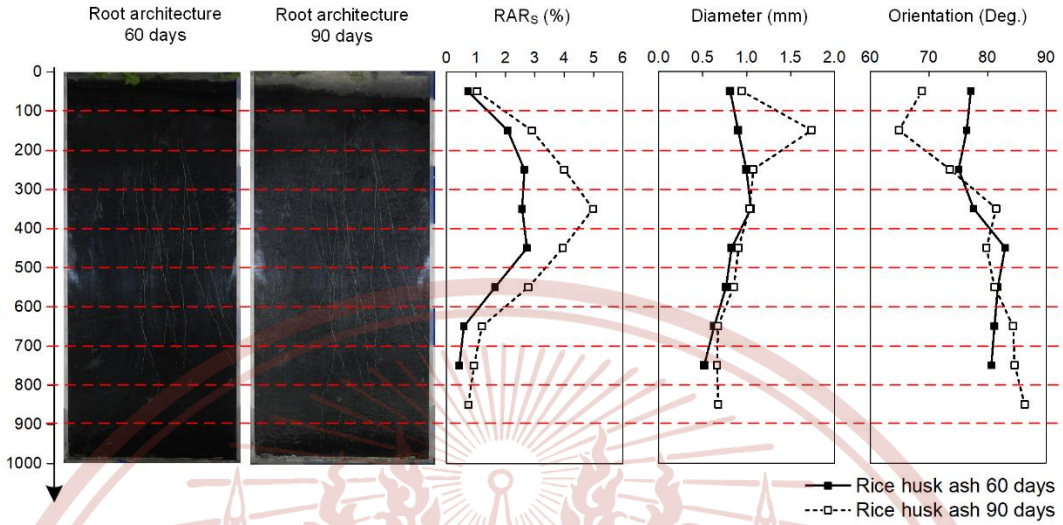


FIGURE 4-2 Root architecture characteristics of W.trilobata grown in rice husk ash

Figure 4-2 presents the variation of root architecture characteristics of W. trilobata growing in rice husk ash. The RARs profiles reveal pronounced peaks between 300-600 mm depth, indicating a concentration of root biomass in the middle segment of the root system. This trend persists over time, with the three-month roots displaying higher RARs values, suggesting denser root development as growth progresses. In comparison to the findings of Phan and Likitlersuang (2024) on C. nemoralis and C. zizaniodes, where RARs increased with depth or remained nearly constant, respectively, the current results demonstrate a distinct pattern unique to W. trilobata. This difference underscores the contrasting root system behaviors between W. trilobata, typically employed as a ground cover species, and vetiver species, which are widely used in slope stabilization applications. The average root diameter remains approximately 1 mm across the profile, with only a slight increase noted over time, reflecting gradual radial growth. Root orientation exhibits a declining trend with depth, suggesting a shift from more oblique angles near the surface to nearly vertical alignments at greater depths. Notably, root orientation profiles remain nearly identical between the two and three month observations, indicating that the overall directional pattern of root development stabilizes early during establishment.

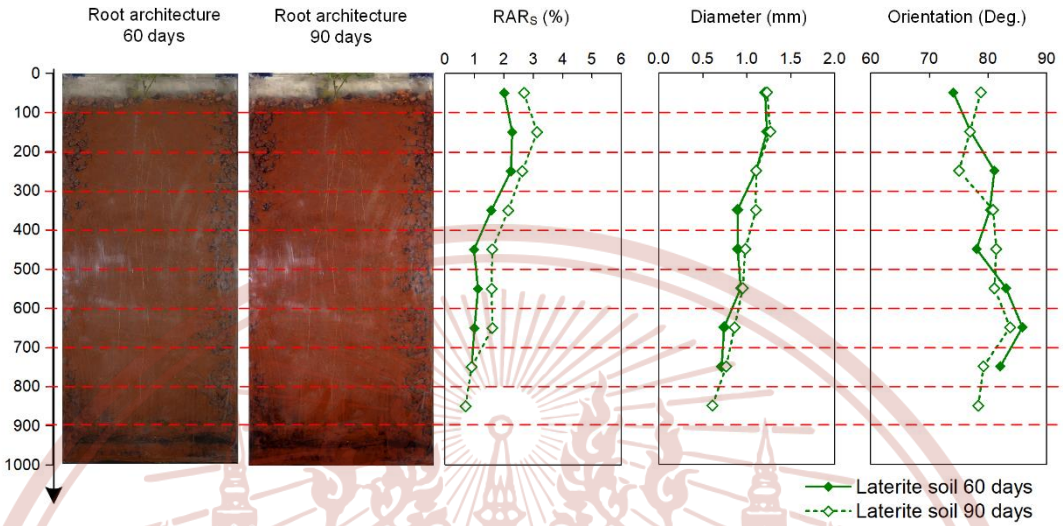


FIGURE 4-3 Root architecture characteristics of W.trilobata grown in grown in laterite soil

Figure 4-3 presents the root architecture characteristics of W. trilobata grown in laterite soil at 2 and 3 months. Across all root traits root area ratio (RARs), average root diameter, and root orientation—a consistent declining trend with depth is observed, suggesting vertical differentiation in resource allocation and root function . The overall values for both time points are nearly identical, indicating limited morphological changes between the 2 and 3 month growth stages under lateritic conditions. However, a slight increase in root depth at 3 months is evident, reflecting progressive elongation over time. When compared to growth in rice husk ash (RHA), roots developed in laterite exhibit lower RARs, smaller orientation angles, and slightly reduced elongation, likely due to the denser, more compact structure of lateritic soil, which constrains root penetration and expansion. In contrast, the average root diameter in laterite is larger than that in RHA. This may be attributed to the relatively higher nutrient content particularly nitrogen (N), phosphorus (P), and potassium (K) available in laterite, as indicated by the SEM-EDX analysis (Figure 3-8), which likely promotes radial rather than longitudinal root growth. These observations underscore the contrasting influence of soil texture and nutrient availability on root system architecture and suggest that

substrate conditions significantly affect the growth strategy of W. trilobata, a species often utilized for ground cover and soil stabilization.

Figure 4-4 illustrates the box plots of the distribution of root system parameters. The average root area ratio (RAR_s) increased from 1.79 to 2.50 in RHA and from 1.52 to 1.89 in lateritic soil, indicating deeper, denser root networks. Based on the Percentile 50% values, as depicted in Figure 4-4a, the RAR_s increased from 1.87 to 2.78 in the RHA and from 1.35 to 1.62 in lateritic soil during 60 and 90 days, respectively.

Figure 4-4b, the average root diameter of *W. trilobata* grown in lateritic soil was larger than that in RHA. The mean root diameter showed minimal variation over time and between media. In RHA, it slightly increased from 0.912 mm at 60 days to 0.965 mm at 90 days, while in lateritic soil, it rose from 1.036 mm to 1.042 mm.

Figure 4-4c, the root orientation angles of *W. trilobata* were similar between the two growth media, with mean values between roughly 77.8° and 78.9°, indicating mostly near-vertical root growth. The 50th and 75th percentile values for both RHA and lateritic soil were nearly comparable. Whereas the 25th percentile in lateritic soil was significantly higher (75.3° at 60 days and 74.5° at 90 days) than in RHA (71.6° and 70.7°), implying a narrower spread of data and a more concentrated orientation distribution.

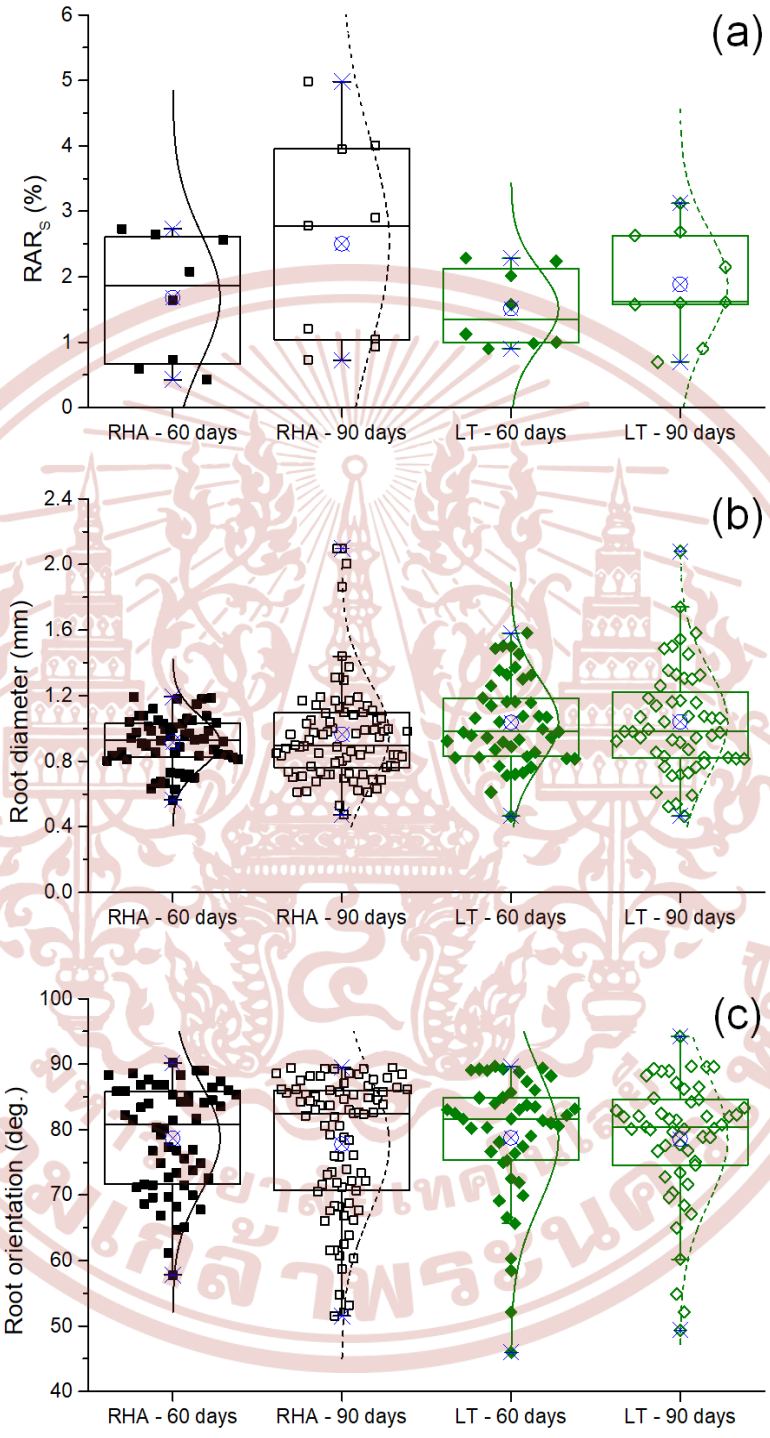


FIGURE 4-4 Boxplots illustrating the distribution of root system parameters of W. trilobata grown in rice husk ash (RHA) and lateritic (LT) soils at 60 and 90 days of growth: (a) root area ratio (RAR_s), (b) root diameter, and (c) root orientation.

4.2 Root engineering properties

4.2.1 Root tensile strength test

Figure 4-5 illustrates the relationship between root diameter and tensile strength for W. trilobata, comparing results across different soil media and planting durations. The observed tensile strength decreases as root diameter increases, following a trend similar to that reported for vetiver roots used in soil reinforcement. By comparing the data with a previous study conducted on different species, the data show that W. trilobata generally exhibits lower tensile strength values than the benchmark vetiver species (C. nemoralis and C. zizanioides) reported by Likitlersuang et al. (2022). This indicates that, although W. trilobata roots are finer and possess lower tensile resistance than vetiver, they can still contribute to soil binding due to their high root density and branching.

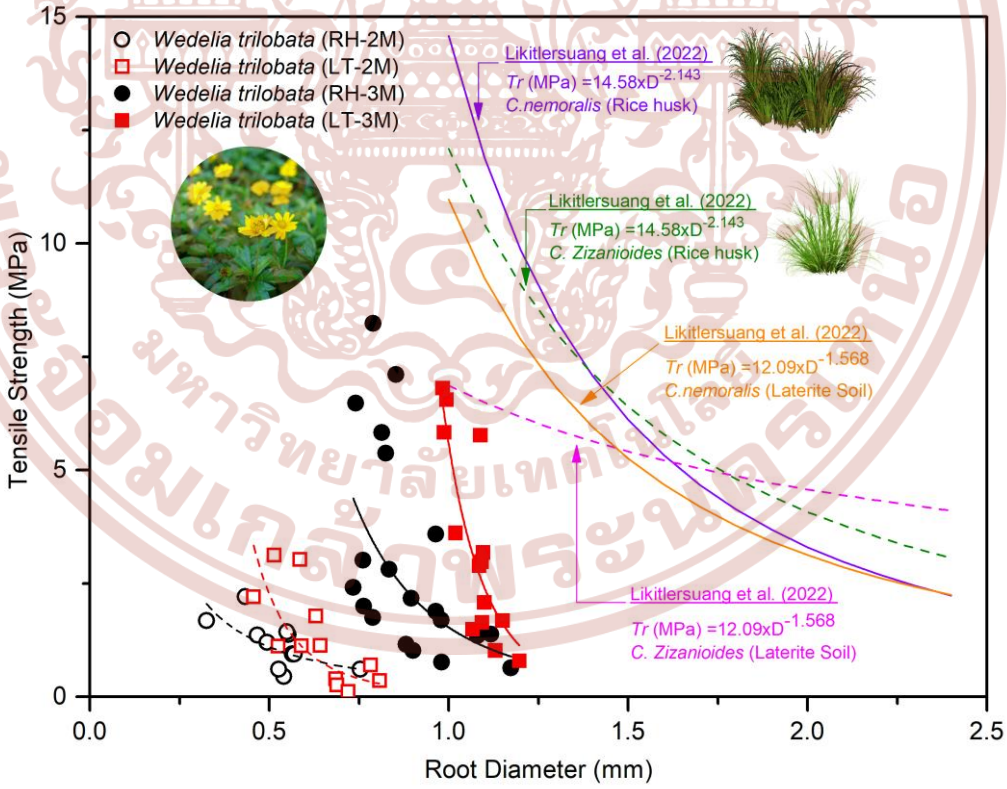


FIGURE 4-5 Correlation between tensile strength (Tr) and root diameter (d) of Wedelia trilobata

Figure 4-6 presents the relationship between root diameter and Young's modulus for W. trilobata, evaluated under different soil conditions and growth durations. Similar to the tensile strength trend, the Young's modulus tends to decrease with increasing root diameter, indicating that finer roots contribute more to stiffness at small diameters. Although W. trilobata roots have a lower modulus overall, their dense root mat and prolific branching could compensate for their lower mechanical stiffness, making them viable for applications targeting surface soil stabilization and erosion control. The comparative results suggest that W. trilobata may be suitable for applications requiring shallow root reinforcement, low to moderate slope height, and erosion control, while vetiver species remain preferable for deeper soil stabilization due to their stronger and thicker roots. Overall, the tensile and modulus properties of W. trilobata support its potential as a cost-effective alternative for eco-engineering practices.

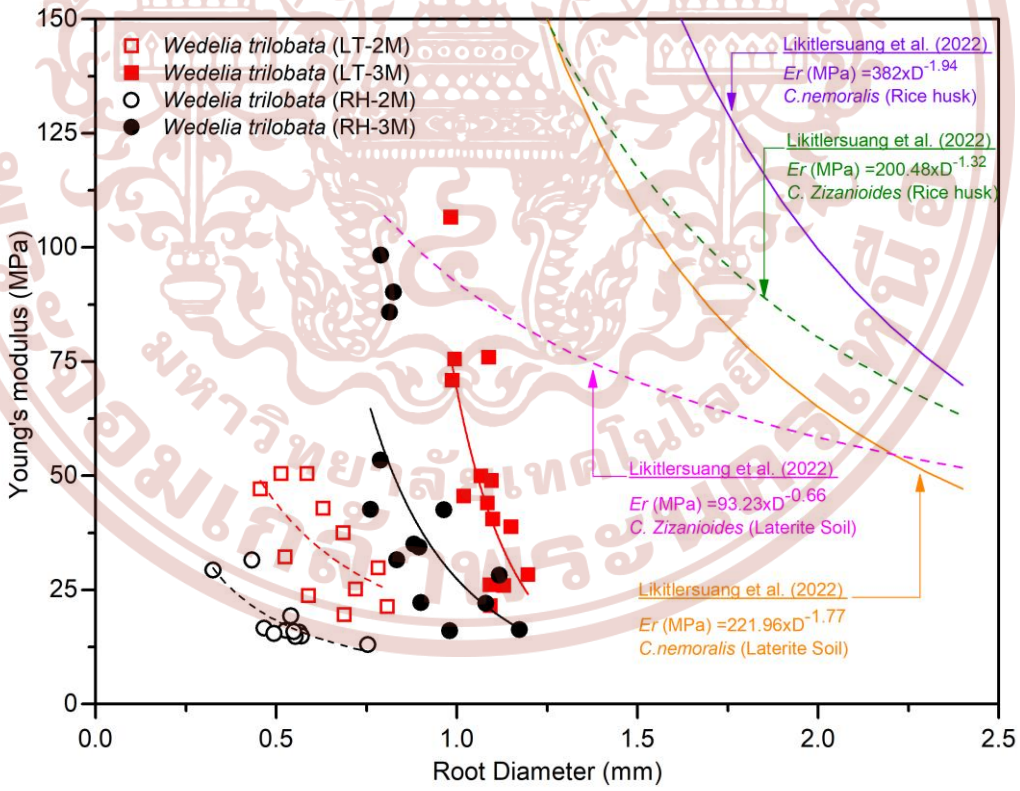


FIGURE 4-6 Correlation between Young's modulus and root diameter (d) of Wedelia trilobata

Figure 4-7 illustrates the relationship between tensile strength and Young's modulus for *W. trilobata* roots grown in different soil conditions and for different growth periods. The results reveal a positive correlation between tensile strength and stiffness, consistent with the mechanical behavior observed in vetiver species reported by Likitlersuang et al. (2022). Although *W. trilobata* shows generally lower tensile strength and Young's modulus values compared to vetiver roots, the linear relationship indicates predictable mechanical performance, which is critical for modeling root reinforcement in slope stability analyses.

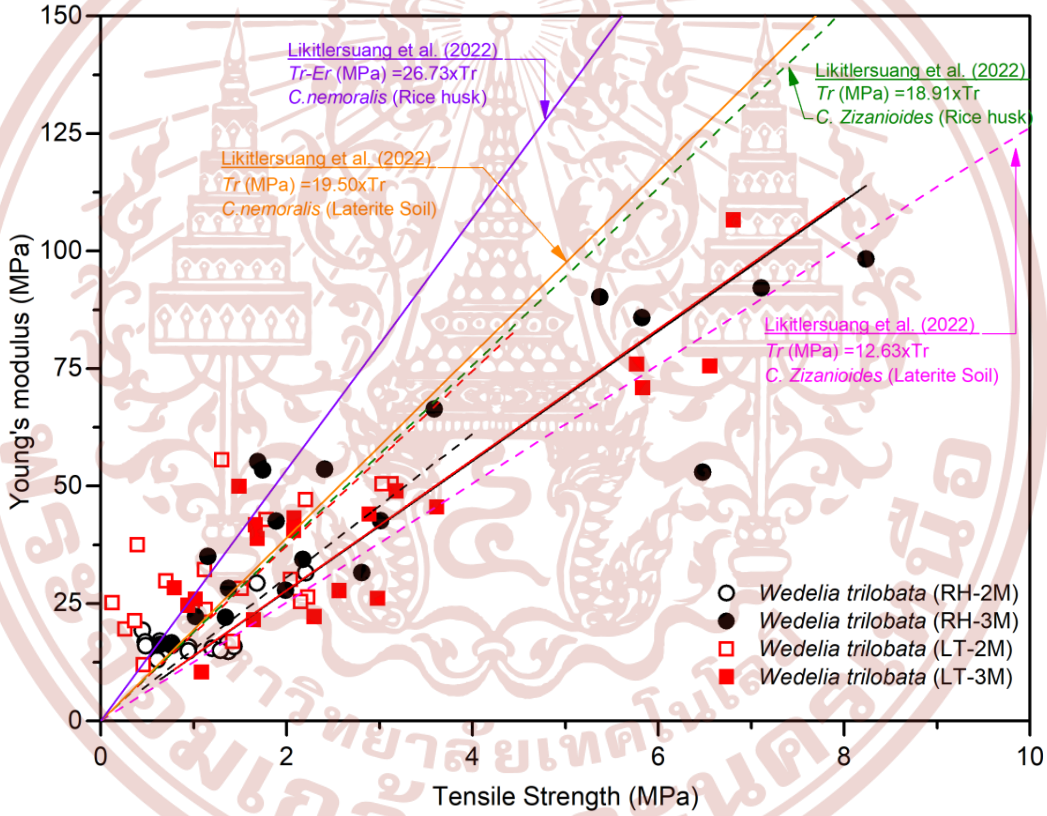


FIGURE 4-7 Relation Tensile strength and Young's modulus of Wedelia trilobata

The estimated root reinforcement and corresponding shear displacement of *W. trilobata* under different growth media and growth durations are presented in Table 4-5 The results clearly demonstrate the strong influence of growth medium on reinforcement performance. At both 60 and 90 days, *W. trilobata* cultivated in RHA

exhibited higher root reinforcement (0.80 and 3.92 kPa, respectively) compared with those grown in lateritic soil (0.12 and 3.56 kPa, respectively). Although the tensile strength of roots in RHA was generally lower than in lateritic soil, the greater reinforcement in RHA is attributed to the higher root density and larger mean root diameter, which collectively enhanced anchorage capacity and load transfer within the root–soil system. A similar influence of growth medium was observed for shear displacement. Roots grown in RHA showed larger displacement (1.679 and 2.502 mm at 60 and 90 days, respectively) compared with those in lateritic soil (1.515 and 1.887 mm, respectively). This difference may be explained by the higher Young's modulus of *W. trilobata* roots cultivated in RHA, which reflects greater elasticity and deformation capacity under applied loads (Table 4-5).

Root reinforcement increased markedly with plant age in both growth media. After 90 days, the root cohesion in RHA reached 3.92 kPa, nearly five times higher than at 60 days, owing to both a substantial increase in root number (from 52 to 82) and improved mechanical strength (from 1.382 to 3.032 Mpa). In lateritic soil, although the number of roots remained constant (44), the increase in tensile strength (from 1.776 to 3.189 MPa) resulted in the enhancement of root reinforcement from 0.12 kPa to 3.56 kPa. These results indicate that reinforcement in RHA is governed mainly by root proliferation and thickening, whereas in lateritic soil, it is driven predominantly by the strengthening of existing roots.

To our best knowledge, this study is the first to investigate the reinforcement of *W. Trilobata* root. The root reinforcement of *W. Trilobata* in this study is within the range of several well-established bioengineering species. For example, Woody shrubs such as Salix and Alnus species often contribute 2-17 kPa for Salix (Kamath et al., 2025), 4-12 kPa for *A. glutinosa* (Zydroń and Skórski, 2018), depending on root density and diameter distribution, while riparian trees (*E. camaldulensis*) have been reported to provide cohesion in the range of 15-19 kPa (Abernethy & Rutherfurd, 2001). In addition, the vetiver species, which has been widely applied for soilbioengineering, typpically provides root reinforcement values of 7 kPa (Eab et al., 2015), and combination of vetiver and ruzi grasses results in 11-19 kPa during 2-6 months

(Teerawattanasuk et al., 2014). The observed reinforcement values of *W. trilobata* (up to 4 kPa at 90 days) therefore demonstrate comparable or superior performance, highlighting its potential as an effective species for shallow slope stabilization in tropical environments where rapid root proliferation is advantageous.

TABLE 4- 5 Summary of root-induced cohesion values produced by W. trilobata

Growth Period (days)	Growth Media	Avg. T_r (MPa)	Root depth (mm)	RAR_S (%)	C_r Wu model (kPa)	C_r Root bundle model (kPa)
60	Rice husk ash	1.382	743.24	12.97	16.01	0.80
90	Rice husk ash	3.032	850.36	21.20	57.42	3.92
60	Laterite soil	1.776	825.93	10.11	16.02	0.12
90	Laterite soil	3.189	925.18	11.04	31.44	3.56

4.3 Application for slope stability analysis

In the current work, the GeoStudio software, specifically SLOPE/W, based on the limit equilibrium method for analyzing slope stability was used. The slope section with a 1:1, 1:1.5, 1:2 ration and 10.00 meters road width, varies height of slope 2.00 to 6.00 was modeled. And applied surcharge load to road equal 10.00 kN/m^2, The material properties are detailed in Table 4-5. To determine the safety factor, the Janbu method was utilized to define a slip surface using the grid and radius method. The slope stability analysis result was shown in Figure 4-8

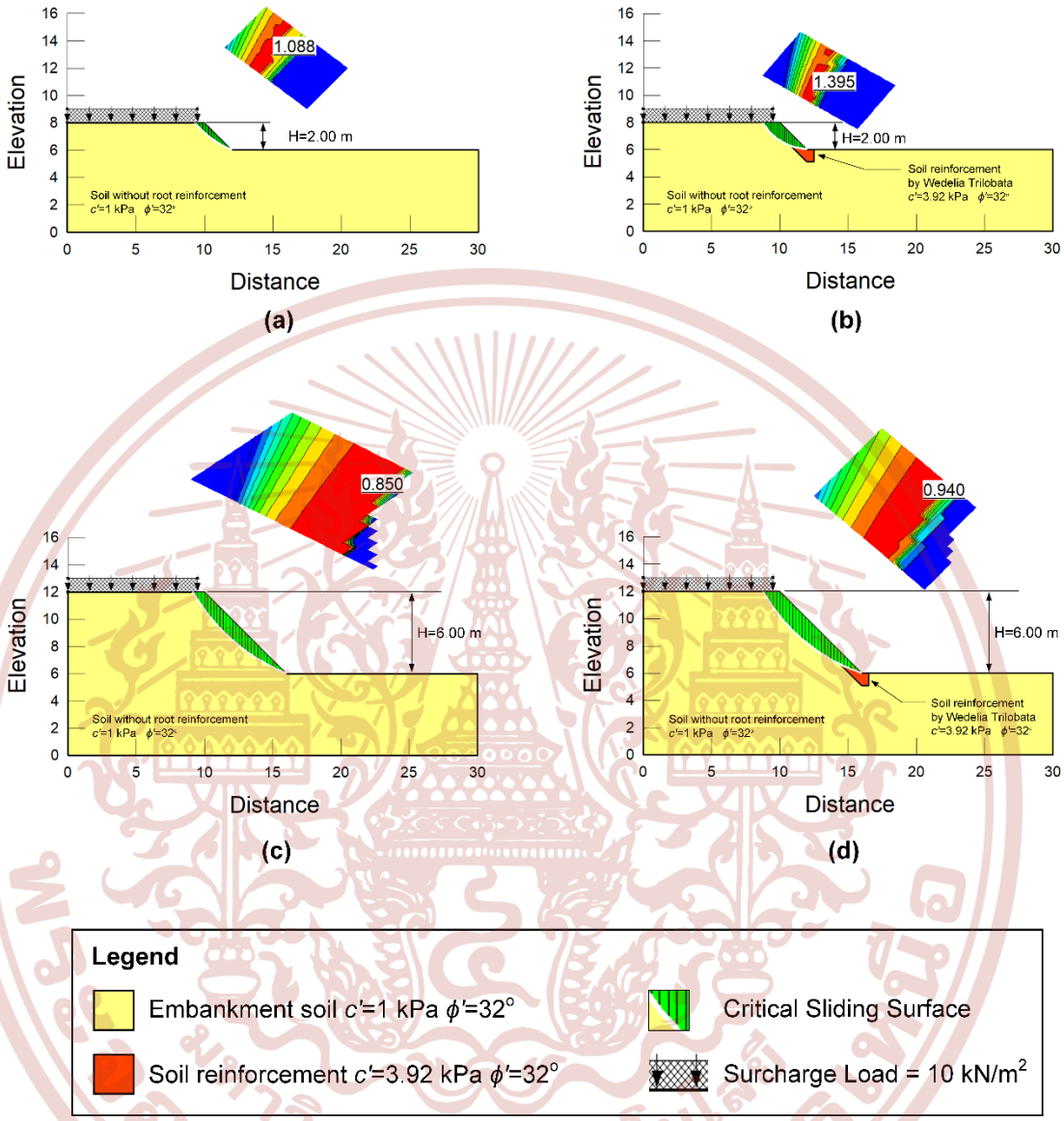


FIGURE 4- 8 Slope analysis results soil without roots and soil with roots

An unreinforced 2-meter slope had a Factor of Safety (FS) of 1.088, indicating marginal stability with a shallow failure surface. Reinforcing the slope with Wedelia trilobata increased the FS to 1.395, a 28.22% improvement. The roots acted as a reinforcement layer, increasing soil shear strength and pushing the critical failure surface to a deeper, less critical path. This highlights root reinforcement's effectiveness in stabilizing low-height slopes.

When the analysis was extended to a 6-meter slope, the unreinforced condition was unstable, with an FS of 0.850. While root reinforcement did improve the FS to 0.940, it remained below 1.0. This is because the driving forces from the taller embankment were too substantial for the shallow root system to fully counteract. The results show that the effectiveness of root reinforcement is inversely proportional to slope height, making it a complementary measure rather than a standalone solution for taller slopes.

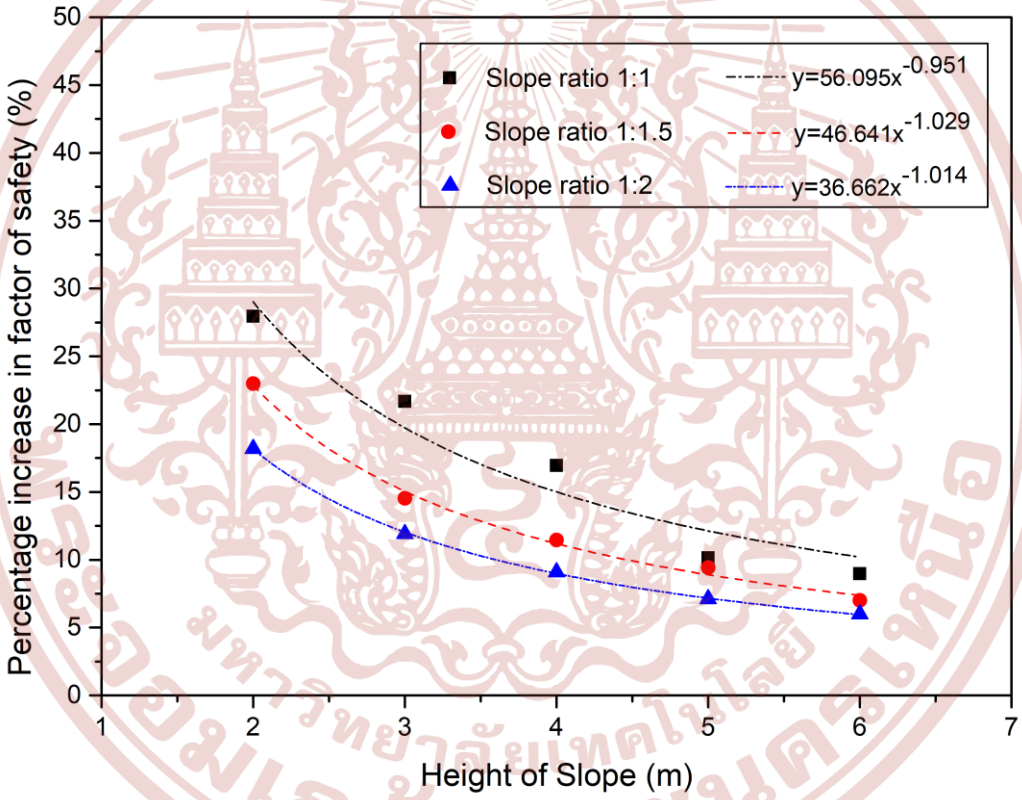


FIGURE 4-9 Increase in percentage of safety factor

Figure4-10 presents the correlation matrices among root parameters, slope geometry, and factor of safety (FoS) for slopes reinforced with W. trilobata. Previous investigation on sensitivity analysis of vetiver-reinforced slopes has indicated that for steep slopes, particularly at a 45° inclination (slope ratio 1:1), RAR and C_r are the most important

variables influencing FoS (Maadi & Noorzad, 2024). Comparing to this study, the results show that the slopes with a 1:1 ratio, the correlation results indicate that C_r and root age have the most significant impact on FoS, as depicted in Figures 4-10(a) and 4-10(b). This result is consistent with can be attributed to the considerable increase in C_r between 60 and 90 days of growth, which directly enhances shear resistance within the root zone. Consequently, the effect of root age is more pronounced, reflecting the gradual increase in enhancement of tensile strength and cohesion over time. When the slope becomes flatter (slope ratios of 1:1.5 and 1:2), as shown in Figures 4-10(c)–(f), the relative influence of root depth (h_r) and root diameter (d) on FoS decreases. C_r becomes the primary variable affecting stability in flatter geometries. This is particularly evident at higher slope heights, where the failure often occurs deeper than the root zone and is therefore predominantly governed by the shear resistance provided by C_r. Consequently, although root depth and diameter contribute to reinforcement, their influence becomes relatively less significant on flatter slopes.

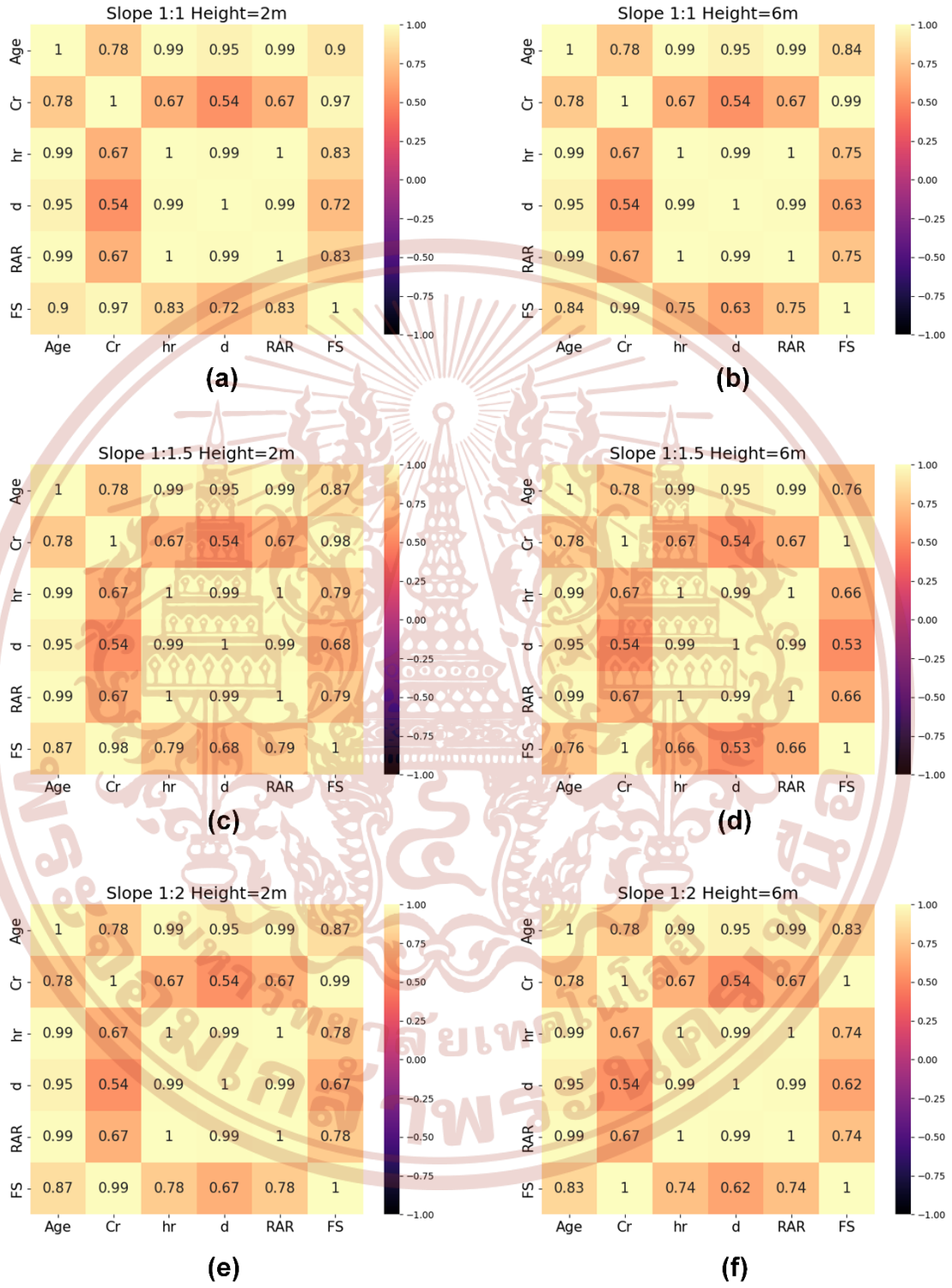


FIGURE 4-10 Correlation (heat map diagram) between various effective parameters on the FS

CHAPTER 5

EROSION BEHAVIOR RESULT

This chapter presents the experimental results obtained from the erosion tests, which are divided into two main parts.

The first part focuses on quantitative results, such as sediment yield, surface runoff volume, and infiltration volume. These are presented in the form of rates, cumulative results, and total results within the test flumes with varying soil bulk densities. The testing periods are defined as follows: bare soil, soil planted with Wedelia Trilobata at ages 1 to 3 months, and the decaying/drought-killed stage.

The second part of this chapter presents the results obtained from using LiDAR technology to model and create a Digital Elevation Model (DEM) of the test plots. The resulting data illustrates the characteristics of erosion and the behavior that occurred on the soil surface when tested during each event period.

5.1 Erosion result

5.1.1 Summary of cumulative erosion result in each rainfall event

The erosion behavior test comprised three main parameters: sediment yield, surface runoff volume, and infiltration volume. The test utilized a rainfall hyetograph (shown in Figures 3-12 and 3-13), which was derived from a 25-year return period analysis. The rain application was conducted simultaneously on all three test flumes. During the test, collection was performed every 5 minutes for the tank containing the surface runoff and the eroded sediment. This collected mixture was subsequently dried (air-dried) to separate the volume of sediment from the volume of water. Additionally, water obtained from infiltration was collected every 10 minutes during each test event. As shown in figure 5-1

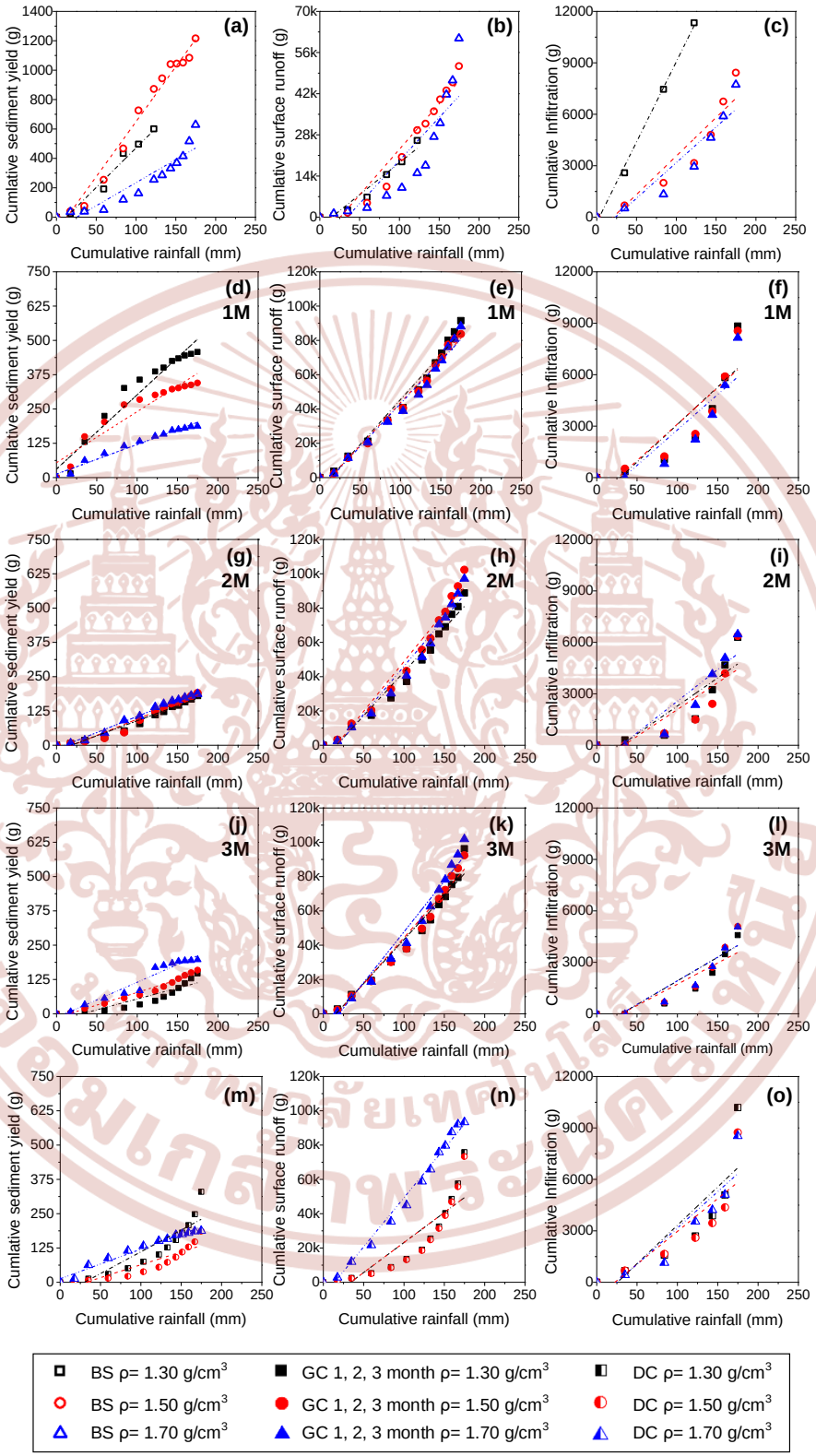


FIGURE 5-1 Summary of cumulative erosion result in each rainfall event

Figure 5-1a displays the cumulative sediment yield during the erosion test of bare soil slopes with different bulk densities. It was found that the test flume with a soil density of 1.30 g/cm^3 measured a sediment yield of 601.1 grams. Since the soil slope failed at 35 minutes, the sediment yield is summarized for the 30-minute test period. When the soil density in the test flume was increased to 1.50 g/cm^3 and 1.70 g/cm^3, the slopes maintained stability throughout the 60-minute test duration. The soil slope with a density of 1.50 g/cm^3 had an eroded sediment yield of 1,215 grams, and the soil slope with a density of 1.70 g/cm^3 had an eroded sediment yield of 628 grams. This result shows an increase in sediment yield; it is observed that loose to moderately dense soil tends to produce a greater volume of sediment than high-density soil. This is because the soil mass in higher-density soil is better compacted, resulting in less erosion when rain impacts the soil surface.

Figure 5-1b displays the cumulative surface runoff during the erosion test of bare soil slopes with different bulk densities. It was found that the test flume with a soil density of 1.30 g/cm^3 measured a surface runoff volume of 26,069 grams. Since the soil slope failed at 35 minutes, the surface runoff is summarized for the 30-minute test period. When the soil density in the test flume was increased to 1.50 g/cm^3 and 1.70 g/cm3, the slopes maintained stability throughout the 60-minute test duration. The soil slope with a density of 1.50 g/cm^3 had a surface runoff volume of 51,358 grams, and the soil slope with a density of 1.70 g/cm^3 had a surface runoff volume of 60,818 grams. This result shows a trend of increasing surface runoff volume for soil slopes with different bulk densities. When rainwater falls on looser soil, the water flows into the soil mass. Looser or moderately dense soil has more pore space, which causes the water that impacts the surface not to flow as much along the soil surface.

Figure 5-1c displays the cumulative infiltration during the erosion test of bare soil slopes with different bulk densities. It was found that the test flume with a soil density of 1.30 g/cm^3 measured an infiltration volume of 11,337 grams. Since the soil slope failed at 35 minutes, the infiltration volume is summarized for the 30-minute test period. When the soil density in the test flume was increased to 1.50 g/cm^3 and 1.70 g/cm^3, the slopes maintained stability throughout the 60-minute test duration. The

soil slope with a density of 1.50 g/cm^3 had an infiltration volume of 8,425 grams, and the soil slope with a density of 1.70 g/cm3 had an infiltration volume of 7,725 grams. The results indicate that in looser soil, when rainwater falls, the water flows through the soil mass via the larger pore spaces more easily than in dense soil, which has less pore space. This result is consistent with the observed surface runoff, where a greater surface runoff volume indicates less water infiltration into the soil mass.

Figure 5-1d displays the cumulative sediment yield during the erosion test of soil slopes planted with one-month-old Wedelia Trilobata at different bulk densities. The measured sediment yields at the end of the test were 458, 344, and 188 grams, respectively. It can be seen that the Wedelia Trilobata helped the soil slopes avoid failure throughout the 60-minute test. In this test, it was found that the cover crop helped prevent the disintegration of the soil mass caused by rainwater impact. However, the trend of sediment yield still showed a greater amount in the looser soil due to its lower density, which made it easily erodible. In the test flumes with moderate and high density, the planting of the cover crop significantly reduced the amount of erosion. This suggests that the soil density remains the primary factor affecting the amount of erosion, while the plant helps to increase the overall strength of the soil mass.

Figure 5-1e displays the surface runoff volume during the erosion test of soil slopes planted with one-month-old Wedelia Trilobata at different bulk densities. The measured surface runoff volumes at the end of the test were 91,536, 83,719, and 88,101 grams, respectively. It is evident that the Wedelia Trilobata helped the soil slopes avoid failure throughout the 60-minute test. Considering the test results, it was found that the Wedelia Trilobata caused the surface runoff volume to increase compared to the unplanted slopes. This occurred because the soil surface, even after only one month of coverage by the Wedelia Trilobata, could promote a higher surface runoff volume. However, the plant was not yet at its full efficiency after just one month of planting, and the surface runoff volume also contained components of the soil mass flowing out from the slope. Therefore, it is not possible to clearly conclude the main factor influencing the surface runoff volume, as the values obtained throughout the test did not differ significantly.

Figure 5-1f displays the infiltration volume during the erosion test of soil slopes planted with one-month-old Wedelia Trilobata at different bulk densities. At the end of the test, the measured infiltration volumes were 8,833, 8,555, and 8,149 grams, respectively. It is evident that the Wedelia Trilobata helped the soil slopes avoid failure through out the 60-minute test. Considering the test results, it was found that the Wedelia Trilobata caused the infiltration volume to decrease in each test flume, especially for the loose soil. Conversely, the moderately dense and highly dense soil showed a slight increase in infiltration volume. This is because, during the initial stage of planting (cuttings), the roots of the Wedelia Trilobata slightly penetrate the topsoil, allowing water impacting the surface to flow slightly better into the subsurface. However, while the plant does assist in loose soil, for moderately dense to dense soil, the soil density remains the primary factor influencing the infiltration volume.

Figure 5-1g shows the cumulative sediment yield during the erosion test of slopes with different densities after two months of planting. The measured sediment yields were 181, 190, and 187 grams, respectively. It is clear that after two months, the trend of sediment yield has significantly decreased, with the erosion values across all three test flumes becoming nearly equal. This suggests that in the low and moderate-density soils, where the planted Wedelia Trilobata has grown for two months, its foliage cover has developed well (better than in dense soil) and is now performing effectively. This improved coverage is the primary factor leading to the reduction in erosion. In the case of the high-density soil, although there is less plant coverage, the soil's inherent density combined with the partial foliage cover results in an erosion value that is not significantly different from the other cases.

Figure 5-1h shows the surface runoff volume during the erosion test of slopes with different densities after two months of planting. The measured surface runoff volumes were 88,797, 102,307, and 97,099 grams, respectively. After two months of planting, the trend in surface runoff volume shows a slight change. The low-density soil shows a slight decrease in surface runoff volume compared to the earlier test. However, the moderate and high-density slopes show a slight increase in surface runoff volume. This indicates that planting the cover crop on soil that is already dense can lead to a

greater volume of surface runoff than before, particularly in the moderate-density soil, where the plant can still grow well and the density is adequate. The effect is that when surface runoff occurs, the water flows along the stems and leaves upon rain impact rather than directly hitting the soil surface and infiltrating.

Figure 5-1i shows the infiltration volume during the erosion test of slopes with different densities after two months of planting. The measured infiltration volumes were 6,301, 6,375, and 6,467 grams, respectively. After two months, the trend in infiltration volume has changed, with the values obtained in this test having decreased by almost 30%. It is observed that the leaves of the Wedelia Trilobata help the impacting water land on the foliage before flowing to the runoff collection tank, rather than infiltrating into the soil mass. The low-density test plot had the lowest infiltration value, which further demonstrates that the plant is highly effective at reducing infiltration. The plant grows better in low-density soil, producing more stems and leaves than in high-density soil. Nevertheless, in the high-density soil, the inherent tightness already limits infiltration, and the added foliage cover further contributes to the reduction of the infiltration volume.

Figure 5-1j shows the cumulative sediment yield during the erosion test of slopes with different densities after three months of planting. The measured sediment yields were 147, 159, and 197 grams, respectively. From these values, it is clear that the reduction in erosion from the 2-month mark to the 3-month mark is not as substantial as the reduction observed between the 1-month and 2-month marks. Nevertheless, the Wedelia Trilobata has demonstrated its ability to help reduce the amount of sediment eroded. Additionally, at the 3-month plant age, the highest erosion value is observed in the highest-density soil. This is due to the lesser area of plant coverage, as the high density hinders better plant growth compared to the low-density soil. Consequently, the primary factor promoting the reduction in sediment yield at this age depends more on the plant coverage than on the soil density.

Figure 5-1k shows the surface runoff volume during the erosion test of slopes with different densities after three months of planting. The measured surface runoff volumes were 96,241, 92,430, and 101,807 grams, respectively. After three months of

planting, the trend in surface runoff volume has not changed significantly. While there is some reduction and increase in volume across certain test plots, the values throughout the 1- to 3-month period show slight variability. However, the results consistently reflect that when compared to the bare soil condition, the surface runoff volume across all densities has roughly doubled. The bare soil test results indicated that soil density was the factor influencing runoff volume, but with the planted cover crop, the plant itself helps enhance the increase in surface runoff. This is especially true for the high-density soil with plant cover, which further contributes to a greater volume of surface runoff.

Figure 5-1l shows the infiltration volume during the erosion test of slopes with different densities after three months of planting. The measured infiltration volumes were 4,587, 5,093, and 5,056 grams, respectively. It can be seen that at the 3-month mark, the infiltration values continue to decrease over time. However, the rate of reduction from the 2- to 3-month period is less significant than the rate from the 1- to 2-month period. It is clearly visible that the low-density test plot, with plant cover at 3 months, has an infiltration volume that is lower than both the moderate and high-density plots. This indicates that when the plant cover is fully established, rainwater hits the leaves and stems and flows into the surface runoff collection tank, rather than hitting the soil surface and infiltrating downwards. Nevertheless, the moderate-density plot, despite being slightly denser, still exhibits a high volume of infiltration. This test suggests that the main influence on infiltration volume largely remains with the soil density.

Figure 5-1m displays the cumulative sediment yield during the erosion test conducted after the plants were allowed to enter a decaying state for approximately three months (following the 3-month test). The measured sediment yields were 330, 186, and 188 grams, respectively. The graph shows that early in the test, the high-density flume tended to produce a greater amount of sediment, but this trend gradually decreased during the final 30 minutes. It is notable that even with the plants decaying, the soil density, along with the remaining dry leaves and stems, still helped ensure the resulting sediment yield did not increase significantly from when the plants were

healthy. Conversely, the low- and moderate-density test plots showed a tendency for the sediment yield to gradually increase and climb steadily. Ultimately, the low-density flume, which had the lowest erosion when the plants were healthy, ended up with a sediment yield that doubled. This is attributed to the fact that this flume originally had the most coverage; when the plant entered the decaying state, the subsequent root atrophy/decay created more voids, and the significant loss of surface cover resulted in much greater erosion than before.

Figure 5-1n shows the measured surface runoff volumes were 75,841, 73,316, and 93,330 grams, respectively. It is observed that the high-density test plot shows a surface runoff trend similar to when the plants were healthy, although the total runoff volume decreased by about 10%. This indicates that even in the decaying state, the high-density soil still promotes a good volume of surface runoff. In the case of the low- and moderate-density soils, the surface runoff volume decreased by more than 20%, and the trend was a gradual increase that only peaked toward the end of the test. This suggests that when the plant began to decay, the stems and roots interwoven on the surface disappeared, causing water, instead of flowing along the surface, to flow through the newly created voids. Once the soil became saturated, the surface runoff volume increased in the final stages.

Figure 5-1o shows the measured infiltration volumes were 10,186, 8,732, and 8,528 grams, respectively. Across all three test plots, the infiltration volume after the plants entered the decaying stage was almost equivalent to the period before any plants were established. This reflects that when the plant decayed, the voids created by the decaying roots and the interwoven stems on the surface disappeared, leading to a greater volume of infiltration than before. Even with dry leaves and stems covering the surface, water could still flow easily through these gaps. However, despite the volume being similar to the unplanted state, the slopes did not fail during the test.

5.1.2 Total Sediment yield with Ground coverage in each rainfall event

This section focuses on the analysis of cumulative sediment yield as presented in Figure 4-2, evaluating the performance of slopes under various conditions. The primary

objective is to determine how soil bulk density and the growth stages of the Wedelia Trilobata cover crop affect the stability of the soil and the magnitude of erosion. The analysis begins by establishing a baseline using bare soil tests to quantify the fundamental influence of density on sediment loss. This is followed by a stage-by-stage examination of erosion results corresponding to plant ages of 1, 2, and 3 months, correlating the significant increase in plant cover percentage with the progressive reduction in sediment yield. A critical part of this investigation is the assessment of the soil's stability after the plant enters a drought-killed/decaying state (after 3 months of no watering). This final stage evaluates the residual effect of the root system and dried biomass in mitigating erosion compared to the healthy plant and bare soil conditions.

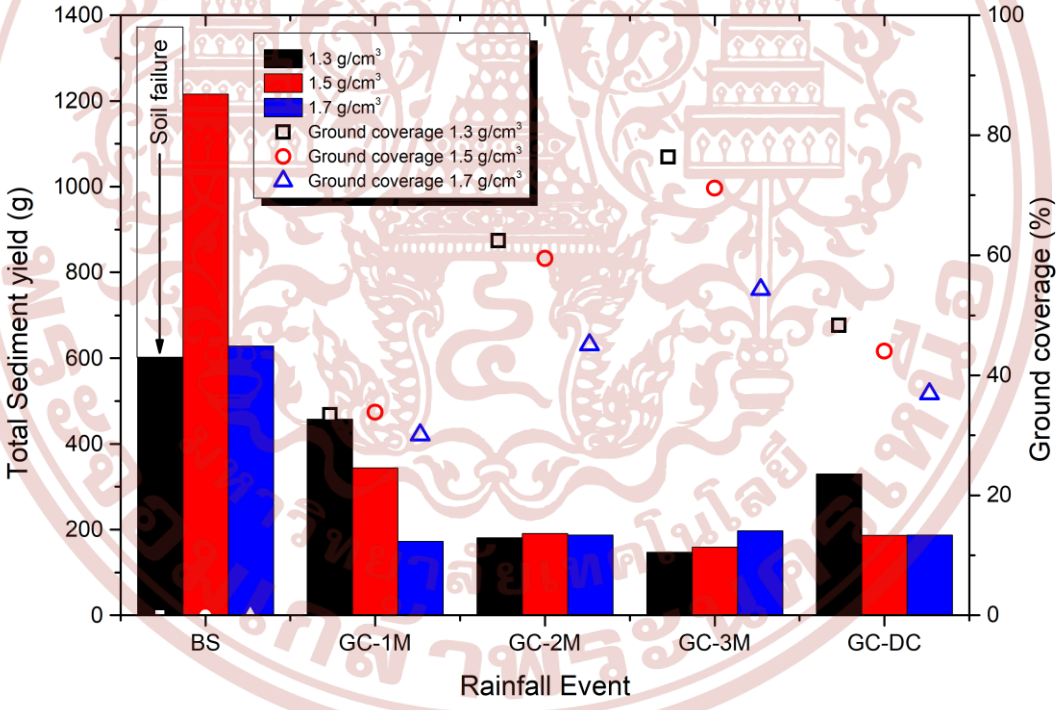


FIGURE 5-2 Total Sediment yield with Ground coverage in each rainfall event

The test flume with a soil density of 1.30 g/cm^3 measured a sediment yield of 601.1 grams; however, the slope failed at 35 minutes, so the result is summarized for the 30-minute test period. For the flumes with increased soil densities (1.50 and

1.70 g/cm^3), the slopes maintained stability throughout the 60-minute test. The 1.50 g/cm^3 slope had an eroded sediment yield of 1,215 grams, and the 1.70 g/cm3 slope had 628 grams. These results show that the primary factor influencing sediment erosion is the soil bulk density. Soil with better compaction tends to yield less sediment when impacted by rainfall, meaning looser soil produces more sediment than denser soil.

After planting Wedelia Trilobata for 1 month, the test flumes with densities of 1.30, 1.50, and 1.70 g/cm^3 had plant cover percentages of 33%, 33%, and 30%, respectively. Subsequent erosion tests showed that the *Wedelia Trilobata* helped the slopes avoid failure throughout the 60-minute test in all flumes, with measured erosion volumes of 457, 344, and 172 grams, respectively. Comparing the cumulative sediment yields, the erosion trend remains similar to the bare soil case; the lowest-density soil still had the highest erosion. Since the plant cover percentages were not significantly different and not very high across the three flumes, the cover did not heavily influence the erosion values. Nonetheless, the 1-month-old cover crop was able to reduce the eroded sediment volume by over 70% in every test flume compared to the bare soil condition.

After 2 months of planting, the plant cover percentage increased significantly. The cover increased from 33.31%, 33.86%, and 30.04% (for low to high density) to 62.46%, 59.47%, and 44.79%, respectively. The low- and moderate-density flumes (1.30 and 1.50 g/cm^3) showed an increase in cover percentage of over 90% compared to the 1-month period, which is due to better plant growth in less dense soil. The sediment yield resulting from the simulated rainfall erosion was 181.3, 190.4, and 187.64 grams for low to high-density flumes, respectively. The overall decrease in sediment yield correlates with the plant growth duration, especially at the 2-month mark, where the plant cover began to clearly affect the erosion process. The measured sediment volume decreased significantly by more than a factor of two compared to the previous period for the moderate- and high-density flumes. Although the sediment values were similar, it can be seen that there is a combined factor of increased plant cover and soil density contributing to erosion resistance. The increased density helps

reduce water permeability and increases particle cohesion, while the plant cover reduces the impact force from raindrops and surface runoff. Both factors play a complementary role in reducing topsoil loss in this scenario.

After 3 months of planting, the cover percentage increased to 76.38%, 71.20%, and 54.16%. The rate of increase in cover was lower at the 3-month mark compared to the increase from 1 to 2 months. Furthermore, the sediment erosion volume was substantially reduced, with plant cover becoming the primary factor. The low-density soil, which had the highest cover rate, had the lowest erosion volume, followed by the moderate-density soil, and finally the highest-density soil. At the 3-month plant age, the soil density no longer had a dominant impact on the amount of erosion.

Subsequently, when the plants were left in a drought-killed/decaying state, the plant cover rate decreased to 47.83%, 44.02%, and 36.74%, respectively. Plant death caused the leaves and stems of the *Wedelia Trilobata* to dry and shrink. Upon conducting the erosion test, the 1.30 g/cm^3 (low-density) soil had the highest volume of eroded soil. This resulted from the loss of cover by 28.55%, combined with the soil's inherently low density, which led to a greater sediment yield than the denser soils. In the case of the 1.50 g/cm3 (moderate-density) soil, which had a high initial cover rate, the sediment from erosion increased only slightly. The 1.70 g/cm3 (high-density) soil, which was already very dense and had a smaller loss of cover rate, did not show a significant difference in eroded sediment volume.

From all tests, it is concluded that low-density slopes cannot maintain stability indefinitely under erosion. However, planting *Wedelia Trilobata* for 2 months or more significantly reduces the eroded sediment volume. In the drought-killed state, the loss of cover is greater in the low-density soil compared to the high-density soil. Nevertheless, since high-density soil already yields a lower sediment volume, and a considerable percentage of cover still remained, the resulting increase in sediment volume was not substantial.

5.1.3 Total Surface runoff with Ground coverage in each rainfall event

This section focuses on the analysis of cumulative surface runoff volume as presented in Figure 5-3. The primary goal is to investigate how soil bulk density and the progressive growth stages of the Wedelia Trilobata cover crop influence the hydrological response of the slopes under simulated rainfall. Understanding the factors that control the partitioning of rainfall—between infiltration into the soil mass and runoff across the surface—is critical for assessing slope stability and hydrological modeling. The analysis is structured chronologically, starting with the bare soil phase to establish the baseline influence of density on runoff generation. This is followed by a stage-by-stage evaluation at 1, 2, and 3 months of plant growth, examining how increasing plant canopy and root development alter the surface flow characteristics. Crucially, the section concludes with the results from the drought-killed/decaying state test. This evaluation helps determine the persistence of the plant's influence on surface runoff once its active vegetative protection is lost. The overall findings reveal a complex interaction where plant cover tends to increase surface runoff initially by intercepting water, while soil density remains the long-term dominant factor, particularly in dense soils.

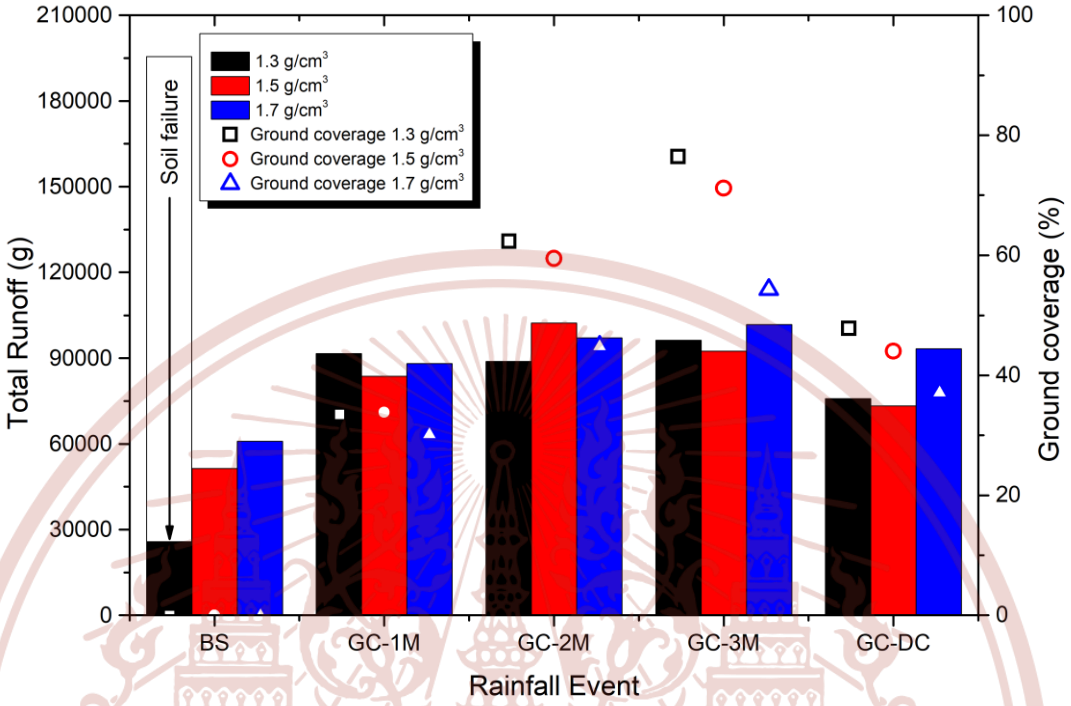


FIGURE 5-3 Total Surface runoff with Ground coverage in each rainfall event

The test flume with a soil density of 1.30 g/cm3 measured a surface runoff volume of 26,069 grams; however, the slope failed at 35 minutes, so the result is summarized for the 30-minute test period. For the flumes with increased soil densities (1.50 and 1.70 g/cm^3), the slopes maintained stability throughout the 60-minute test. The 1.50 g/cm^3 slope had a runoff volume of 51,358 grams, and the 1.70 g/cm^3 slope had 60,818 grams. These results show that the primary factor influencing surface runoff volume is the soil bulk density. Denser soil tends to have less water infiltration, causing water to flow across the surface and into the collection tank. Conversely, in looser soil, water tends to infiltrate into the soil mass rather than runoff.

After planting Wedelia Trilobata for 1 month, the test flumes with densities of 1.30, 1.50, and 1.70 g/cm^3 had plant cover percentages of 33%, 33%, and 30%, respectively. Subsequent runoff tests showed that the *Wedelia Trilobata* helped the slopes avoid failure throughout the 60-minute test in all flumes, with measured surface runoff volumes of 91,536, 83,719, and 88,101 grams, respectively.

Comparing the cumulative surface runoff volumes, the runoff trend increased significantly by 71.52%, 38.65%, and 30.968% respectively, compared to the bare soil test. It is observed that with plant cover, infiltration decreases because rainwater impacts the stems and leaves of the *Wedelia Trilobata* before flowing into the collection tank, rather than hitting the soil surface directly. Since the cover percentages were not significantly different across the three flumes at 1 month, a clear conclusion about the dominance of cover ratio versus density cannot be drawn. However, the low-density flume, which previously failed at only 26,069 grams of runoff, was able to handle the increased runoff volume and remained stable after planting. For the moderate- and high-density soils, the planting of the cover crop further enhanced the already high surface runoff volume caused by the soil's inherent density.

After 2 months of planting, the plant cover percentage increased significantly from the initial 33.31%, 33.86%, and 30.04% (for low to high density) to 62.46%, 59.47%, and 44.79%, respectively. The low- and moderate-density flumes showed a cover increase of more than 90% compared to the 1-month period due to better plant growth in less dense soil. The surface runoff volumes measured were 88,797, 102,307, and 97,099 grams, respectively. For the low-density soil, the slight reduction in runoff volume at 2 months is attributed to the increased sediment yield (as shown in Figure 4-1), which meant less water was collected as runoff. Conversely, in the moderate-density soil, the increase in runoff volume correlates with the plant's growth period. Here, the combined influence of soil density and increased plant cover contributed to the higher surface runoff. For the high-density soil, the runoff volume was still primarily influenced by the soil's inherent density, and the increase in cover percentage did not significantly raise the surface runoff volume further.

After 3 months of planting, the cover percentage increased to 76.38%, 71.20%, and 54.16%. The rate of cover increase slowed down compared to the 1-to-2-month period. The surface runoff volumes measured were 96,241, 92,430, and 101,807 grams, respectively. For the low-density soil, the collected runoff volume continued to increase from both the bare soil and previous planted stages, although the rate of increase was much smaller between 1 and 3 months. The moderate-density flume showed a slight,

non-significant decrease in runoff compared to the 2-month test. The high-density flume showed a slight increase in runoff from the 2-month mark. It is observed that even with a 9% increase in cover, the canopy was not the main factor influencing the surface runoff volume at this stage.

Subsequently, when the plants were allowed to enter a drought-killed/decaying state, the plant cover rate decreased to 47.83%, 44.02%, and 36.74%, respectively. The surface runoff volumes measured were 75,841, 73,316, and 93,330 grams, respectively. For the low- and moderate-density flumes, the loss of plant cover resulted in a runoff volume decrease of approximately 21%. This indicates that when the *Wedelia Trilobata* cover decays, the surface water is able to infiltrate more into the soil mass, reducing the collected runoff. Conversely, in the high-density soil, despite a similar loss of cover, the runoff volume decreased by only 9%. This demonstrates that the soil density remains the dominant influence on runoff volume in dense soils.

The tests confirm that low-density slopes cannot maintain stability when subjected to high volumes of surface runoff. However, planting *Wedelia Trilobata* for 1 month or more significantly increases the surface runoff volume while stabilizing the slope. In the 2-to-3-month growth period, the overall trend is an increase, though not a substantial one. Conversely, during the drought-killed state, the loss of cover is more pronounced in the loose and moderate-density soils, causing a significant reduction in their surface runoff volumes. The runoff volume in the high-density soil, however, did not change much, leading to the conclusion that the primary influence on surface runoff volume in this condition is soil density.

5.1.4 Total Infiltration with Ground coverage in each rainfall event

This section presents the analysis of the cumulative infiltration volume as shown in Figure 5-4, focusing on the inverse relationship between surface cover, soil density, and the amount of water absorbed by the soil mass. Infiltration is a critical component of the soil-water balance, directly influencing the amount of water available for surface runoff and, subsequently, the potential for erosion and slope failure. The analysis first establishes that soil bulk density is the primary control on infiltration in bare soil, where

looser soil facilitates greater water entry. The subsequent phases—covering plant growth at 1, 2, and 3 months—investigate how the Wedelia Trilobata cover crop alters this relationship. Specifically, the data demonstrates that as plant cover increases, the water partitioning shifts, with less water reaching the soil surface to infiltrate.

Finally, the section examines the results from the drought-killed/decaying state to assess the long-term changes in soil structure (due to root decay) and the resulting impact on infiltration capacity. This comprehensive analysis highlights the complex interplay between plant development, soil physical properties, and the soil's ability to absorb water across different stages of the experiment.

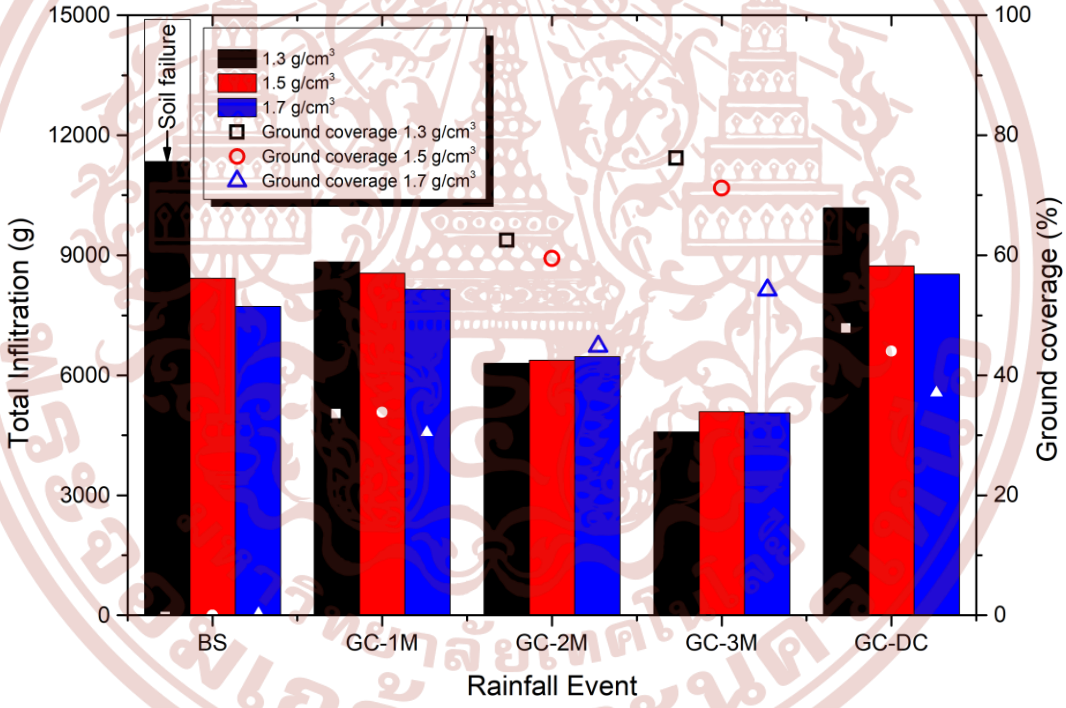


FIGURE 5-4 Total Infiltration with Ground coverage in each rainfall event

The test flume with a soil density of 1.30 g/cm3 measured an infiltration volume of 11,337 grams; however, the slope failed at 35 minutes, so the result is summarized for the 30-minute test period. For the flumes with increased soil densities (1.50 and 1.70 g/cm^3), the slopes maintained stability throughout the 60-minute test. The

1.50 g/cm^3 slope had an infiltration volume of 8,425 grams, and the 1.70 g/cm^3 slope had 7,725 grams. These results confirm that soil bulk density is the primary factor influencing infiltration volume. Looser soil allows water to easily flow through the larger pore spaces, resulting in a higher infiltration volume than in moderate- and high-density soils. In dense soil, the small pore spaces restrict water entry, causing the rain to flow across the surface instead.

After planting Wedelia Trilobata for 1 month, the test flumes with densities of 1.30, 1.50, and 1.70 g/cm^3 had plant cover percentages of 33%, 33%, and 30%, respectively. Subsequent infiltration tests showed that the *Wedelia Trilobata* helped the slopes avoid failure throughout the 60-minute test in all flumes, with measured infiltration volumes of 8,833, 8,555, and 8,149 grams, respectively. Comparing the cumulative infiltration volumes, the low-density flume showed a notable decrease of 28.35%, indicating that the initial plant cover effectively reduced infiltration. Conversely, the moderate- and high-density slopes showed a slight increase in infiltration, though the difference was not statistically significant compared to the bare soil test. The prevailing influence was still soil density. The slight increase is attributed to the initial root growth *loosening* the topsoil as the plant established itself, causing the measured infiltration volume to rise slightly to 8,555 and 8,149 grams respectively.

After 2 months of planting, the plant cover percentage increased significantly, rising from 33.31%, 33.86%, and 30.04% to 62.46%, 59.47%, and 44.79%, respectively. The low- and moderate-density flumes saw an increase in cover of over 90%. The simulated rainfall resulted in infiltration volumes of 6,301, 6,374, and 6,466 grams, respectively. The overall reduction in infiltration is clearly correlated with the extended plant growth. At 2 months, the increased plant cover significantly impacts infiltration because rainwater hits the foliage rather than the soil surface, leading to greater interception and runoff generation, and less water available for infiltration. Notably, the low- and moderate-density flumes showed lower infiltration than the high-density flume. However, due to the high inherent density and limited pore space of the densest soil, the infiltration values across all three flumes were not significantly different.

After 3 months of planting, the cover percentage increased to 76.38%, 71.20%, and 54.16%. The rate of cover increase slowed down compared to the 1-to-2-month period. The infiltration volumes measured were 4,587, 5,093, and 5,056 grams, respectively. The further reduction in infiltration confirms that plant cover is the main factor. The low-density soil, with the highest cover, recorded the lowest infiltration. The dense canopy ensures that rainwater hits the stems and leaves and flows to the surface runoff tank (as shown in Figure 5-2) rather than penetrating the soil. This effect is clearest in the low-density flume, where high cover dramatically lowered infiltration. The moderate-density flume, despite 71.20% cover, showed an infiltration volume similar to the high-density flume, indicating that the combined influence of density and cover dictates the result, unlike the bare soil phase where density was solely responsible.

When the plants were allowed to enter a drought-killed/decaying state, the plant cover rate decreased to 47.83%, 44.02%, and 36.74%, respectively. The resulting infiltration volumes were 10,186, 8,731, and 8,528 grams.

For the low-density flume, the extensive cover loss created significant voids from root atrophy, and the soil's inherently low density caused the infiltration volume to more than double compared to the 3-month healthy state. The final value approached the initial bare soil value. For the moderate- and high-density flumes, the infiltration volume increased by 72.68% from the 3-month healthy state and even exceeded the bare soil value slightly. This demonstrates that once the plants decay, the protective effect is lost, and the loss of root binding structure can slightly increase permeability, particularly in the already-dense soils.

The tests show that low-density slopes eventually fail under erosion. However, planting Wedelia Trilobata for 2 months or more significantly reduces the infiltration volume. During the drought-killed state, the loss of cover is most severe in the low-density soil, causing infiltration to revert to near-bare soil levels. In the high-density soil, where infiltration was already low, the loss of cover resulted in the infiltration volume returning to a value close to the bare soil test.

5.2 Runoff rate and Sediment rate compared with Bare soil and Groundcover

Figure5-5 (a), (b), and (c) show that bare soil consistently produces higher runoff rates compared to ground cover across all densities. In cases of bare soil, the runoff rate increased rapidly at first and then gradually decreased as time passed. For the lowest density tray, the soil slope failed at 30 minutes. A similar trend is observed in ground cover cases. The runoff rate on the underlying surface increased at the beginning until the time of 10 minutes the runoff rate gradually decreased as time progressed. The runoff rates for bare soil exhibit more pronounced peaks and fluctuations, while ground cover maintains lower, more stable rates. The results indicate that soil density did not significantly impact the runoff for the ground cover cases compared to the bare soil in any of the tests. in this experiment, the rainfall intensity was simulated to be higher during the first 20 minutes. After that, the rainfall intensity gradually decreased, reflecting the distribution of rainfall over time in Thailand within an hour. This resulted in a reduction in the runoff volume over time

Figure 5-5(d), (e), and (f) show bare soil produces much greater sediment rates than ground cover at all densities. In the 1.7 g/cm^3 density, the bare soil sediment rates exhibit more significant variability and higher peaks. The presence of ground cover consistently ensures reduced sediment rates with less fluctuation.

In Figure 5-5 (g), (h), and (i), it is shown that bare soil typically leads to greater sediment concentrations in comparison to ground cover. However, the disparity is less significant than in the case of runoff and sediment rates. The sediment concentration patterns exhibit greater variability with densities, with certain cases of ground cover showing similar or slightly higher concentrations during specific rainfall periods. For bare soil cases, sediment production exhibited successive fluctuations with several spikes and drops and varied rapidly as the flow discharge increased. The findings indicate that soil density and ground cover are important factors in determining erosion evolution. Ground cover improves erosion control for various rainfall durations and soil densities.

Form The experiment, runoff, and sediment reduction depend on the coverage area of Wedelia Tribolata provided by its stems and leaves, which grow well during the

rainy season. However, the experiment is not yet complete, the root structure has not been examined. However, a detailed inspection will be conducted once the experiment is finished.

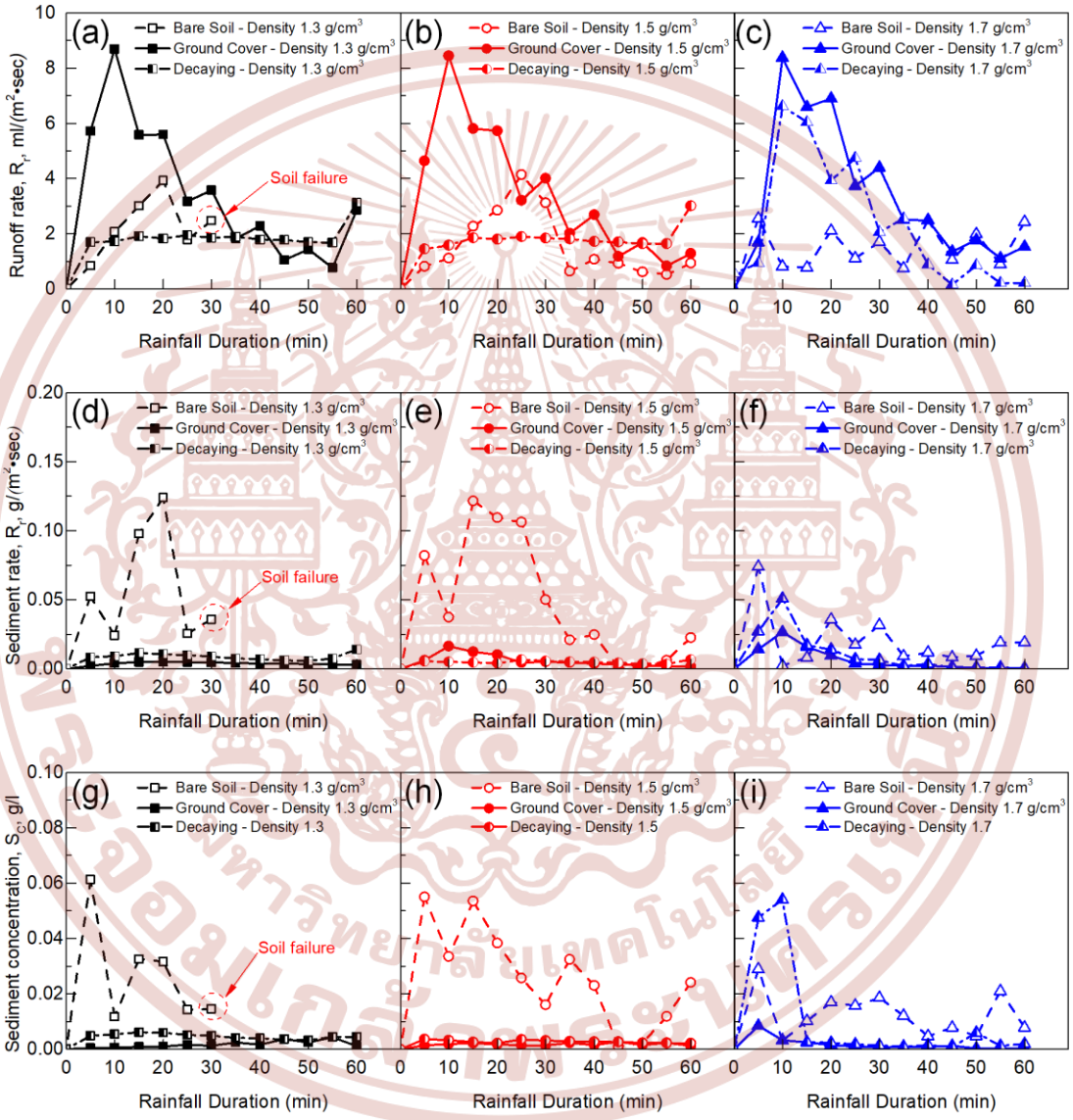


FIGURE 5-5 Runoff rate and Sediment rate compared with Bare soil and Groundcover

5.3 Analyzing Erosion Behavior Using DEM

Figure5-6 and Figure 5-7 show the DEM characteristics of the ground cover that affect the rate and development of runoff on the soil slope for soil density 1.3, 1.5 and 1.7 g/cm^3, respectively. The color scale indicates elevation from blue (low level) to red (high level), with green representing the mid-range elevations. Both figures show that the initial condition exhibits a uniform topography, mainly green shades. This indicates that the soil surface was relatively flat and undisturbed before erosion testing, as evidenced by the minimal variation and moderately elevated surface. For bare soil cases, significant topographical changes are evident for the low-density tray after the first rainfall. A pronounced area has formed, shown in blue, which implies significant soil erosion and a lower elevation area. The large area of blue in Fig. 8 can be noticeably seen, indicating the soil failure at 30 minutes of rainfall. Meanwhile, the slope of the bare soil did not fail because of the high density. The topography exhibits a patterned mosaic of green color for the ground cover cases. This observation indicates multiple micro-topographies, which could be related to the protective mechanisms of ground cover plants that diminish soil erosion. The distribution characteristics of ground cover impacted the runoff, sedimentation, and concentration rate, leading to diminishing surface runoff rate characteristics under the action of intermittent rainfall events.

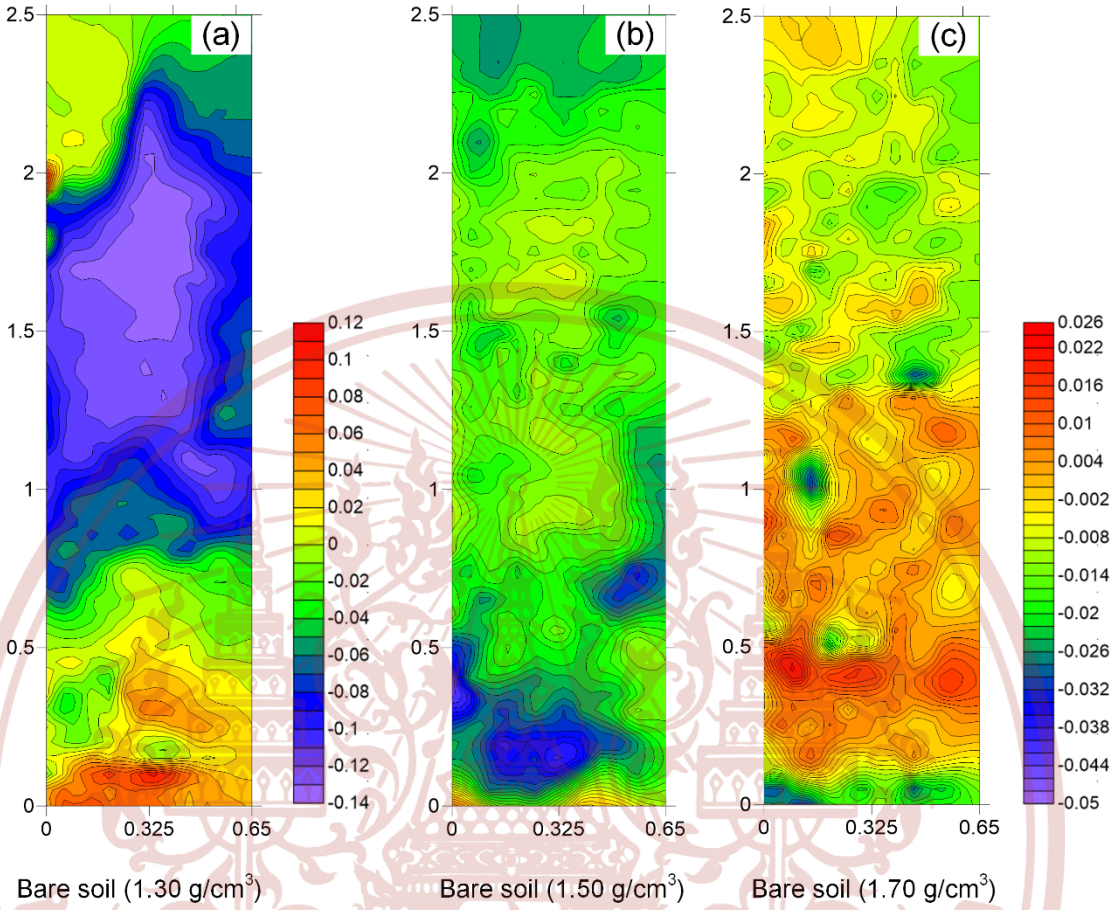


FIGURE 5-6 DEM characteristics of the erosion process bare soil (Before-after)

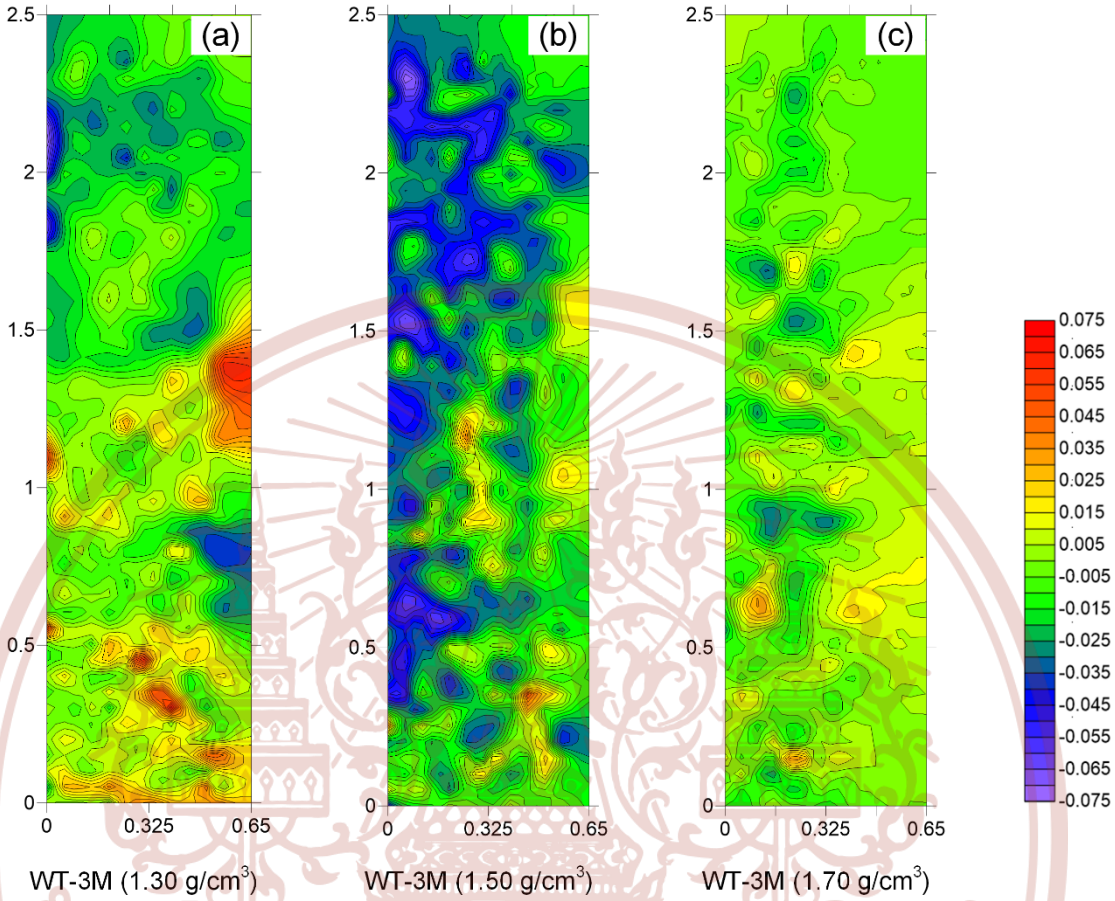


FIGURE 5-7 DEM characteristics of the erosion process groundcover (2 and 3 months)

CHAPTER 6

CONCLUSION

6.1 Root biomechanical result

This study systematically investigated the root system architecture of *W. trilobata* and its potential for embankment reinforcement under controlled conditions using a rhizobox setup. The influence of soil type on RSA and biomechanical properties was comprehensively assessed. Key parameters such as root area ratio (RARs), diameter distribution, and root orientation were quantified, and the resulting root cohesion (C_r) values were derived and incorporated into slope stability assessments. Based on the results obtained from this study, the following conclusions can be drawn.

1) *W. trilobata* exhibits distinct root system responses to contrasting soil media. In rice husk ash (RHA), roots demonstrate higher root area ratios (RAR_s), finer diameters, and extensive lateral branching, reflecting adaptation to the loose soils, low-density substrates. Conversely, roots grown in lateritic soil show deeper penetration, larger diameters, and limited lateral expansion due to soil compaction, but benefit from higher nutrient content.

2) The root system of *W. trilobata* observed in this study displays features consistent with tufted root systems, commonly associated with species in the Poaceae family. The RAR_s profiles show a notable concentration in the mid-root zone (approximately 400–600 mm) at both growth stages, with the peak values shifting slightly deeper after 90 days. This indicates progressive root proliferation toward sublayers, likely associated with enhanced resource exploration over time. The zone of elevated RAR_s coincided with a visibly higher number of lateral roots branching from the primary root axis, thereby increasing cumulative root surface area.

3) The root biomechanical of *W. trilobata* roots reveals that both tensile strength and Young's modulus decrease with increasing root diameter, a trend consistent with prior studies on vetiver species. While *W. trilobata* exhibits lower tensile strength and

stiffness compared to C. *nemoralis* and C. *zizanioides*, its dense, fine root network with high branching compensates for mechanical limitations.

4) The integration of root architectural traits and mechanical properties of *W. trilobata* confirms its potential for soil reinforcement through the development of root-induced cohesion (C_r). Results show that growth in rice husk ash (RHA) produces higher RARs and a marked increase in tensile strength over time, leading to C_r values rising from 0.80 kPa at 60 days to 3.92 kPa at 90 days. In contrast, lateritic soil promotes deeper root penetration and higher tensile strength, but the comparatively lower RARs limit the increase in C_r to 3.56 kPa. These findings emphasize that while root mechanical strength is critical in compact soils, the greater lateral branching and RARs in RHA enhance root–soil interaction, yielding superior reinforcement.

5) The slope stability analysis shows that reinforcement by *W. trilobata* roots significantly enhances the factor of safety, especially in shallow slope conditions. While the enhancement is more limited on higher slopes, the incorporation of roots consistently improves stability.

6) The results indicate that the reinforcing effect of *W. trilobata* is most effective in shallow and steep slope conditions. At low slope heights (2.0 m), the factor of safety increases by up to 28%, whereas at greater heights (6.0 m) the improvement is limited to less than 10% as the failure surface develops deeper than the root zone. Steeper slopes (1:1) also benefit more from reinforcement compared with flatter slopes, since the critical slip surface intersects the root-reinforced zone and mobilizes stronger root–soil interaction. In contrast, flatter slopes exhibit failure surfaces largely below the reinforced zone, reducing the relative contribution of roots to stability.

7) The correlation analysis demonstrates that the contribution of *W. trilobata* to slope stability is governed by both slope geometry and root development. For steep slopes with a 1:1 ratio, C_r and root age are the dominant variables influencing the factor of safety, reflecting the progressive increase in tensile strength and cohesion between 60 and 90 days of growth. In contrast, when slopes become flatter, the influence of root depth and diameter is diminished, and stability is predominantly controlled by C_r. This effect is particularly evident at higher slope heights, where the

failure plane often develops deeper than the root zone, reducing the impact of structural root traits and emphasizing the central role of C_r in maintaining slope stability.

6.2 Erosion behavior result

The study concludes that soil bulk density is the primary factor influencing sediment yield, surface runoff, and infiltration in bare soil conditions, but the presence and growth of Wedelia Trilobata dramatically alter these relationships over time.

1) Effect of Soil Density on Erosion Behavior (Bare Soil Condition) Under the Bare Soil (BS) Condition, soil bulk density was the primary factor influencing slope stability and water movement. The low-density soil was highly unstable, resulting in slope failure within 35 minutes of rainfall, while higher-density slopes maintained stability throughout the 60-minute test. Looser soil produced a greater volume of sediment due to poor compaction, but exhibited the highest infiltration rate because large pore spaces allowed for easy water flow. Conversely, denser soil resulted in higher surface runoff and lower infiltration, as smaller pore spaces restricted water entry.

2) Effect of Wedelia Trilobata (Ground Cover - GC) The introduction of the Ground Cover (GC) plant, Wedelia trilobata, rapidly and dramatically altered the density-erosion relationship. Planting for only one month was sufficient to help all soil slopes, including the low-density one, avoid failure throughout the 60-minute test, highlighting the immediate stabilizing role of the root system.

3) Sediment Yield Reduction as Plant Cover, Increases The capacity for erosion resistance increased significantly with the plant's growth over time. Planting for two months or more significantly reduced the volume of eroded sediment across all densities. By the two-month mark, the increased foliage cover became the primary factor in reducing erosion, leading to the sediment values for all three densities becoming nearly equal. By three months, plant coverage was clearly the dominant factor for erosion resistance, outweighing the influence of soil density.

4) Surface Runoff as Plant Cover Increases, The ground cover significantly increased the surface runoff volume (roughly doubling it compared to bare soil) across all densities. This occurred because the plant's stems and leaves intercepted rainwater, promoting its flow toward the collection tank rather than infiltration. This effect was more pronounced in the high-density soil with plant cover, indicating that while the plant reduces sediment, it increases the volume of water flowing across the surface.

5) Infiltration as Plant Cover Increases, As plant cover increased (especially from two to three months), the infiltration volume was significantly reduced because less water successfully reached the soil surface. This confirmed the role of plant interception

as the key factor. At three months, the low-density soil, which had the highest plant cover, recorded the lowest infiltration, a complete reversal of its behavior under bare soil conditions.

6) Decaying/Drought-Killed (GC-DC) State, When the ground cover entered the Decaying/Drought-Killed (GC-DC) State, the vulnerability to erosion increased, particularly in the low-density soil. This soil showed the highest volume of eroded sediment due to the combination of its low inherent density and the greatest loss of plant cover, where root atrophy created voids that compromised structural integrity. For the moderate and high-density soils, however, the remaining dry biomass and high soil density helped ensure the sediment yield did not increase substantially from the healthy plant state. Intriguingly, the infiltration volume across all plots reverted to a level similar to the bare soil period, as root decay and loss of surface cover increased soil permeability.

REFERENCES

Abrantes, J. R. C. B., Prats, S. A., Keizer, J. J., & de Lima, J. L. M. P. (2018). Effectiveness of the application of rice straw mulching strips in reducing runoff and soil loss: Laboratory soil flume experiments under simulated rainfall. Soil and Tillage Research, 180, 238–249. https://doi.org/10.1016/j.still.2018.03.015

Ahmed, H., Hazari, S., & Das, P. (2024). Influence of Tea Plant Roots for Soil Slope Strengthening: Case Studies and Numerical Investigation. Transportation Infrastructure Geotechnology, 11(4), 1389–1414. https://doi.org/10.1007/s40515-023-00350-x

Armengaud, P., Zambaux, K., Hills, A., Sulpice, R., Pattison, R. J., Blatt, M. R., & Amtmann, A. (2009). EZ- Rhizo: integrated software for the fast and accurate measurement of root system architecture. The Plant Journal, 57(5), 945–956. https://doi.org/10.1111/j.1365-313X.2008.03739.x

Armstrong, A. (2007). An Integrated Approach to Establishing Native Plants An Integrated Approach to Establishing Native Plants An Integrated Approach to Establishing Native Plants An Integrated Approach to Establishing Native Plants Roadside Revegetation.

Arrington, W. (2022). SOIL EROSION - CAUSES, EFFECTS, AND PREVENTION. International Journal of Agriculture, Environment and Bioresearch, 06(06), 226–235. https://doi.org/10.35410/IJAEB.2021.5696

ASTM International. (2007). Standard test method for determination of water (moisture) content of soil by direct heating (ASTM D4959-07). West Conshohocken, PA: ASTM International. https://doi.org/10.1520/D4959-07

ASTM-D2487. 2011. “Standard Classification of Soils for Engineering Purposes (Unified Soil Classification System).” In. West Conshohocken, PA: ASTM International.

ASTM-D698. 2012. “Standard Test Methods for Laboratory Compaction Characteristics of Soil Using Standard Effort.” In. West Conshohocken, PA: ASTM International.

ASTM International. (2015). ASTM D1556/D1556M-15: Standard test method for density and unit weight of soil in place by sand-cone method. West Conshohocken, PA: ASTM International. https://doi.org/10.1520/D1556_D1556M-15

ASTM-D854. 2023. “Standard Test Methods for Specific Gravity of Soil Solids by Water Pycnometer.” In. West Conshohocken, PA: ASTM International.

Ashour, M., & Ardalan, M. H. (2010). Road Embankment and Slope Stabilization.

Aziz, S., & Islam, M. S. (2023). Erosion and runoff reduction potential of vetiver grass for hill slopes: A physical model study. International Journal of Sediment Research, 38(1), 49–65. https://doi.org/10.1016/j.ijsrc.2022.08.005

Badhon, F. F., Islam, M. S., Islam, Md. A., & Arif, Md. Z. U. (2021). A simple approach for estimating contribution of vetiver roots in shear strength of a soil–root system. Innovative Infrastructure Solutions, 6(2), 96. https://doi.org/10.1007/s41062-021-00469-1

Bagarello, V., Ferro, V., Keesstra, S., Comino, J. R., Pulido, M., & Cerdà, A. (2018). Testing simple scaling in soil erosion processes at plot scale. *Catena*, *167*, 171–180. https://doi.org/10.1016/j.catena.2018.04.035

Bagarello, V., & Ferro, V. (2017). Scale Effects on Plot Runoff and Soil Erosion in a Mediterranean Environment. Vadose Zone Journal, 16(12), 1–14. https://doi.org/10.2136/vzj2017.03.0059

Blanco-Canqui, H., & Jasa, P. J. (2019). Do Grass and Legume Cover Crops Improve Soil Properties in the Long Term? Soil Science Society of America Journal, 83(4), 1181–1187. https://doi.org/10.2136/sssaj2019.02.0055

Browning, T. N., & Sawyer, D. E. (2021). Vulnerability to watershed erosion and coastal deposition in the tropics. Scientific Reports, 11(1), 885. https://doi.org/10.1038/s41598-020-79402-y

Boldrin, D., Leung, A. K., & Bengough, A. G. (2021). Hydro-mechanical reinforcement of contrasting woody species: a full-scale investigation of a field slope. Géotechnique, 71(11), 970–984. https://doi.org/10.1680/jgeot.19.SiP.018

Bordoni, M., Cislaghi, A., Vercesi, A., Bischetti, G. B., & Meisina, C. (2020). Effects of plant roots on soil shear strength and shallow landslide proneness in an area of northern Italian Apennines. Bulletin of Engineering Geology and the Environment, 79(7), 3361–3381. https://doi.org/10.1007/s10064-020-01783-1

Bryan, R. B. (1979). THE INFLUENCE OF SLOPE ANGLE ON SOIL ENTRAINMENT BY SHEETWASH AND RAINSPLASH. In EARTH SURFACE PROCESSES (Vol. 4).

Burt, T., Boardman, J., Foster, I., & Howden, N. (2016). More rain, less soil: long-term changes in rainfall intensity with climate change. Earth Surface Processes and Landforms, 41(4), 563–566. https://doi.org/10.1002/esp.3868

Burylo, M., Rey, F., Mathys, N., & Dutoit, T. (2012). Plant root traits affecting the resistance of soils to concentrated flow erosion. Earth Surface Processes and Landforms, 37(14), 1463–1470. https://doi.org/10.1002/esp.3248

Cabal, C., De Deurwaerder, H. P. T., & Matesanz, S. (2021). Field methods to study the spatial root density distribution of individual plants. Plant and Soil, 462(1–2), 25–43. https://doi.org/10.1007/s11104-021-04841-z

Carley, C. N., Chen, G., Das, K. K., Delory, B. M., Dimitrova, A., Ding, Y., George, A. P., Greeley, L. A., Han, Q., Hendriks, P., Hernandez-Soriano, M. C., Li, M., Ng, J. L. P., Mau, L., Mesa-Marín, J., Miller, A. J., Rae, A. E., Schmidt, J., Thies, A., … Zheng, C. (2022). Root biology never sleeps. New Phytologist, 235(6), 2149–2154. https://doi.org/10.1111/nph.18338

Carolina, N. (2014). Erosion and Sediment Control Design and Construction Manual NCDOT.

Chauhan, C., Singh, M., Vinayak, A. B., & Uday, K. V. (2024). Quantification of the effectiveness of mitigation measures on erosion potential of soil with image analysis. Journal of Soils and Sediments, 24(1), 98–110. https://doi.org/10.1007/s11368-023-03598-5

Chen, Y., Teo, F. Y., Wong, S. Y., Chan, A., Weng, C., & Falconer, R. A. (2024). Monsoonal Extreme Rainfall in Southeast Asia: A Review. Water, 17(1), 5. https://doi.org/10.3390/w17010005

Chuenjaidee, S., Voottipruex, P., Jongpradist, P., Kalayasri, P., & Jamsawang, P. (2025a). Integrated performance of geocells and Ruzi grass for slope erosion control under variable rainfall and slope conditions. Journal of Soils and Sediments, 25(3), 732–750. https://doi.org/10.1007/s11368-025-03966-3

Chen, F., Zhang, J., Zhang, M., & Wang, J. (2015). Effect of Cynodon dactylon community on the conservation and reinforcement of riparian shallow soil in the Three Gorges Reservoir area. Ecological Processes, 4(1), 3. https://doi.org/10.1186/s13717-014-0029-2

Chen, Y., Qi, Y., Wei, Y., Ning, W., & He, B. (2024). Root traits and soil detachment in response to variable slope gradients in a representative purple-soil sloping grassland. CATENA, 239, 107936. https://doi.org/10.1016/j.catena.2024.107936

Cheng, P., Wu, L., Zhang, H., & Zhou, J. (2024b). Inclusion of root water absorption and reinforcement in upper bound limit stability analysis of vegetated slopes. Computers and Geotechnics, 169, 106227. https://doi.org/10.1016/j.compgeo.2024.106227

Chuenjaidee, S., Voottipruex, P., Jongpradist, P., Kalayasri, P., & Jamsawang, P. (2025). Integrated performance of geocells and Ruzi grass for slope erosion control under variable rainfall and slope conditions. Journal of Soils and Sediments, 25(3), 732–750. https://doi.org/10.1007/s11368-025-03966-3

Cohen, D., Schwarz, M., & Or, D. (2011). An analytical fiber bundle model for pullout mechanics of root bundles. Journal of Geophysical Research, 116(F3), F03010. https://doi.org/10.1029/2010JF001886

Costantini, A., & Loch, R. J. (2002). Effects of site preparation on runoff, erosion, and nutrient losses from Pinus plantations established on the coastal lowlands of south-east Queensland, Australia. Australian Journal of Soil Research, 40(8), 1287–1302. https://doi.org/10.1071/SR02032

Costantini, A., & Loch, R. J. (2002). Effects of site preparation on runoff, erosion, and nutrient losses from Pinus plantations established on the coastal lowlands of south-east Queensland, Australia. Australian Journal of Soil Research, 40(8), 1287–1302. https://doi.org/10.1071/SR02032

Couper, P., Stott, T., & Maddock, I. (2002). Insights into river bank erosion processes derived from analysis of negative erosion-pin recordings: observations from three recent UK studies. Earth Surface Processes and Landforms, 27(1), 59–79. https://doi.org/10.1002/esp.285

Cuomo, S., Della Sala, M., & Pierri, M. (2016). Experimental evidences and numerical modelling of runoff and soil erosion in flume tests. CATENA, 147, 61–70. https://doi.org/10.1016/j.catena.2016.06.044

Dai, Z.-C., Fu, W., Qi, S.-S., Zhai, D.-L., Chen, S.-C., Wan, L.-Y., Huang, P., & Du, D.-L. (2016). Different Responses of an Invasive Clonal Plant Wedelia trilobata and its Native Congener to Gibberellin: Implications for Biological Invasion. Journal of Chemical Ecology, 42(2), 85–94. https://doi.org/10.1007/s10886-016-0670-6

Dai, Z.-C., Kong, F.-L., Li, Y.-F., Ullah, R., Ali, E. A., Gul, F., Du, D.-L., Zhang, Y.-F., Jia, H., Qi, S.-S., Uddin, N., & Khan, I. U. (2024). Strong Invasive Mechanism of Wedelia trilobata via Growth and Physiological Traits under Nitrogen Stress Condition. Plants, 13(3), 355. https://doi.org/10.3390/plants13030355

Deng, L., Sun, T., Fei, K., Zhang, L., Fan, X., Wu, Y., & Ni, L. (2020). Effects of erosion degree, rainfall intensity and slope gradient on runoff and sediment yield for the bare soils from the weathered granite slopes of SE China. Geomorphology, 352, 106997. https://doi.org/10.1016/j.geomorph.2019.106997

Department of Highways, M. of T. K. of T. (2018). Standard drawing and drainage design guidebook.

Devienne-Barret, F., Richard-Molard, C., Chelle, M., Maury, O., & Ney, B. (2006). Ara-Rhizotron: An Effective Culture System to Study Simultaneously Root and

Shoot Development of Arabidopsis. Plant and Soil, 280(1–2), 253–266. https://doi.org/10.1007/s11104-005-3224-1

Duan, J., Liu, Y.-J., Wang, L.-Y., Yang, J., Tang, C.-J., & Zheng, H.-J. (2022). Importance of grass stolons in mitigating runoff and sediment yield under simulated rainstorms. CATENA, 213, 106132. https://doi.org/10.1016/j.catena.2022.106132

Dunkerley, D. L. (2019). Rainfall intensity bursts and the erosion of soils: an analysis highlighting the need for high temporal resolution rainfall data for research under current and future climates. Earth Surface Dynamics, 7(2), 345–360. https://doi.org/10.5194/esurf-7-345-2019

Dutilleul, P., & Lafond, J. A. (2016). Editorial: Branching and Rooting Out with a CT Scanner: The Why, the How, and the Outcomes, Present and Possibly Future. Frontiers in Plant Science, 7. https://doi.org/10.3389/fpls.2016.00041

Enesi, I., & Kuqi, A. (2022). Analyzing parameters in 3D reconstruction photogrammetry in Meshroom, a case study. 2022 11th Mediterranean Conference on Embedded Computing (MECO), 1–8. https://doi.org/10.1109/MECO55406.2022.9797170

Enyew, M., Geleta, M., Feyissa, T., Hammenhag, C., Tesfaye, K., Seyoum, A., & Carlsson, A. S. (2023). Sorghum genotypes grown in simple rhizotrons display wide variation in root system architecture traits. Plant and Soil. https://doi.org/10.1007/s11104-023-06373-0

Elhakeem, M., & Papanicolaou, A. N. (2009). Estimation of the runoff curve number via direct rainfall simulator measurements in the state of Iowa, USA. Water Resources Management, 23(12), 2455–2473. https://doi.org/10.1007/s11269-008-9390-1

Fan, C.-C., Chen, C.-H., & Chen, C. (2025). Exploring the Root–Soil Anchoring Dynamics of Bambusa pachinensis (Pachi Bamboo) Root System. Forests, 16(5), 832. https://doi.org/10.3390/f16050832

Fei, K., Deng, L., Sun, T., Zhang, L., Wu, Y., Fan, X., & Dong, Y. (2019). Runoff processes and lateral transport of soil total carbon induced by water erosion in the hilly region of southern China under rainstorm conditions. Geomorphology, 340, 143–152. https://doi.org/10.1016/j.geomorph.2019.05.006

Fernández-Raga, M., Rodríguez, I., Caldevilla, P., Búrdalo, G., Ortiz, A., & Martínez-García, R. (2022). Optimization of a Laboratory Rainfall Simulator to Be Representative of Natural Rainfall. Water, 14(23), 3831. https://doi.org/10.3390/w14233831

Fienberg, K., & Foufoula-Georgiou, E. (2009). HYDROLOGY Contents Atmospheric Water and Precipitation Evapotranspiration Fluvial Export Fluvial Transport of Suspended Solids Ground Water Ground Water and Surface Water Interaction Groundwater Chemistry Hydrological Cycle and Water Budgets Rivers Snow and Ice Springs Streams Vadose Water Wetland Hydrology Atmospheric Water and Precipitation.

Flavel, R. J., Guppy, C. N., Tighe, M., Watt, M., McNeill, A., & Young, I. M. (2012). Non-destructive quantification of cereal roots in soil using high-resolution X-ray tomography. Journal of Experimental Botany, 63(7), 2503–2511. https://doi.org/10.1093/jxb/err421

French, A., Ubeda-Tomás, S., Holman, T. J., Bennett, M. J., & Pridmore, T. (2009). High-Throughput Quantification of Root Growth Using a Novel Image-Analysis Tool. Plant Physiology, 150(4), 1784–1795. https://doi.org/10.1104/pp.109.140558

Fu, Y., Wang, D., Sun, W., & Guo, M. (2023). Impacts of grass planting density and components on overland flow hydraulics and soil loss. Land Degradation & Development, 34(1), 234–249. https://doi.org/10.1002/ldr.4456

Geißler, C., Kühn, P., Böhnke, M., Bruelheide, H., Shi, X., & Scholten, T. (2012). Splash erosion potential under tree canopies in subtropical SE China. Catena, 91, 85–93. https://doi.org/10.1016/j.catena.2010.10.009

Gentile, F., Elia, G., & Elia, R. (2010). Analysis of the stability of slopes reinforced by roots. 189–200. https://doi.org/10.2495/DN100171

Ghestem, M., Sidle, R. C., & Stokes, A. (2011). The Influence of Plant Root Systems on Subsurface Flow: Implications for Slope Stability. BioScience, 61(11), 869–879. https://doi.org/10.1525/bio.2011.61.11.6

Ghestem, M., Veylon, G., Bernard, A., Vanel, Q., & Stokes, A. (2014). Influence of plant root system morphology and architectural traits on soil shear resistance. Plant and Soil, 377(1–2), 43–61. https://doi.org/10.1007/s11104-012-1572-1

Gong, C., Ni, D., Liu, Y., Li, Y., Huang, Q., Tian, Y., & Zhang, H. (2024). Herbaceous Vegetation in Slope Stabilization: A Comparative Review of Mechanisms, Advantages, and Practical Applications. Sustainability, 16(17), 7620. https://doi.org/10.3390/su16177620

Goff, B. F., Bent, G. C., & Hart, G. E. (1993). Erosion Response of a Disturbed Sagebrush Steppe Hillslope. Journal of Environmental Quality, 22(4), 698–709. https://doi.org/10.2134/jeq1993.00472425002200040010x

Gonçalves, M. S., Ribeiro, W. R., Gonçalves, D. da C., Guerra Filho, P. A., Tanure, M. M. C., Amaral, J. F. T. do, Coser, A. C., Garcia, G. de O., Reis, E. F. dos, & Santos, A. R. dos. (2023). Tropical grasses adaptability as a sustainable tool for recovering degraded pastures and restricting soil loss: Use diagnosis and future scenarios. Environmental Development, 47, 100887. https://doi.org/10.1016/j.envdev.2023.100887

Gray, D. H., & Ohashi, H. (1983). Mechanics of Fiber Reinforcement in Sand. Journal of Geotechnical Engineering, 109(3), 335–353. https://doi.org/10.1061/(ASCE)0733-9410(1983)109:3(335)

Guo, H., Zhang, B., Hill, R. L., Wu, S., Dong, Q., Sun, L., & Zhang, K. (2019). Fish-scale pit effects on erosion and water runoff dynamics when positioned on a soil slope in the Loess Plateau region, China. Land Degradation and Development, 30(15), 1813–1827. https://doi.org/10.1002/ldr.3379

Guo, M., Shi, H., Zhao, J., Liu, P., Welbourne, D., & Lin, Q. (2016). Digital close range photogrammetry for the study of rill development at flume scale. CATENA, 143, 265–274. https://doi.org/10.1016/j.catena.2016.03.036

Han, Z., Yang, X., Yin, X., Fang, Q., & Zhao, L. (2023). Effect of exposed roots on the erosion characteristics of sloped land based on close-range photogrammetry in a karst rocky desertification region. Catena, 225. https://doi.org/10.1016/j.catena.2023.107035

Hao, H., Qin, J., Sun, Z., Guo, Z., & Wang, J. (2021). Erosion-reducing effects of plant roots during concentrated flow under contrasting textured soils. CATENA, 203, 105378. https://doi.org/10.1016/j.catena.2021.105378

Haubrock, S. N., Kuhnert, M., Chabrillat, S., Güntner, A., & Kaufmann, H. (2009). Spatiotemporal variations of soil surface roughness from in-situ laser scanning. Catena, 79(2), 128–139. https://doi.org/10.1016/j.catena.2009.06.005

He, W., Luo, C., Wang, Y., Wen, X., Wang, Y., Li, T., Chen, G., Zhao, K., Li, X., & Fan, C. (2022). Response Strategies of Root System Architecture to Soil Environment: A Case Study of Single-Species Cupressus funebris Plantations. Frontiers in Plant Science, 13. https://doi.org/10.3389/fpls.2022.822223

Helliwell, J. R., Sturrock, C. J., Miller, A. J., Whalley, W. R., & Mooney, S. J. (2019). The role of plant species and soil condition in the structural development of the rhizosphere. Plant, Cell & Environment, 42(6), 1974–1986. https://doi.org/10.1111/pce.13529

Himmelbauer, M. L., Loiskandl, ¡AFF1¿W., & Kastanek, ¡AFF1¿F. (2004). Estimating length, average diameter and surface area of roots using two different Image

analyses systems. Plant and Soil, 260(1/2), 111–120. https://doi.org/10.1023/B:PLSO.0000030171.28821.55

Hossain, A., Ishimine, Y., Motomura, K., & Akamine, H. (2005). Effects of Planting Pattern and Planting Distance on Growth and Yield of Turmeric (Curcuma longa L.). Plant Production Science, 8(1), 95–105. https://doi.org/10.1626/pps.8.95

Hu, J., Wang, B., Bai, L., Li, Y., Zhang, X., Liu, J., & Zhao, C. (2024). Quantifying the contribution of shrub roots to soil mechanical reinforcement using in situ shearing and assessing model reliability in coal mine subsidence areas, China. CATENA, 246, 108459. https://doi.org/10.1016/j.catena.2024.108459

Javed, S., Chai, X., Wang, X., & Xu, S. (2024). The phytohormones underlying the plant lateral root development in fluctuated soil environments. Plant and Soil, 505(1–2), 101–114. https://doi.org/10.1007/s11104-023-06326-7

Jester, W., & Klik, A. (2005). Soil surface roughness measurement—methods, applicability, and surface representation. CATENA, 64(2–3), 174–192. https://doi.org/10.1016/j.catena.2005.08.005

J E Gilley. (2005). Erosion / Water Induced. USDA Agricultural Research Service, Lincoln, NE, USA, 463–469.

Jiang, Y., Shi, H., Guo, M., Zhao, J., Cao, X., Shui, J., & Paull, D. (2023). A digital close range photogrammetric observation system for measuring soil surface morphology during ongoing rainfall. Journal of Hydrology, 620, 129427. https://doi.org/10.1016/j.jhydrol.2023.129427

Jie, C., Jing-zhang, C., Man-zhi, T., & Zi-tong, G. (2002). Soil degradation: a global problem endangering sustainable development. Journal of Geographical Sciences, 12(2), 243–252. https://doi.org/10.1007/BF02837480

Jia, Z., Liu, Y., Gruber, B. D., Neumann, K., Kilian, B., Graner, A., & von Wirén, N. (2019). Genetic Dissection of Root System Architectural Traits in Spring Barley. Frontiers in Plant Science, 10. https://doi.org/10.3389/fpls.2019.00400

Jian, S., Niu, Y., Zhang, X., Wei, Y., & Gao, J. (2024a). Study on Shear Strength of Soil–Root Systems of Different Vegetation Types. Plants, 13(21), 2963. https://doi.org/10.3390/plants13212963

Jian, S., Niu, Y., Zhang, X., Wei, Y., & Gao, J. (2024b). Study on Shear Strength of Soil–Root Systems of Different Vegetation Types. Plants, 13(21), 2963. https://doi.org/10.3390/plants13212963

Jin, X., Zhu, J., Wei, X., Xiao, Q., Xiao, J., Jiang, L., Xu, D., Shen, C., Liu, J., & He, Z. (2024). Adaptation Strategies of Seedling Root Response to Nitrogen and Phosphorus Addition. Plants, 13(4). https://doi.org/10.3390/plants13040536

Kagabo, D. M., Stroosnijder, L., Visser, S. M., & Moore, D. (2013a). Soil erosion, soil fertility and crop yield on slow-forming terraces in the highlands of Buberuka, Rwanda. Soil and Tillage Research, 128, 23–29. https://doi.org/10.1016/j.still.2012.11.002

Kagabo, D. M., Stroosnijder, L., Visser, S. M., & Moore, D. (2013b). Soil erosion, soil fertility and crop yield on slow-forming terraces in the highlands of Buberuka, Rwanda. Soil and Tillage Research, 128, 23–29. https://doi.org/10.1016/j.still.2012.11.002

Kuhn, N. J., & Bryan, R. B. (2004). Drying, soil surface condition and interrill erosion on two Ontario soils. CATENA, 57(2), 113–133. https://doi.org/10.1016/j.catena.2003.11.001

Lann, T., Bao, H., Lan, H., Zheng, H., Yan, C., & Peng, J. (2024). Hydro-mechanical effects of vegetation on slope stability: A review. Science of The Total Environment, 926, 171691. https://doi.org/10.1016/j.scitotenv.2024.171691

Lees, C., de Baets, S., Rickson, J., & Simmons, R. W. (2021). Selecting plant traits for soil erosion control in grassed waterways under a changing climate: A growth room study. European Journal of Soil Science, 72(6), 2381–2397. https://doi.org/10.1111/ejss.13045

Leung, A. K., Boldrin, D., Liang, T., Wu, Z. Y., Kamchoom, V., & Bengough, A. G. (2017). Plant age effects on soil infiltration rate during early plant establishment. Géotechnique, 1–7. https://doi.org/10.1680/jgeot.17.T.037

Leung, A. K., Garg, A., Coo, J. L., Ng, C. W. W., & Hau, B. C. H. (2015). Effects of the roots of Cynodon dactylon and Schefflera heptaphylla on water infiltration rate and soil hydraulic conductivity. Hydrological Processes, 29(15), 3342–3354. https://doi.org/10.1002/hyp.10452

Lhamo, D., & Luan, S. (2021). Potential Networks of Nitrogen-Phosphorus-Potassium Channels and Transporters in Arabidopsis Roots at a Single Cell Resolution. Frontiers in Plant Science, 12, 689545. https://doi.org/10.3389/FPLS.2021.689545

Li, C., Monno, Y., & Okutomi, M. (2022). Pro-Cam SSfM: projector–camera system for structure and spectral reflectance from motion. The Visual Computer. https://doi.org/10.1007/s00371-022-02434-0

Li, P., & Li, Z. (2011). Soil reinforcement by a root system and its effects on sediment yield in response to concentrated flow in the loess plateau. Agricultural Sciences, 02(02), 86–93. https://doi.org/10.4236/as.2011.22013

Liu, H., Yao, L., Lin, C., Wang, X., Xu, W., & Wang, H. (2018). 18-year grass hedge effect on soil water loss and soil productivity on sloping cropland. Soil and Tillage Research, 177, 12–18. https://doi.org/10.1016/j.still.2017.11.007

Liu, Y., Mu, X., Wang, H., & Yan, G. (2012). A novel method for extracting green fractional vegetation cover from digital images. Journal of Vegetation Science, 23(3), 406–418. https://doi.org/10.1111/j.1654-1103.2011.01373.x

Li, Z., Wang, M., Yu, S., & Liu, J. (2024). Effects of the Root's Distribution on the Stability of Slope. Geotechnical and Geological Engineering, 42(2), 1009–1019. https://doi.org/10.1007/s10706-023-02601-7

Lv, J., Xie, Y., & Luo, H. (2020). Erosion Process and Temporal Variations in the Soil Surface Roughness of Spoil Heaps under Multi-Day Rainfall Simulation. Remote Sensing, 12(14), 2192. https://doi.org/10.3390/rs12142192

Likitlersuang, S., Phan, T. N., Boldrin, D., & Leung, A. K. (2022a). Influence of growth media on the biomechanical properties of the fibrous roots of two contrasting vetiver grass species. Ecological Engineering, 178, 106574. https://doi.org/10.1016/j.ecoleng.2022.106574

Likitlersuang, S., Phan, T. N., Boldrin, D., & Leung, A. K. (2022b). Influence of growth media on the biomechanical properties of the fibrous roots of two contrasting vetiver grass species. Ecological Engineering, 178, 106574. https://doi.org/10.1016/j.ecoleng.2022.106574

Lv, J., Wang, W., Dai, T., Liu, B., & Liu, G. (2024a). Experimental Study on the Effect of Soil Reinforcement and Slip Resistance on Shallow Slopes

Lynch, J. P., Strock, C. F., Schneider, H. M., Sidhu, J. S., Ajmera, I., Galindo-Castañeda, T., Klein, S. P., & Hanlon, M. T. (2021). Root anatomy and soil resource capture. Plant and Soil, 466(1–2), 21–63. https://doi.org/10.1007/s11104-021-05010-y

Maadi, R., & Noorzad, A. (2024). Effect of root age on the slope stability using vetiver grass. Arabian Journal of Geosciences, 17(7), 217. https://doi.org/10.1007/s12517-024-12020-4

Maan, C., ten Veldhuis, M.-C., & van de Wiel, B. J. H. (2023). Dynamic root growth in response to depth-varying soil moisture availability: a rhizobox study. Hydrology and Earth System Sciences, 27(12), 2341–2355. https://doi.org/10.5194/hess-27-2341-2023

Mandal, D., Srivastava, P., Giri, N., Kaushal, R., Cerda, A., & Alam, N. M. (2017). Reversing land degradation through grasses: a systematic meta-analysis in the Indian tropics. Solid Earth, 8(1), 217–233. https://doi.org/10.5194/se-8-217-2017

Martinez-Mena, M., Rogel, J. A., Albaladejo, J., & Castillo, V. M. (2000). Influence of vegetal cover on sediment particle size distribution in natural rainfall conditions in a semiarid environment. CATENA, 38(3), 175–190. https://doi.org/10.1016/S0341-8162(99)00073-9

Mei, Y.-H., Li, X., Zhou, J.-Y., Kong, F.-L., Qi, S.-S., Zhu, B., Naz, M., Dai, Z.-C., & Du, D.-L. (2022). Both Adaptability and Endophytic Bacteria Are Linked to the Functional Traits in the Invasive Clonal Plant Wedelia trilobata. Plants, 11(23), 3369. https://doi.org/10.3390/plants11233369

Meijer, G. J., Bengough, A. G., Knappett, J. A., Loades, K. W., & Nicoll, B. C. (2018). In situ measurement of root reinforcement using corkscrew extraction method. Canadian Geotechnical Journal, 55(10), 1372–1390. https://doi.org/10.1139/cgj-2017-0344

Meijer, G. J., Lynch, J. P., Chimungu, J. G., & Loades, K. W. (2024). Root anatomy and biomechanical properties: improving predictions through root cortical and stele properties. Plant and Soil, 500(1–2), 587–603. https://doi.org/10.1007/s11104-024-06507-y

Moresi, F. V., Maesano, M., Matteucci, G., Romagnoli, M., Sidle, R. C., & Scarascia Mugnozza, G. (2019). Root Biomechanical Traits in a Montane Mediterranean Forest Watershed: Variations with Species Diversity and Soil Depth. Forests, 10(4), 341. https://doi.org/10.3390/f10040341

Nahar, K., & Pan, W. L. (2019). High resolution in situ rhizosphere imaging of root growth dynamics in oilseed castor plant (Ricinus communis L.) using digital scanners. Modeling Earth Systems and Environment, 5(3), 781–792. https://doi.org/10.1007/s40808-018-0564-4

Nearing, M. A., Jetten, V., Baffaut, C., Cerdan, O., Couturier, A., Hernandez, M., Bissonnais, Y. Le, Nichols, M. H., Nunes, J. P., Renschler, C. S., Souchere, V., & van Oost, K. (2005). Modeling Response of Soil Erosion and Runoff to Changes in Precipitation and Cover. Impacts of Global Climate Change, 1–11. https://doi.org/10.1061/40792(173)482

Neller, R. J. (1988). A comparison of channel erosion in small urban and rural catchments, Armidale, New South Wales. Earth Surface Processes and Landforms, 13(1), 1–7. https://doi.org/10.1002/esp.3290130102

Neufeld, H. S., Durall, D. M., Rich, P. M., & Tingey, D. T. (1989). A rootbox for quantitative observations on intact entire root systems. Plant and Soil, 117(2), 295–298. https://doi.org/10.1007/BF02220725

Ng, C. W. W., & Zhan, L. T. (2007). Comparative Study of Rainfall Infiltration into a Bare and a Grassed Unsaturated Expansive Soil Slope. Soils and Foundations, 47(2), 207–217. https://doi.org/10.3208/sandf.47.207

Nguyen, T. S., Likitlersuang, S., & Jotisankasa, A. (2019). Influence of the spatial variability of the root cohesion on a slope-scale stability model: a case study of residual soil slope in Thailand. Bulletin of Engineering Geology and the Environment, 78(5), 3337–3351. https://doi.org/10.1007/s10064-018-1380-9

Olinic, T., Olinic, E.-D., & Butcaru, A.-C. (2024). Integrating Geosynthetics and Vegetation for Sustainable Erosion Control Applications. Sustainability, 16(23), 10621. https://doi.org/10.3390/su162310621

Papadaki, H., Robson, S., Chapman, D. P., & Woodhouse, N. G. (2000). <title>Toward the automated extraction of accurate 3D models from close-range photogrammetric networks</title> (S. F. El-Hakim & A. Gruen, Eds.; pp. 267–277). https://doi.org/10.1117/12.410882

Patidar, P., Sannagoudar, M. S., Ghosh, A., Singh, A. K., Misra, S., Khandibagur, V., Ojha, D., Casini, R., Elansary, H. O., & Chandra, A. (2023). Tropical range grasses can sustain soil functions despite nutrient depletion in semiarid degraded land. Frontiers in Sustainable Food Systems, 7. https://doi.org/10.3389/fsufs.2023.1230156

Phan, T. N., & Likitlersuang, S. (2024). Root system architecture of two vetiver species for root reinforcement modelling. Modeling Earth Systems and Environment, 10(1), 233–241. https://doi.org/10.1007/s40808-023-01772-9

Phan, T. N., Likitlersuang, S., Kamchoom, V., & Leung, A. K. (2021). Root biomechanical properties of Chrysopogon zizanioides and Chrysopogon nemoralis for soil reinforcement and slope stabilisation. Land Degradation and Development, 32(16), 4624–4636. https://doi.org/10.1002/ldr.4063

Phan, T. N., Leung, A. K., Kamchoom, V., & Likitlersuang, S. (2023). Reinforcement losses in soil stabilisation due to decomposing roots of Chrysopogon zizanioides and Chrysopogon nemoralis. Land Degradation & Development, 34(4), 1080–1096. https://doi.org/10.1002/ldr.4517

Phan, T. N., Leung, A. K., Nguyen, T. S., Kamchoom, V., & Likitlersuang, S. (2025). Modelling root decomposition effects on root reinforcement and slope stability.

Computers and Geotechnics, 179, 107024. https://doi.org/10.1016/j.compgeo.2024.107024

Phan, T. N., & Likitlersuang, S. (2024). Root system architecture of two vetiver species for root reinforcement modelling. Modeling Earth Systems and Environment, 10(1), 233–241. https://doi.org/10.1007/s40808-023-01772-9

Phan, T. N., Likitlersuang, S., Kamchoom, V., & Leung, A. K. (2021). Root biomechanical properties of Chrysopogon zizanioides and Chrysopogon nemoralis for soil reinforcement and slope stabilisation. Land Degradation and Development, 32(16), 4624–4636. https://doi.org/10.1002/ldr.4063

Piñeros, M. A., Larson, B. G., Shaff, J. E., Schneider, D. J., Falcão, A. X., Yuan, L., Clark, R. T., Craft, E. J., Davis, T. W., Pradier, P., Shaw, N. M., Assaranurak, I., McCouch, S. R., Sturrock, C., Bennett, M., & Kochian, L. V. (2016). Evolving technologies for growing, imaging and analyzing 3D root system architecture of crop plants. Journal of Integrative Plant Biology, 58(3), 230–241. https://doi.org/10.1111/jipb.12456

Preti, F. (2013). Forest protection and protection forest: Tree root degradation over hydrological shallow landslides triggering. Ecological Engineering, 61, 633–645. https://doi.org/10.1016/j.ecoleng.2012.11.009

Qin, Z., Zhang, J., DiTommaso, A., Wang, R., & Wu, R. (2015). Predicting invasions of Wedelia trilobata (L.) Hitchc. with Maxent and GARP models. Journal of Plant Research, 128(5), 763–775. https://doi.org/10.1007/s10265-015-0738-3

Quan, X., He, J., Cai, Q., Sun, L., Li, X., & Wang, S. (2020). Soil erosion and deposition characteristics of slope surfaces for two loess soils using indoor simulated rainfall experiment. Soil and Tillage Research, 204. https://doi.org/10.1016/j.still.2020.104714

Ruan, S., Tang, L., & Huang, T. (2022). The Pullout Mechanical Properties of Shrub Root Systems in a Typical Karst Area, Southwest China. Sustainability, 14(6), 3297. https://doi.org/10.3390/su14063297

Saadati, N., Mosaddeghi, M. R., Sabzalian, M. R., & Jafari, M. (2023). Soil mechanical reinforcement by the fibrous roots of selected rangeland plants using a large soil-root shear apparatus. Soil and Tillage Research, 234, 105852. https://doi.org/10.1016/j.still.2023.105852

Sami, M. A., Tayyab, M., Parikh, P., Govindaraju, H., & Hassan, U. (2021). A modular microscopic smartphone attachment for imaging and quantification of multiple fluorescent probes using machine learning. The Analyst, 146(8), 2531–2541. https://doi.org/10.1039/D0AN02451A

Schwarz, M., Cohen, D., & Or, D. (2010). Root-soil mechanical interactions during pullout and failure of root bundles. Journal of Geophysical Research: Earth Surface, 115(F4). https://doi.org/10.1029/2009JF001603

Schwarz, M., Giadrossich, F., & Cohen, D. (2013). Modeling root reinforcement using a root-failure Weibull survival function. Hydrology and Earth System Sciences, 17(11), 4367–4377. https://doi.org/10.5194/hess-17-4367-2013

Semwal, T., & Uday, K. V. (2022). Multi-dimensional Measurement-Based Approaches for Evaluating the Root Area Ratio of Plant Species. International Journal of Geosynthetics and Ground Engineering, 8(1), 15. https://doi.org/10.1007/s40891-022-00357-3

Shi, P., Arter, C., Liu, X., Keller, M., & Schulin, R. (2017). Soil aggregate stability and size-selective sediment transport with surface runoff as affected by organic residue amendment. Science of the Total Environment, 607–608, 95–102. https://doi.org/10.1016/j.scitotenv.2017.07.008

Shao, H., Xia, T., Wu, D., Chen, F., & Mi, G. (2018). Root growth and root system architecture of field-grown maize in response to high planting density. Plant and Soil, 430(1–2), 395–411. https://doi.org/10.1007/s11104-018-3720-8

Si, H., Qiu, J., & Li, Y. (2022). A Review of Point Cloud Registration Algorithms for Laser Scanners: Applications in Large-Scale Aircraft Measurement. Applied Sciences, 12(20), 10247. https://doi.org/10.3390/app122010247

Singh, K., Gupta, S., & Singh, A. P. (2024). Review: Nutrient-nutrient interactions governing underground plant adaptation strategies in a heterogeneous environment. In Plant Science (Vol. 342). Elsevier Ireland Ltd. https://doi.org/10.1016/j.plantsci.2024.112024

Silvestri, N., Pistocchi, C., & Antichi, D. (2017). Soil and Nutrient Losses in a Flat Land-Reclamation District of Central Italy. Land Degradation & Development, 28(2), 638–647. https://doi.org/10.1002/ldr.2549

Sirmacek, B., & Lindenbergh, R. (2014). Accuracy assessment of building point clouds automatically generated from iphone images. The International Archives of the Photogrammetry, Remote Sensing and Spatial Information Sciences, XL–5, 547–552. https://doi.org/10.5194/isprsarchives-XL-5-547-2014

Song, C., Sang, J., Zhang, L., Liu, H., Wu, D., Yuan, W., & Huang, C. (2022). Adaptiveness of RGB-image derived algorithms in the measurement of fractional vegetation coverage. BMC Bioinformatics, 23(1), 358. https://doi.org/10.1186/s12859-022-04886-6

Stokes, A., Atger, C., Bengough, A. G., Fourcaud, T., & Sidle, R. C. (2009). Desirable plant root traits for protecting natural and engineered slopes against landslides. Plant and Soil, 324(1–2), 1–30. https://doi.org/10.1007/s11104-009-0159-y

Su, Y., Zhang, Y., Wang, H., & Zhang, T. (2022). Effects of vegetation spatial pattern on erosion and sediment particle sorting in the loess convex hillslope. Scientific Reports, 12(1), 14187. https://doi.org/10.1038/s41598-022-17975-6

Susaki, J., & Komiya, Y. (2014). Estimation of green space ratio for assessing urban landscapes using digital surface models and images. 2014 8th IAPR Workshop on Pattern Reconition in Remote Sensing, 1–4. https://doi.org/10.1109/PRRS.2014.6914284

Tayade, R., Kim, S.-H., Tripathi, P., Choi, Y.-D., Yoon, J.-B., & Kim, Y.-H. (2022). High-Throughput Root Imaging Analysis Reveals Wide Variation in Root Morphology of Wild Adzuki bean (Vigna angularis) Accessions. Plants, 11(3), 405. https://doi.org/10.3390/plants11030405

Tenten, N., Zeng, B., & Kazda, M. (2010). Soil stabilizing capability of three plant species growing on the Three Gorges Reservoir riverside. Journal of Earth Science, 21(6), 888–896. https://doi.org/10.1007/s12583-010-0142-9

Thanasisathit, N., Chuenjaidee, S., Voottipruex, P., Jongpradist, P., Kalayasri, P., & Jamsawang, P. (2025a). Field performance of erosion control on Lamtakong dam slopes using geocell and ruzi grass cover: A case study. Geotextiles and Geomembranes, 53(6), 1610–1622. https://doi.org/10.1016/j.geotexmem.2025.08.010

Thanasisathit, N., Chuenjaidee, S., Voottipruex, P., Jongpradist, P., Kalayasri, P., & Jamsawang, P. (2025b). Field performance of erosion control on Lamtakong dam slopes using geocell and ruzi grass cover: A case study. Geotextiles and Geomembranes, 53(6), 1610–1622. https://doi.org/10.1016/j.geotexmem.2025.08.010

Tran, T. V., Tucker-Kulesza, S. E., & Bernhardt-Barry, M. L. (2017). Determining Surface Roughness in Erosion Testing Using Digital Photogrammetry. Geotechnical Testing Journal, 40(6), 917–927. https://doi.org/10.1520/GTJ20160277

Uyar, N. (2025a). Index-Driven Soil Loss Mapping Across Environmental Scenarios: Insights from a Remote Sensing Approach. Sustainability, 17(17), 7913. https://doi.org/10.3390/su17177913

Uyar, N. (2025b). Index-Driven Soil Loss Mapping Across Environmental Scenarios: Insights from a Remote Sensing Approach. Sustainability, 17(17), 7913. https://doi.org/10.3390/su17177913

Walling, D. E. (1988). Erosion and sediment yield research — Some recent perspectives. Journal of Hydrology, 100(1–3), 113–141. https://doi.org/10.1016/0022-1694(88)90183-7

Wang, F., Tian, P., Guo, W., Chen, L., Gong, Y., & Ping, Y. (2024). Effects of rainfall patterns, vegetation cover types and antecedent soil moisture on run-off and soil loss of typical Luvisol in southern China. Earth Surface Processes and Landforms, 49(10), 2998–3012. https://doi.org/10.1002/esp.5871

Wang, H., Wang, F., Xue, R., She, X., Kong, W., & Huang, G. (2025). A Robust Feature-Matching Method for 3D Point Clouds via Spatial Encoding. Symmetry, 17(5), 640. https://doi.org/10.3390/sym17050640

Wang, Y.-C., & Lai, C.-C. (2018). Evaluating the Erosion Process from a Single-Stripe Laser-Scanned Topography: A Laboratory Case Study. Water, 10(7), 956. https://doi.org/10.3390/w10070956

Wang, S., Liu, X., Qi, H., Xu, Z., & Ma, Y. (2024). Determination of Biomechanical Parameters and Development of an Improved FEM Model for Perennial Alfalfa (Medicago sativa L.) Roots. Agronomy, 14(12), 3033. https://doi.org/10.3390/agronomy14123033

Wang, X., Li, Z., Chen, Y., & Yao, Y. (2023). Influence of Vetiver Root Morphology on Soil–Water Characteristics of Plant-Covered Slope Soil in South Central China. Sustainability, 15(2), 1365. https://doi.org/10.3390/su15021365

Wei, S., Zhang, K., Liu, C., Cen, Y., & Xia, J. (2024). Effects of different vegetation components on soil erosion and response to rainfall intensity under simulated rainfall. CATENA, 235, 107652. https://doi.org/10.1016/j.catena.2023.107652

Weihs, B. J., Heuschele, D.-J., Tang, Z., York, L. M., Zhang, Z., & Xu, Z. (2024). The State of the Art in Root System Architecture Image Analysis Using Artificial Intelligence: A Review. Plant Phenomics, 6, 0178. https://doi.org/10.34133/plantphenomics.0178

Woo, M., Fang, G., & diCenzo, P. D. (1997). The role of vegetation in the retardation of rill erosion. CATENA, 29(2), 145–159. https://doi.org/10.1016/S0341-8162(96)00052-5

Wu, T. H., McKinnell III, W. P., & Swanston, D. N. (1979). Strength of tree roots and landslides on Prince of Wales Island, Alaska. Canadian Geotechnical Journal, 16(1), 19–33. https://doi.org/10.1139/t79-003

Xu, Y., Guo, Y., Huang, Z., Liu, D., Huang, Q., & Tang, H. (2023). Study on Cynodon dactylon root system affecting dry–wet cracking behavior and shear strength

characteristics of expansive soil. Scientific Reports, 13(1), 13052. https://doi.org/10.1038/s41598-023-39770-7

Yin, Z., Chang, J., & Huang, Y. (2022). Multiscale Spatiotemporal Characteristics of Soil Erosion and Its Influencing Factors in the Yellow River Basin. Water, 14(17), 2658. https://doi.org/10.3390/w14172658

Yu, H., Han, C., Ren, G., Wu, X., Qi, S., Yang, B., Cui, M., Fan, X., Zhu, Z., Dai, Z., & Du, D. (2024). Heat Wave Adaptations: Unraveling the Competitive Dynamics Between Invasive Wedelia trilobata and Native Wedelia chinensis. Plants, 13(24), 3480. https://doi.org/10.3390/plants13243480

Zhang, C., Wang, J., & Jia, J. (2025). Characteristics of Hydrodynamic Parameters of Different Understory Vegetation Patterns. Plants, 14(16), 2556. https://doi.org/10.3390/plants14162556

Zhai, K., Zhang, J., Zhang, L., Luo, X., & Wang, K. (2024). Integrating Root Morphology Based on Whole-Pullout Test of Model Roots: A Case Study. Applied Sciences, 14(2), 764. https://doi.org/10.3390/app14020764

Zhang, C., Zhang, Q., Jiang, J., & Yang, Q. (2023). Pullout properties of Hippophae rhamnoides L. roots in the loess area. Archives of Agronomy and Soil Science, 69(11), 2170–2186. https://doi.org/10.1080/03650340.2022.2142570

Zhang, J., Wang, Y., Wang, P., Zhang, Q., Yan, C., Yu, F., Yi, J., & Fang, L. (2017). Effect of different levels of nitrogen, phosphorus, and potassium on root activity and chlorophyll content in leaves of Brassica oleracea seedlings grown in vegetable nursery substrate. Horticulture Environment and Biotechnology, 58(1), 5–11. https://doi.org/10.1007/s13580-017-0177-2

Zhang, X., Zhu, Q., Sang, J., & Ding, X. (2022). Effects of rainfall and the slope gradient on the soil and water loss in a purple soil area. Soil and Water Research, 17(4), 232–242. https://doi.org/10.17221/45/2022-SWR

Zhao, X., Li, T., Zhu, H., Wang, C., Yan, H., Song, L., Li, Y., & He, B. (2025). Hedgerow-grass ditch system effectively reduces sediment yield and nitrogen loss with surface runoff during simulated rainfall. International Soil and Water Conservation Research, 13(3), 644–655. https://doi.org/10.1016/j.iswcr.2025.03.006

Zhu, H., & Zhang, L. M. (2016). Field investigation of erosion resistance of common grass species for soil bioengineering in Hong Kong. Acta Geotechnica, 11(5), 1047–1059. https://doi.org/10.1007/s11440-015-0408-6

Zhu, P., Zhang, G., Zhang, B., & Wang, H. (2020). Variation in soil surface roughness under different land uses in a small watershed on the Loess Plateau, China. CATENA, 188, 104465. https://doi.org/10.1016/j.catena.2020.104465

Živanović, N., Rončević, V., Spasić, M., Ćorluka, S., & Polovina, S. (2022). Construction and calibration of a portable rain simulator designed for the in situ research of soil resistance to erosion. Soil and Water Research, 17(3), 158–169. https://doi.org/10.17221/148/2021-SWR

This is Mendeley biography

พระจอมเกล้าพระนครเหนือ มหาวิทยาลัยเทคโนโลยี

APPENDIX A

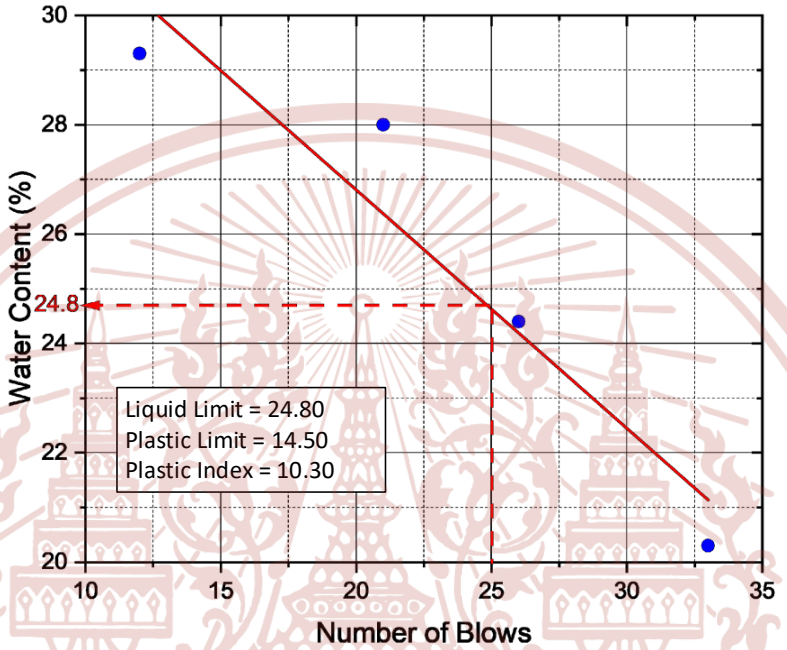


FIGURE A-1 Atterberg Limit Result

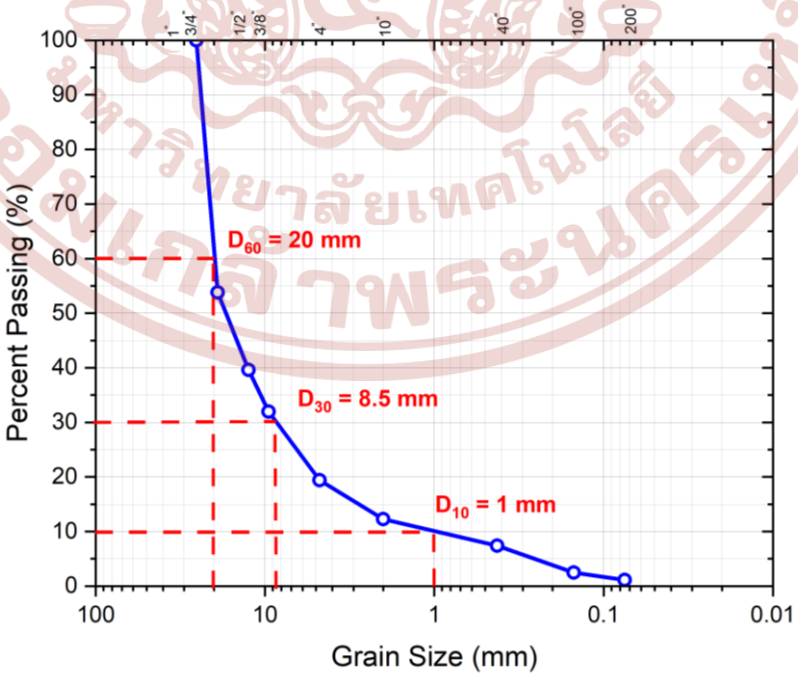


FIGURE A-2 Shows the particle size distribution

Table A-1 Criteria for testing soil modified compaction.

Specification	Method C
Dimension Mold	101.6 mm
Volume of Mold	941.5 cm^3
Hammer weight	2.5 kg
Hammer dropped	305 mm
Blows per layer	25
Layers	3
Energy	595 kJ/m^3
Soil	Passing sieve No. 4

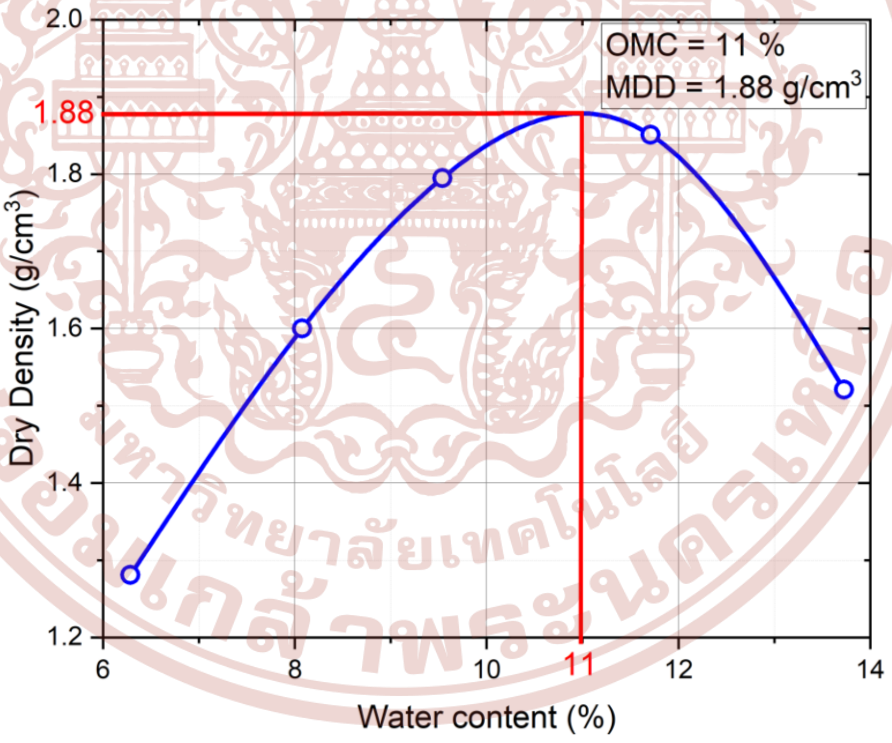


FIGURE A-3 Shows the Maximum dry density and Optimum moisture content

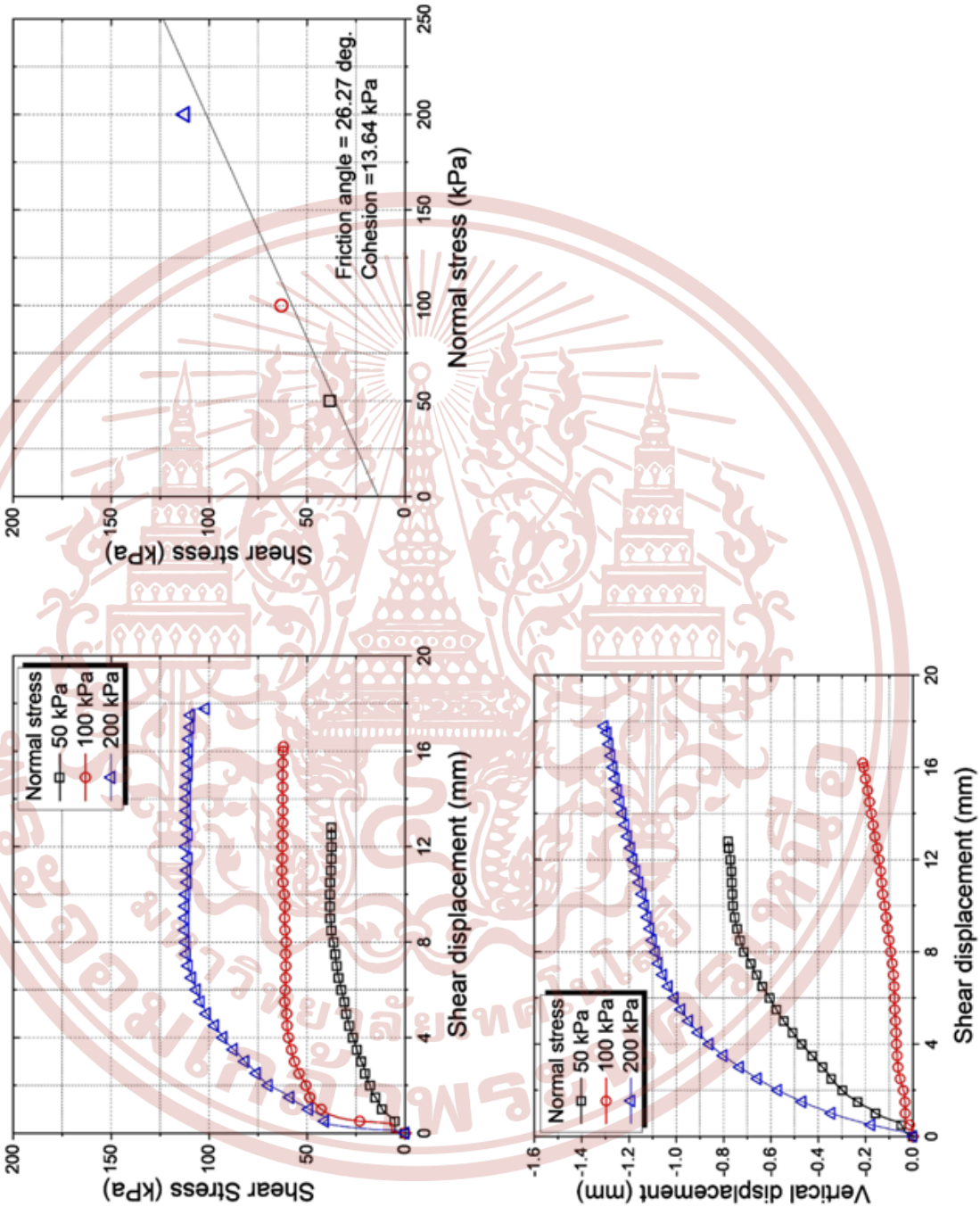


FIGURE A-4 Show Cohesion and internal friction angle

Table A-2 Soil Nutrient Results of Laterite soil and Rice husk ash

Element	Laterite soil			Rice husk ash		
	Weight %	Atomic %	Net Int.	Weight %	Atomic %	Net Int.
N K	1.0	1.4	0.9	1.6	2.2	2.6
P K	2.1	1.4	5.1	0.6	0.4	2.5
K K	2.0	1.1	4.1	0.9	0.5	3.0

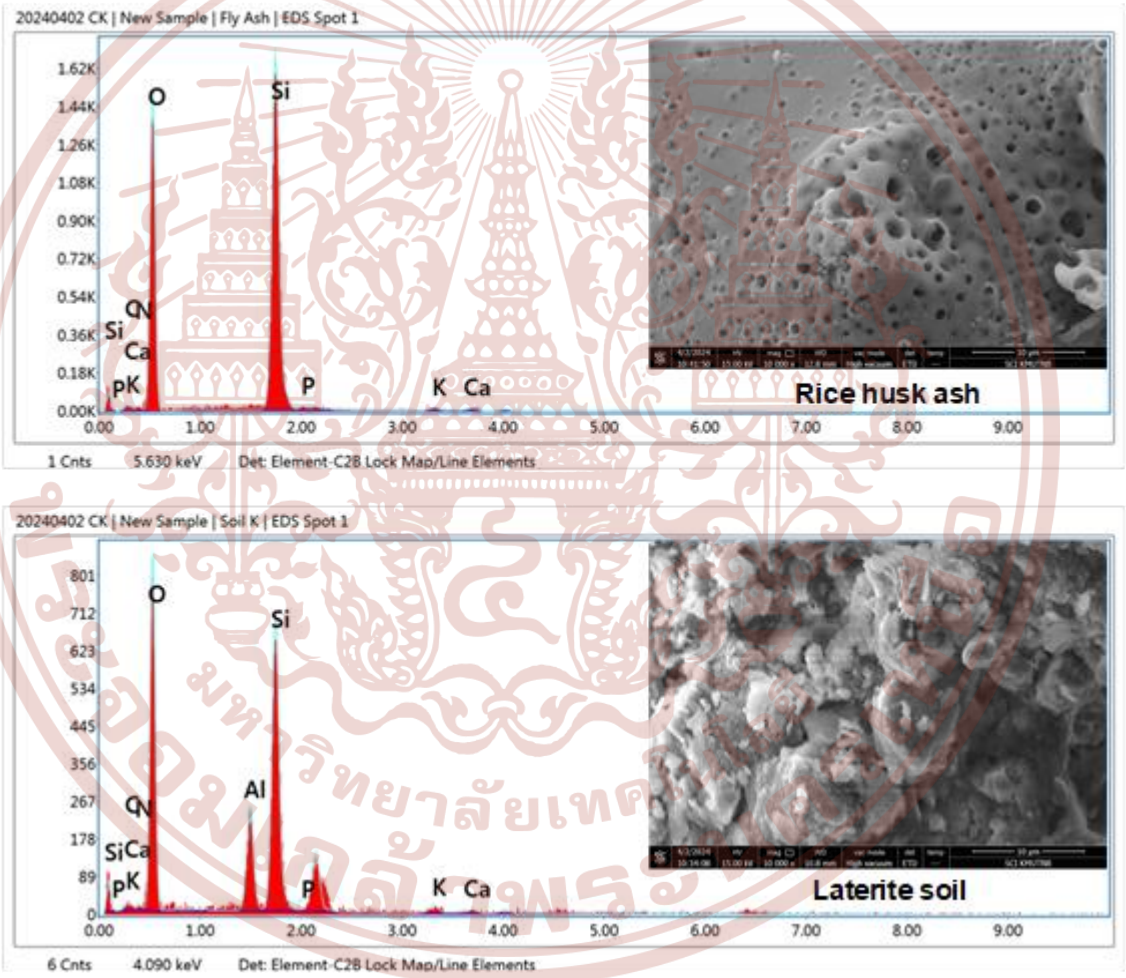


FIGURE A-5 SEM & EDX Result of Laterite soil and Rice husk ash

APPENDIX B

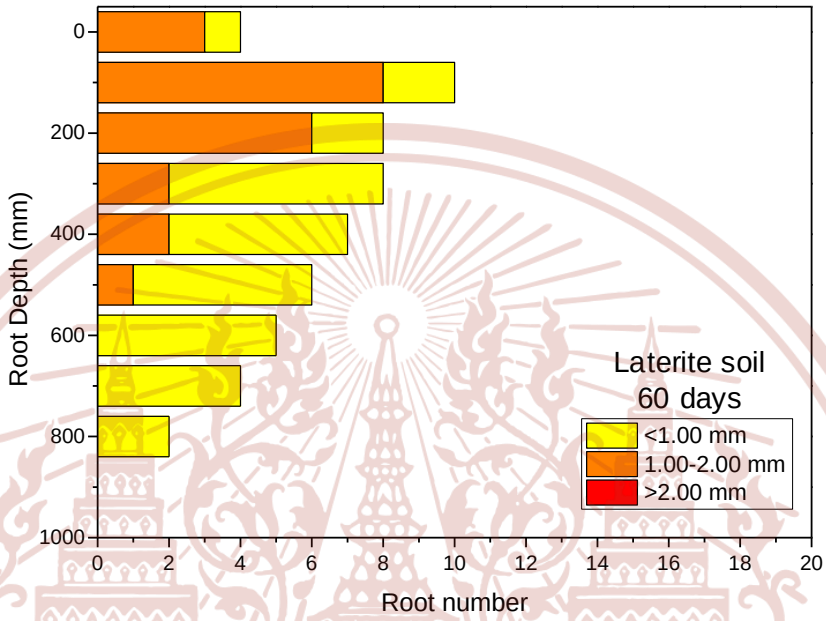


FIGURE B-1 Root diameter distribution of W.trilobata (Laterite soil 60 days)

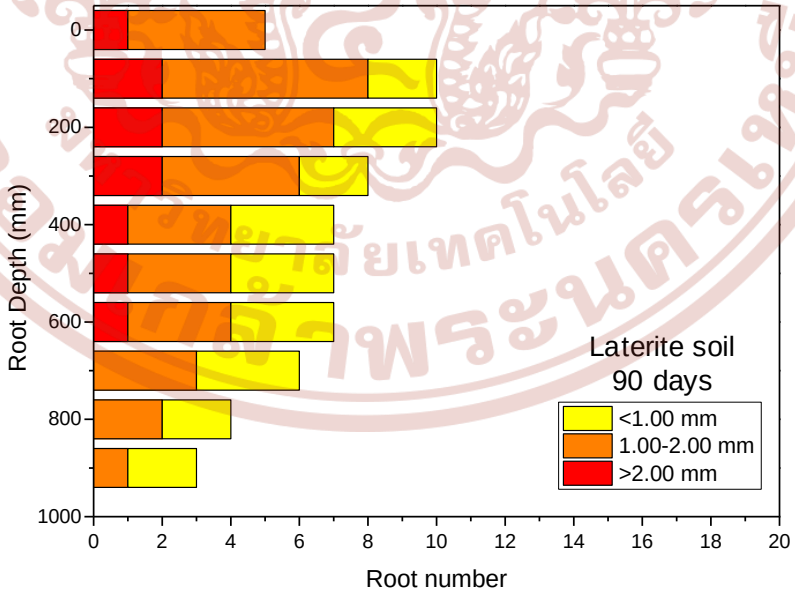


FIGURE B-2 Root diameter distribution of W.trilobata (Laterite soil 90 days)

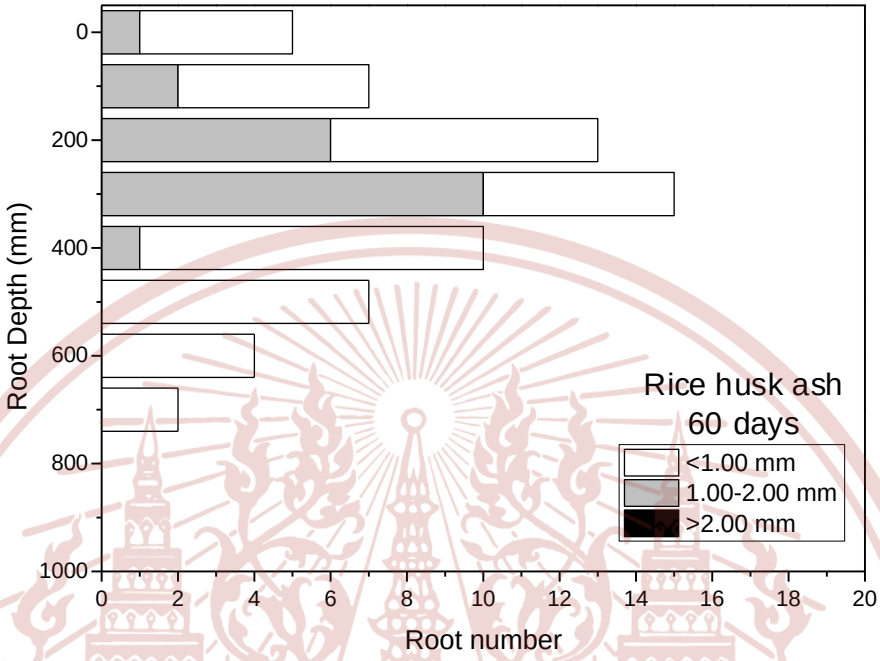


FIGURE B-3 Root diameter distribution of W.trilobata (Rice husk ash 60 days)

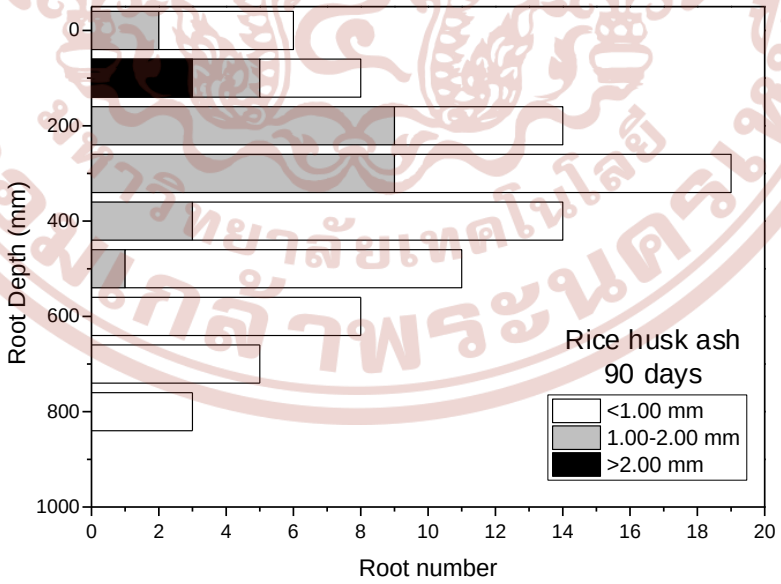


FIGURE B-4 Root diameter distribution of W.trilobata (Rice husk ash 60 days)

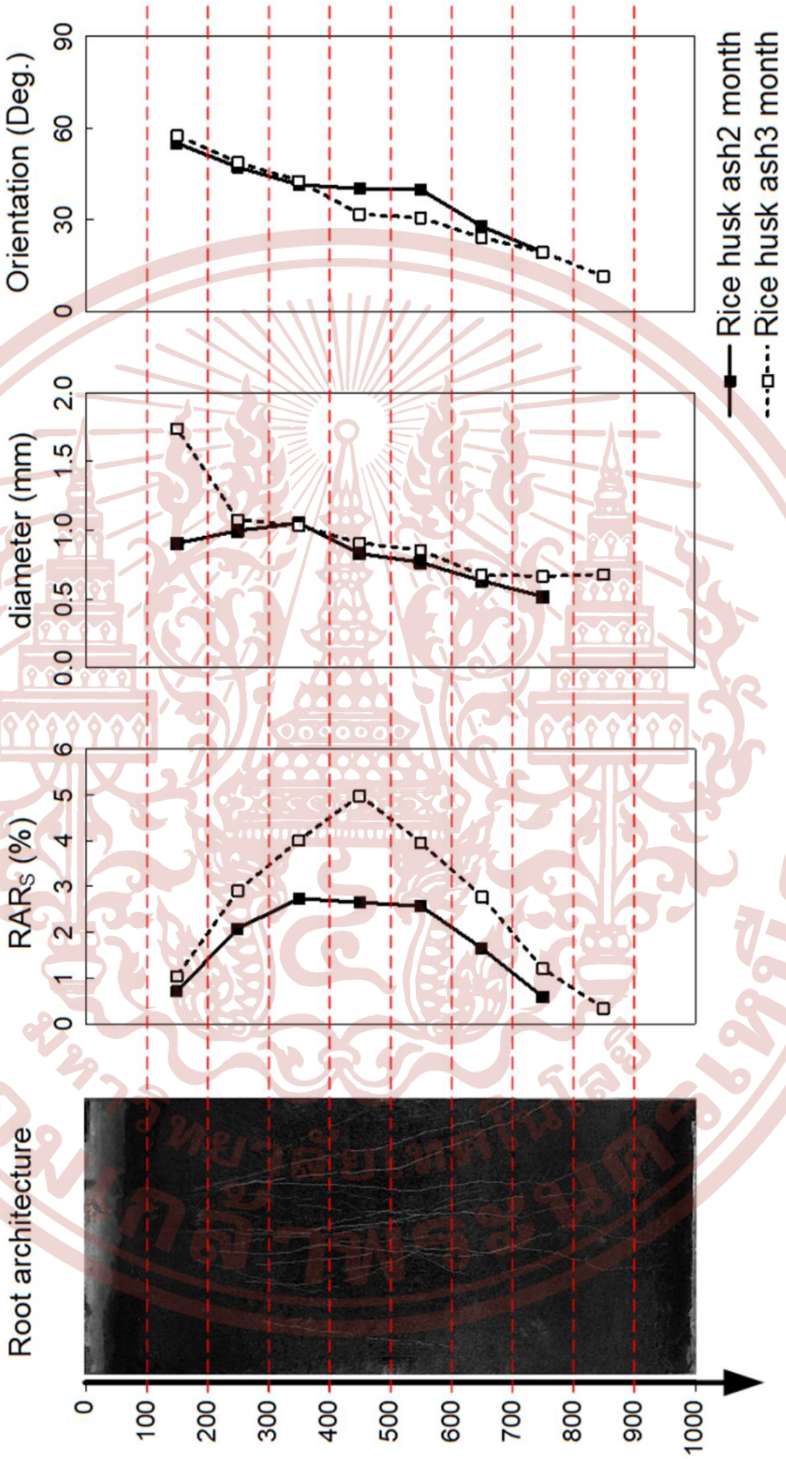


FIGURE B-5 Root architecture characteristics of W. trilobata grown in rice husk ash

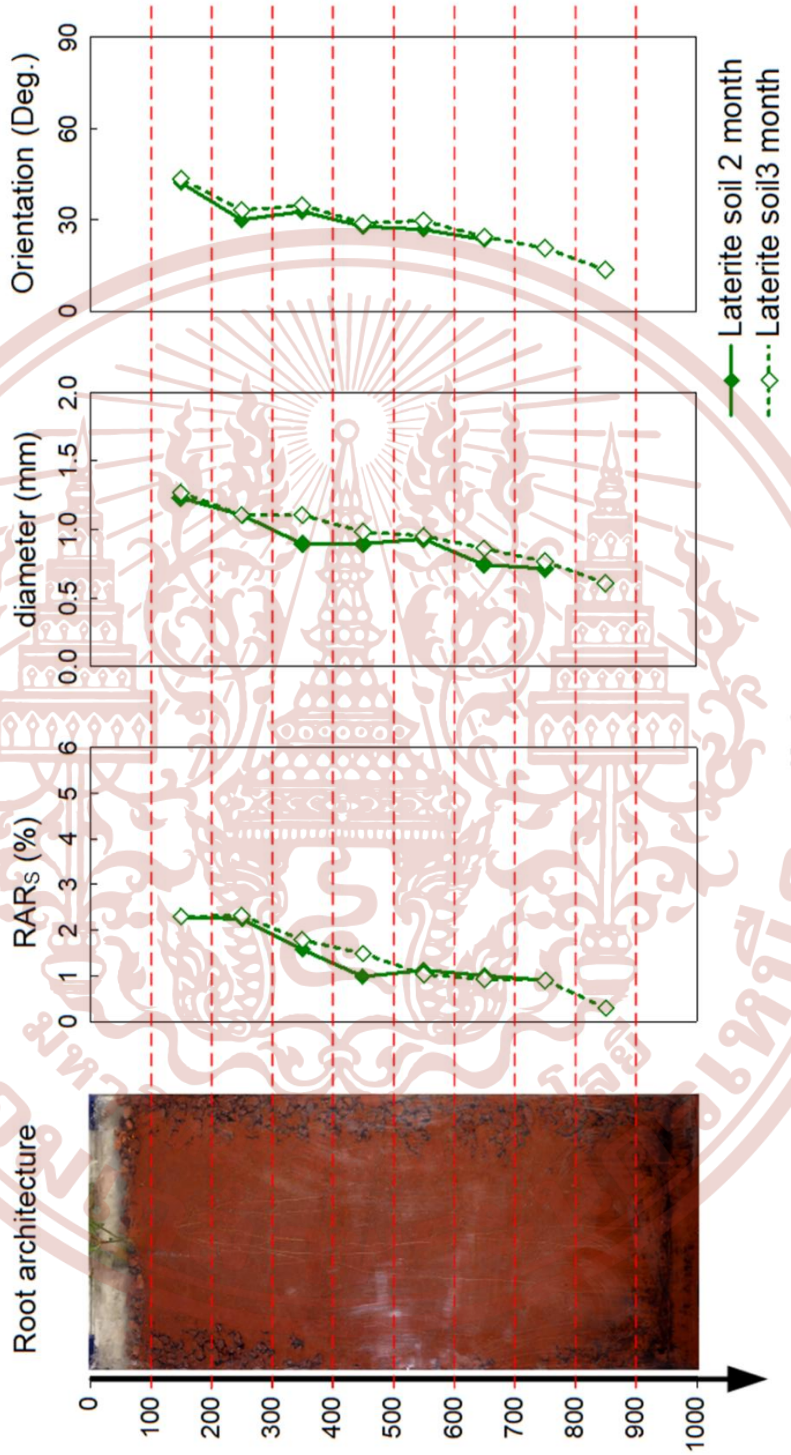


FIGURE B-6 Root architecture characteristics of W. trilobata grown in rice husk ash

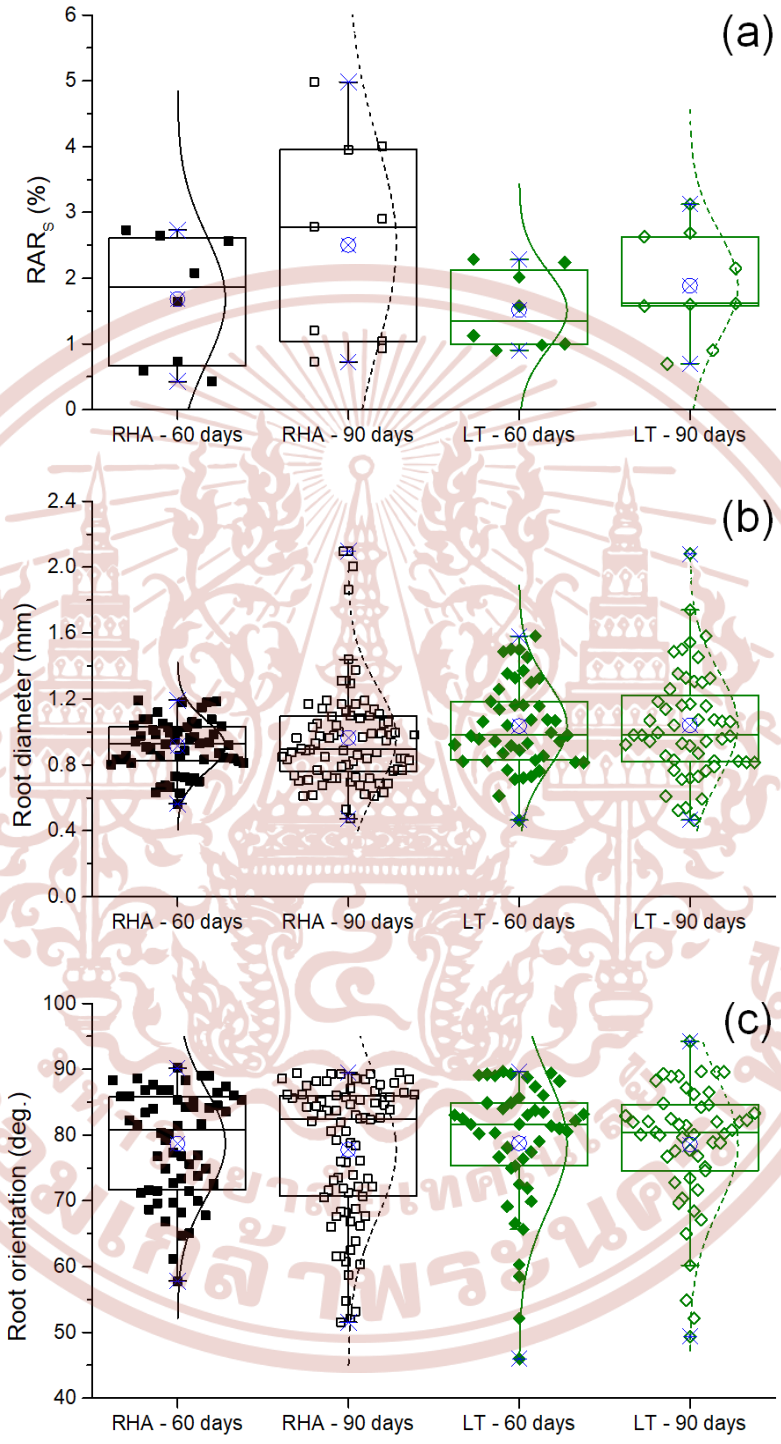


FIGURE B-7 Boxplots illustrating the distribution of root system parameters of W. trilobata grown in rice husk ash (RHA) and lateritic (LT) soils at 60 and 90 days of growth: (a) root area ratio (RAR_s), (b) root diameter, and (c) root orientation.

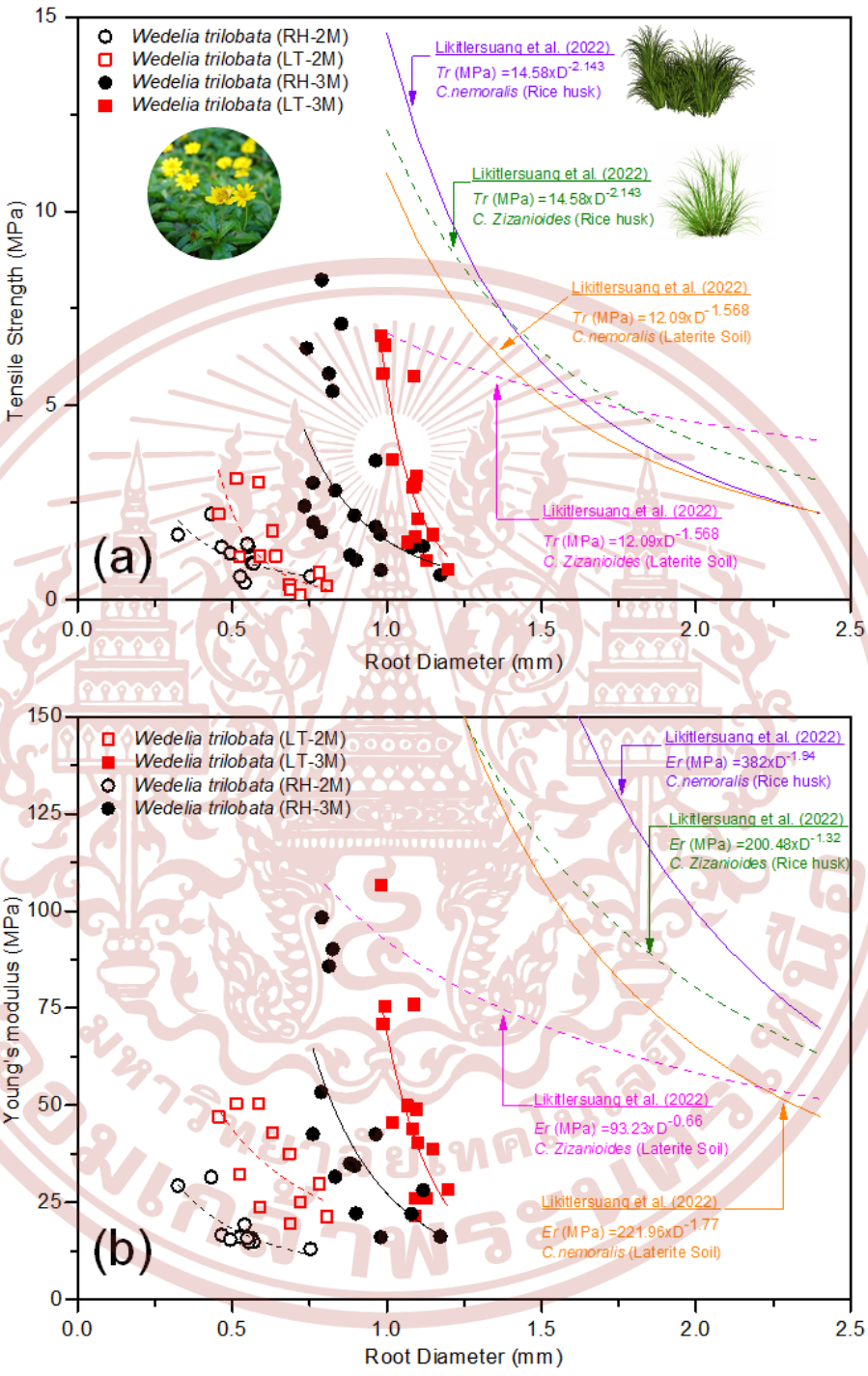


FIGURE B-8 Root biomechanical properties (a) correlation between tensile strength and root diameter (b) correlation between Young's modulus and root diameter.

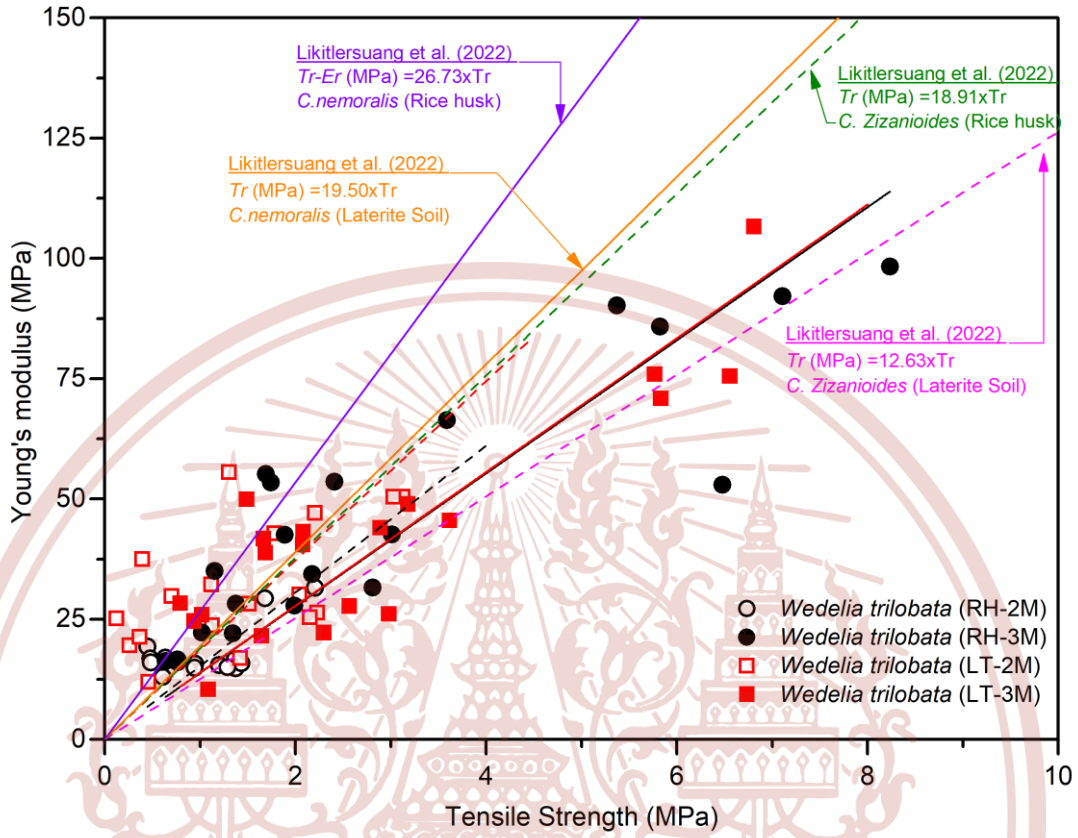


FIGURE B-9 Relation Tensile strength and Young's modulus of W. trilobata.

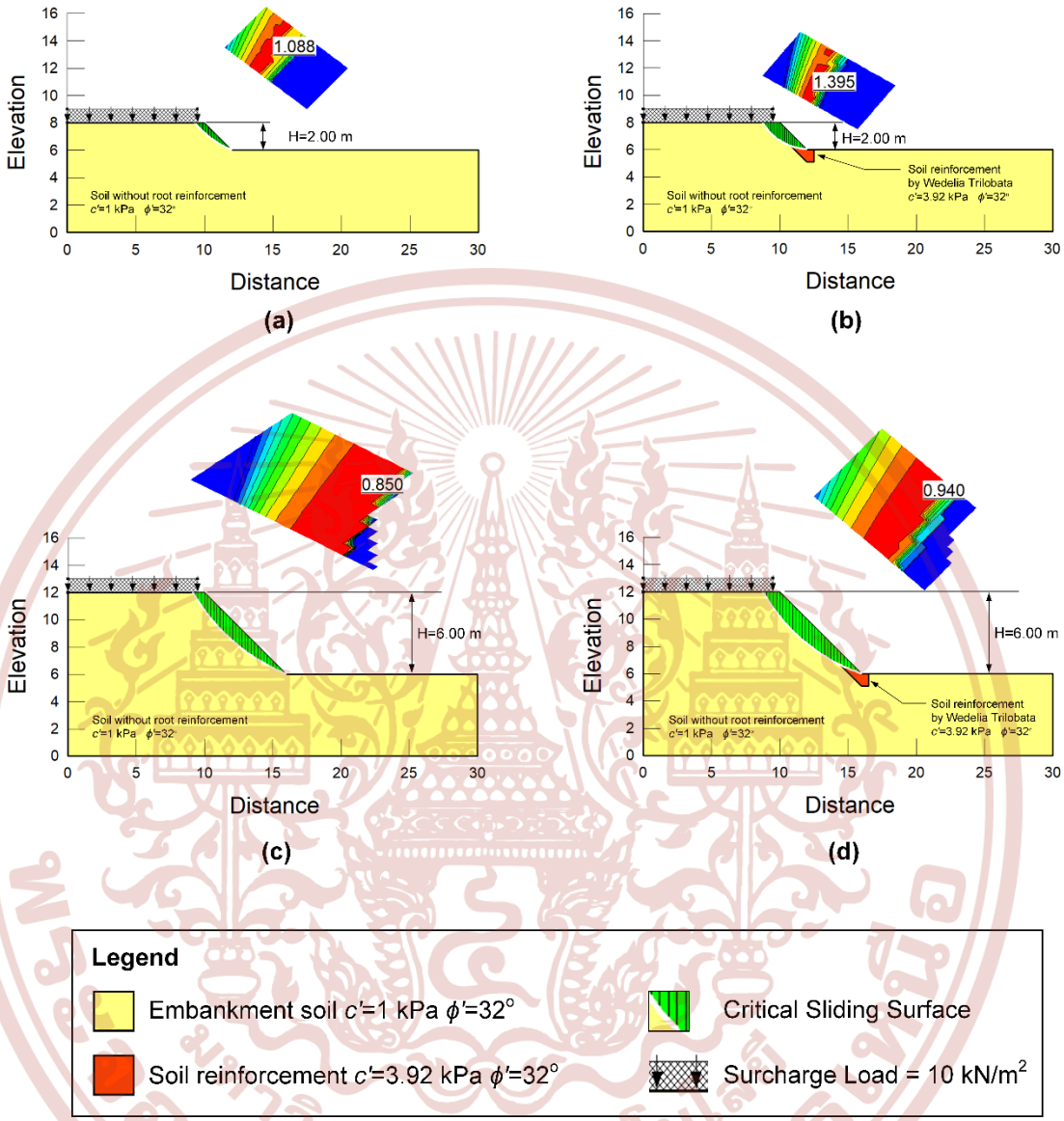


FIGURE B-10 Slope analysis results soil without roots and soil with roots.

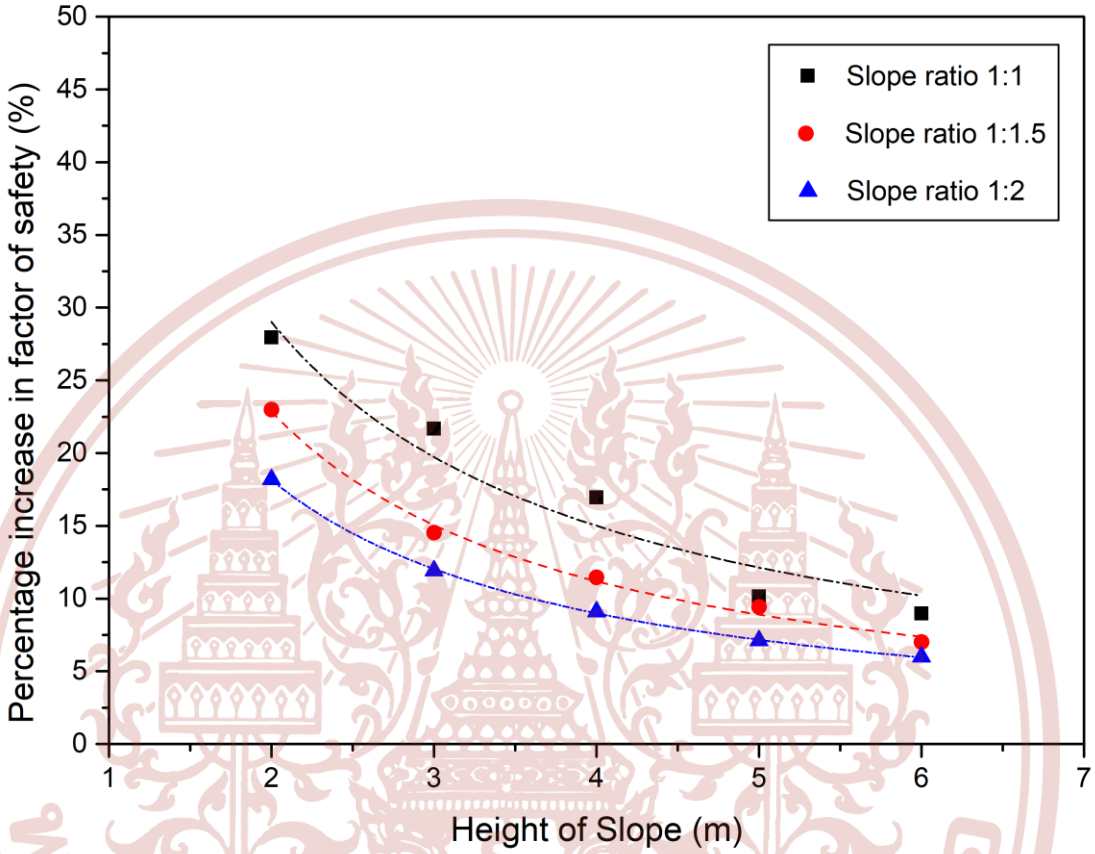


FIGURE B-11 Percentage increase in factor of safety for slopes reinforced with W. trilobata at varying slope ratios and heights.

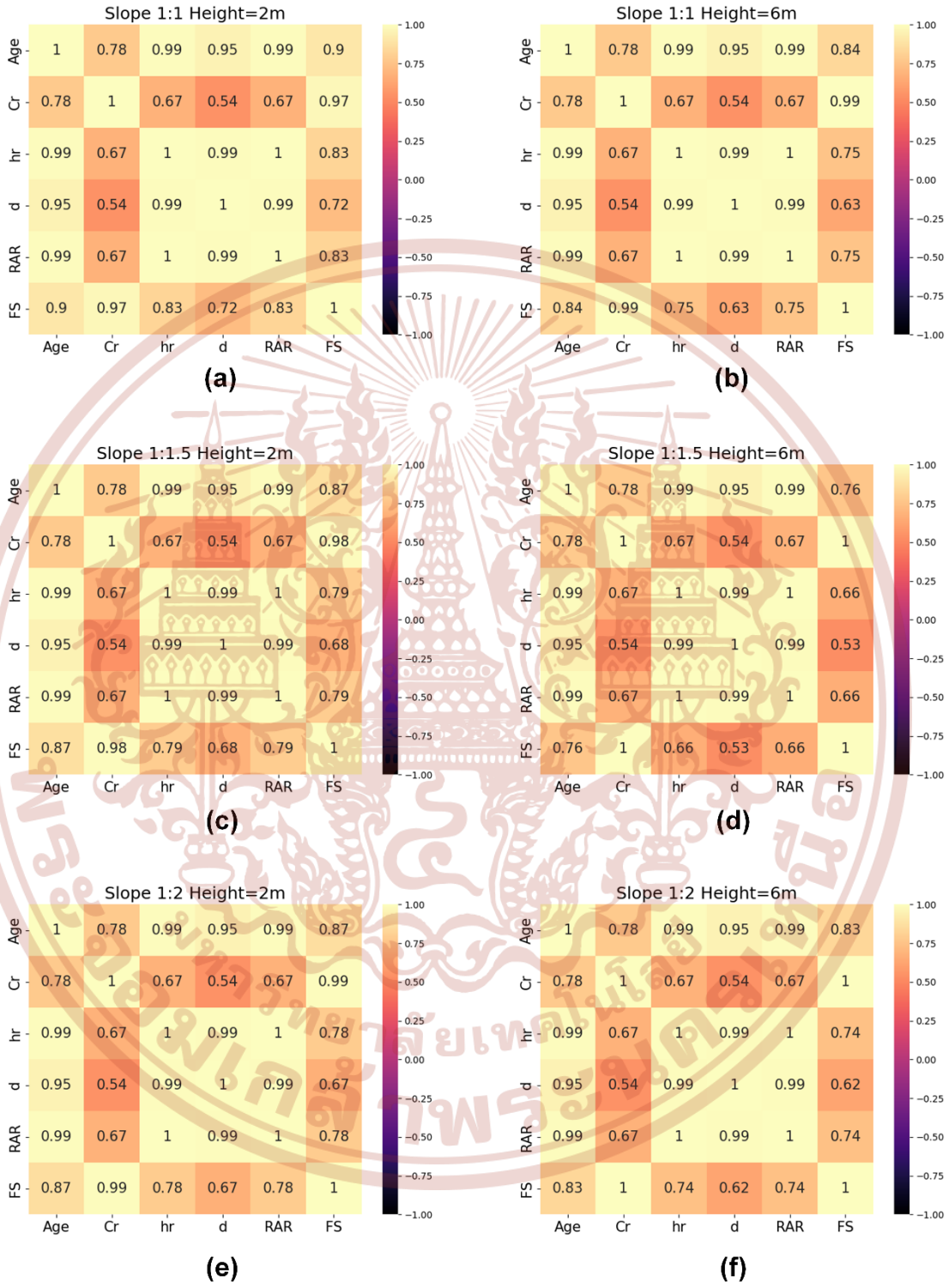


FIGURE B-12 Correlation (heat map diagram) between various effective parameters on the FS

APPENDIX C

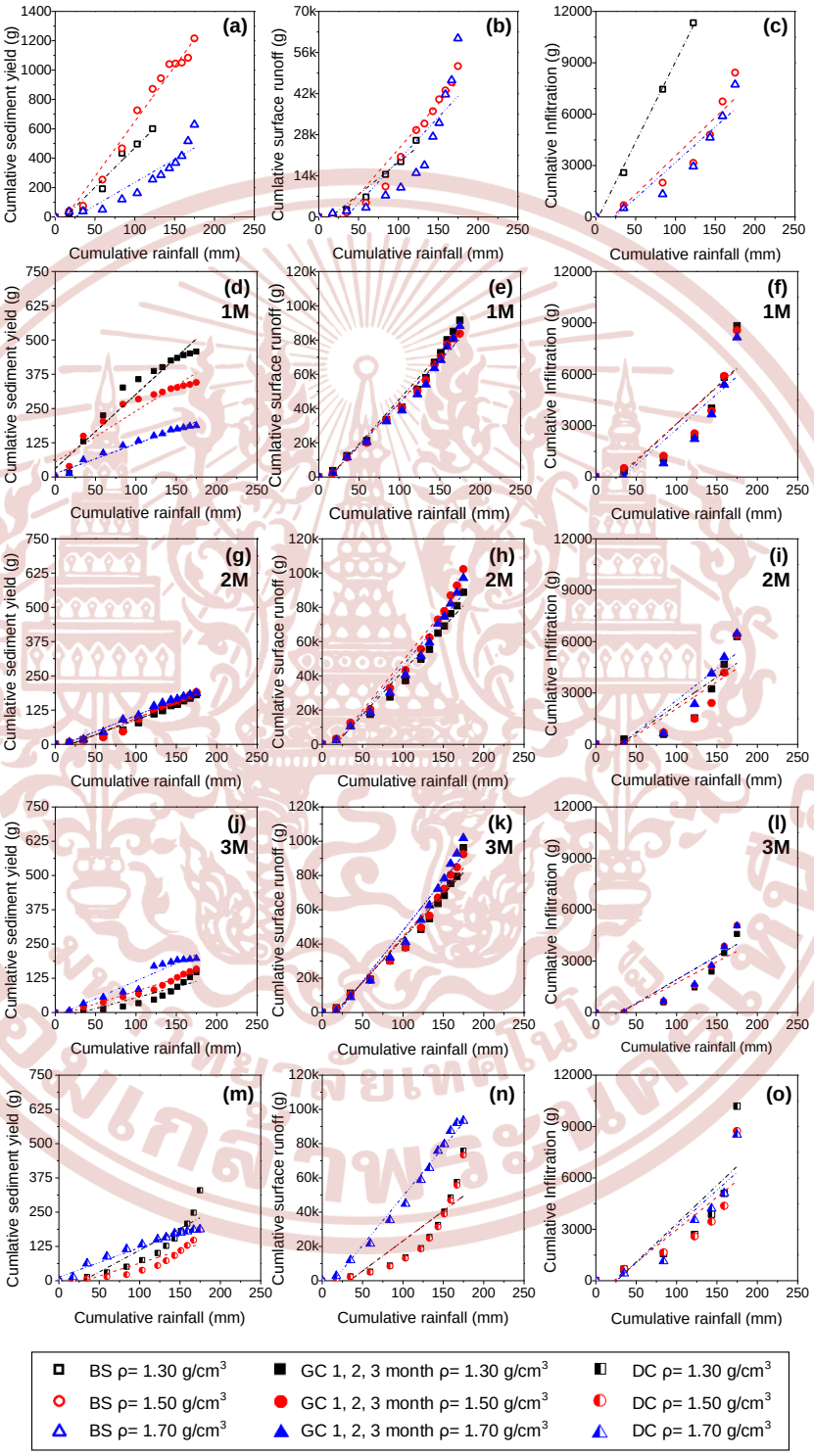


FIGURE C-1 Summary of cumulative erosion result in each rainfall event

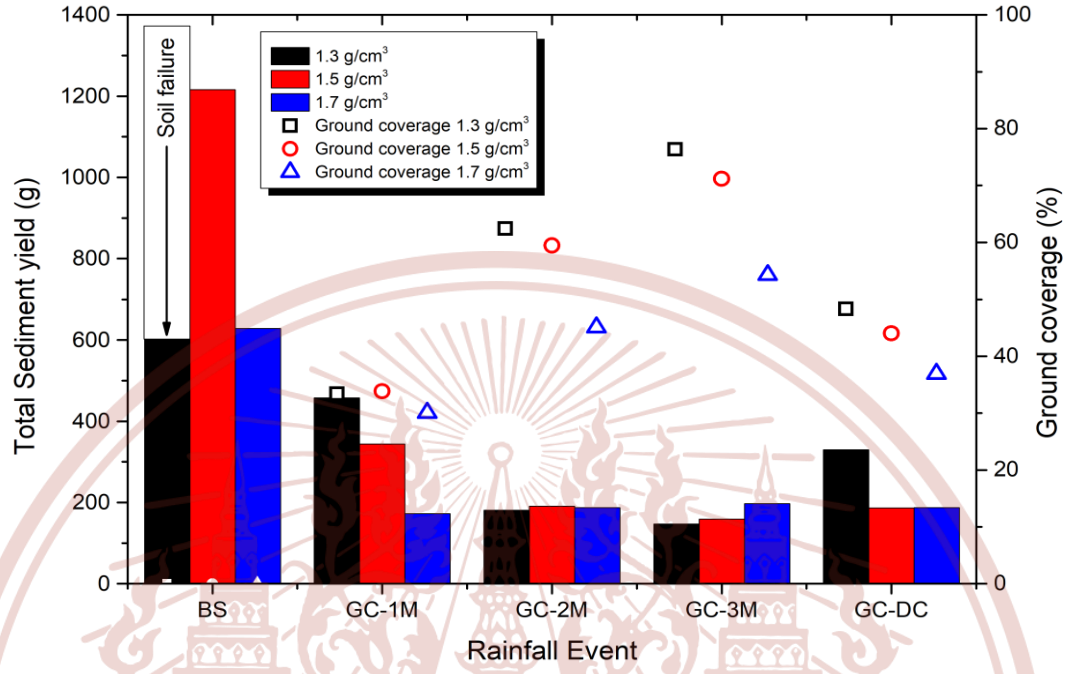


FIGURE C-2 Total Sediment yield with Ground coverage in each rainfall event

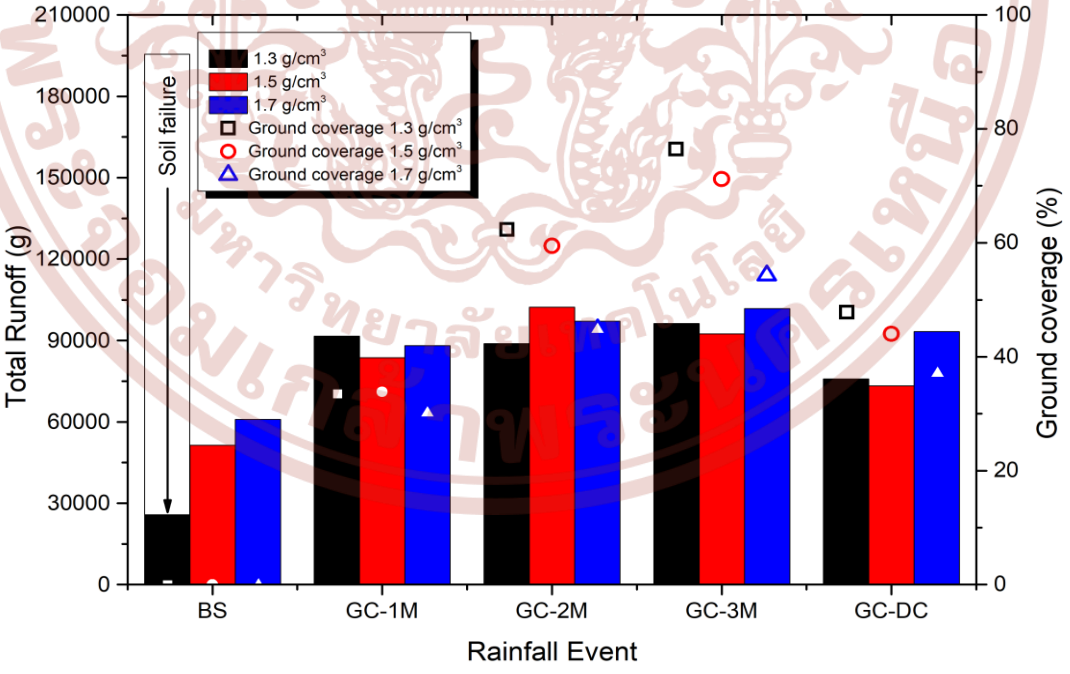


FIGURE C-3 Total Surface runoff with ground coverage in each rainfall event

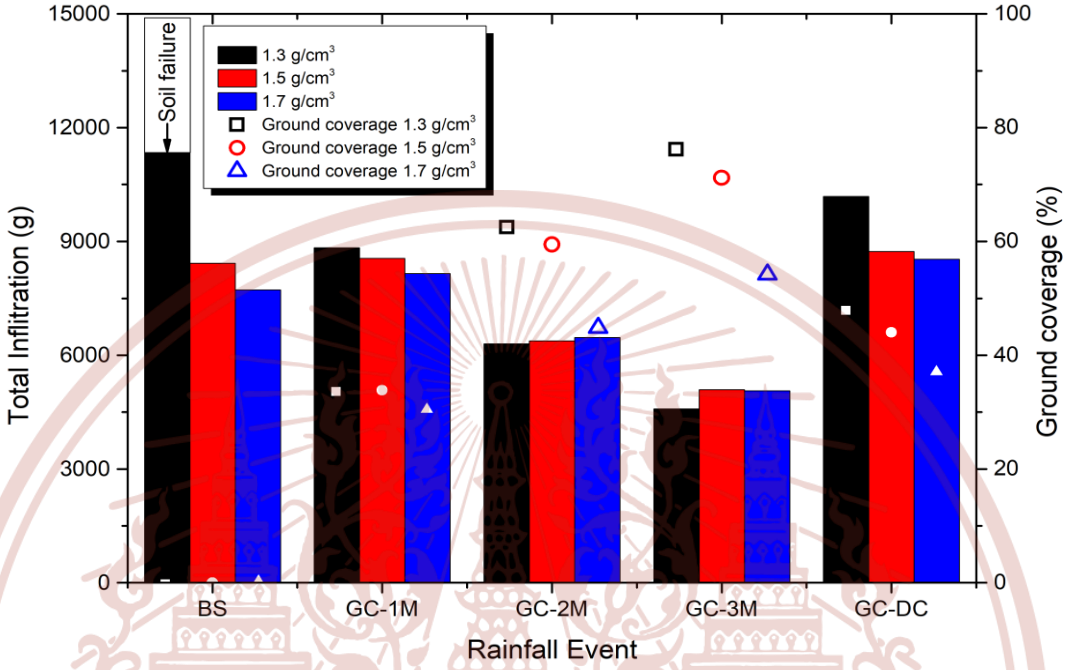


FIGURE C-4 Total Infiltration with Ground coverage in each rainfall event

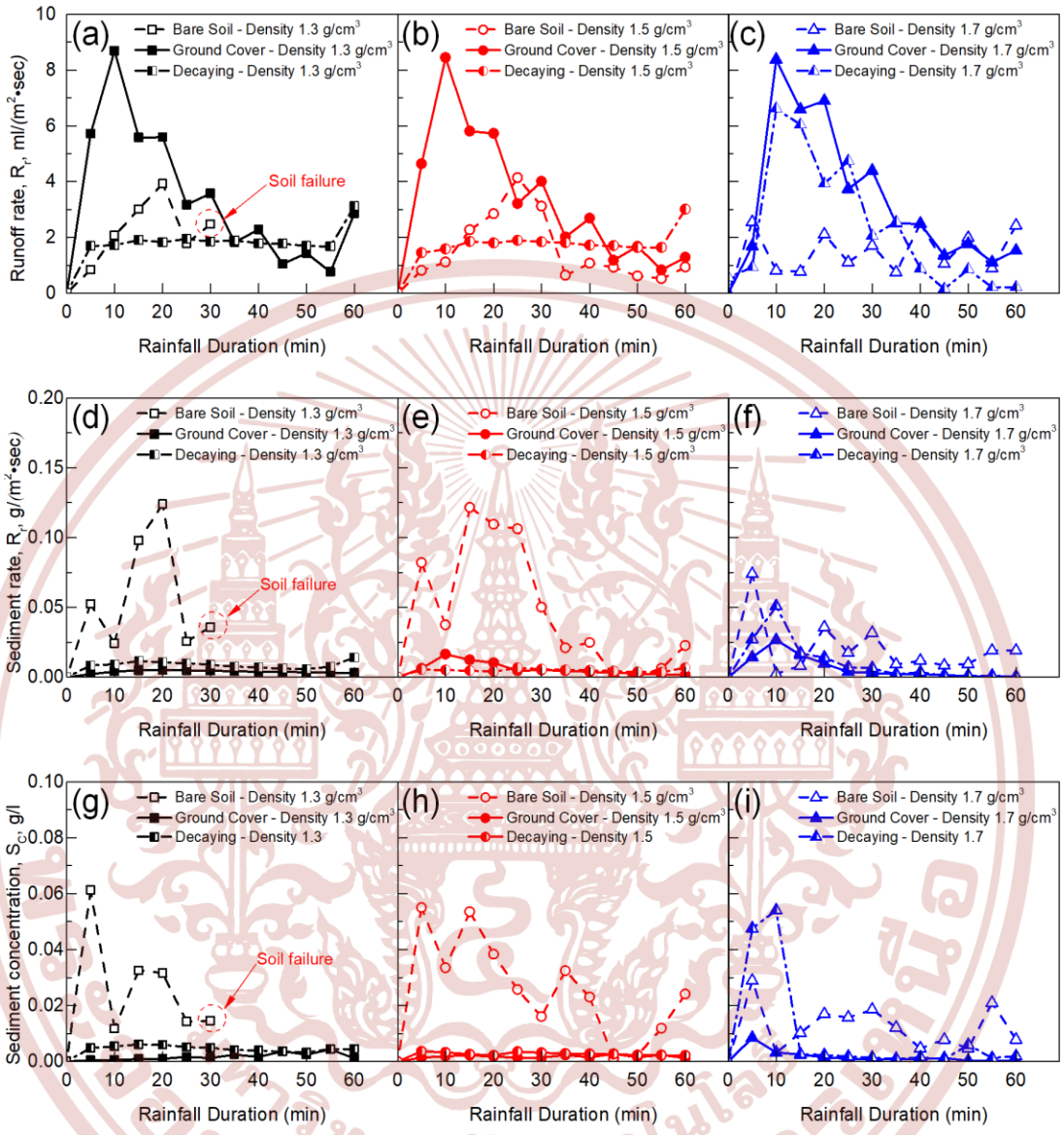


FIGURE C-5 Runoff rate and Sediment rate compared with Bare soil and Groundcover

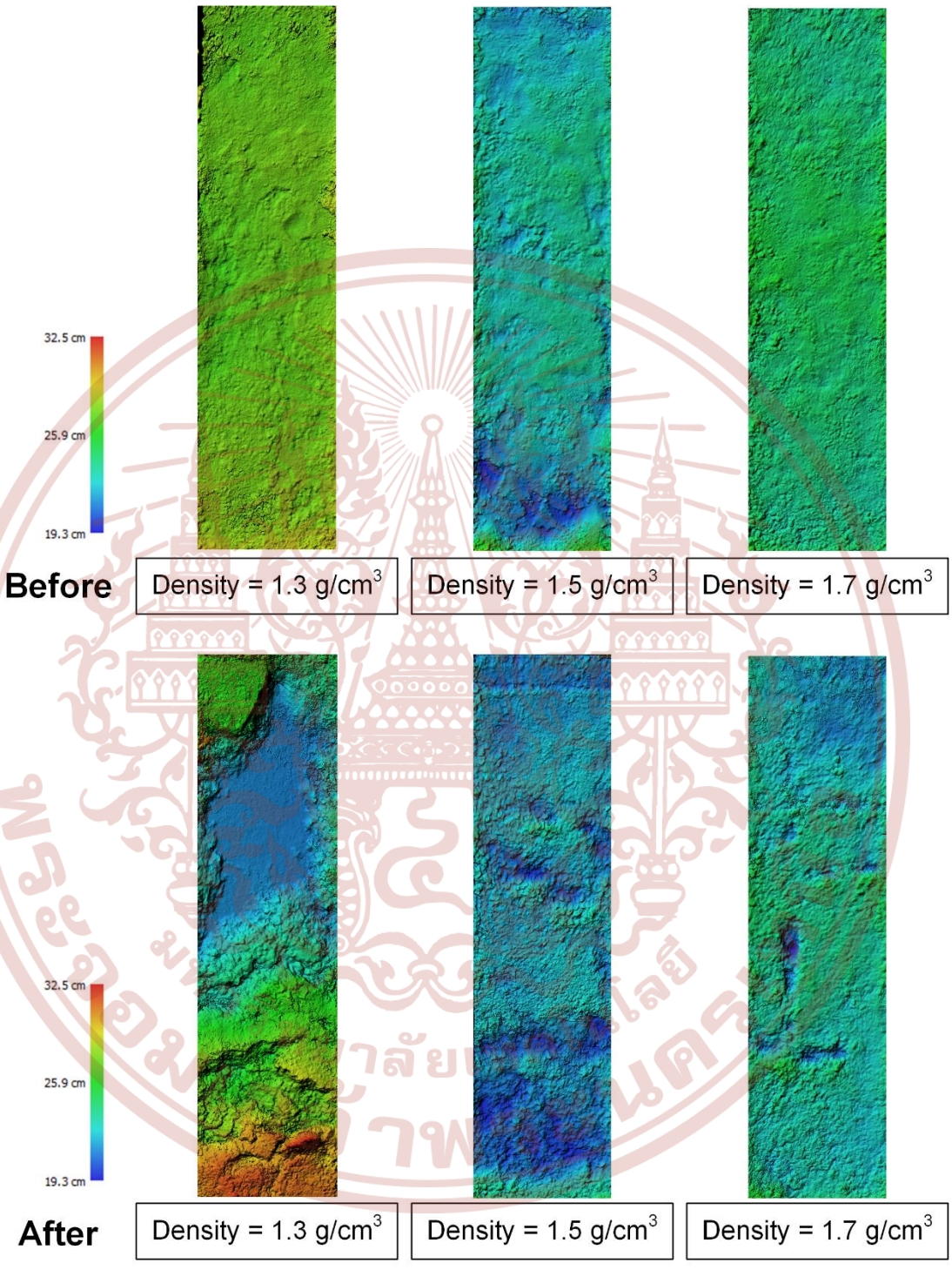


FIGURE C-6 DEM characteristics of the erosion process bare soil (Before-after)

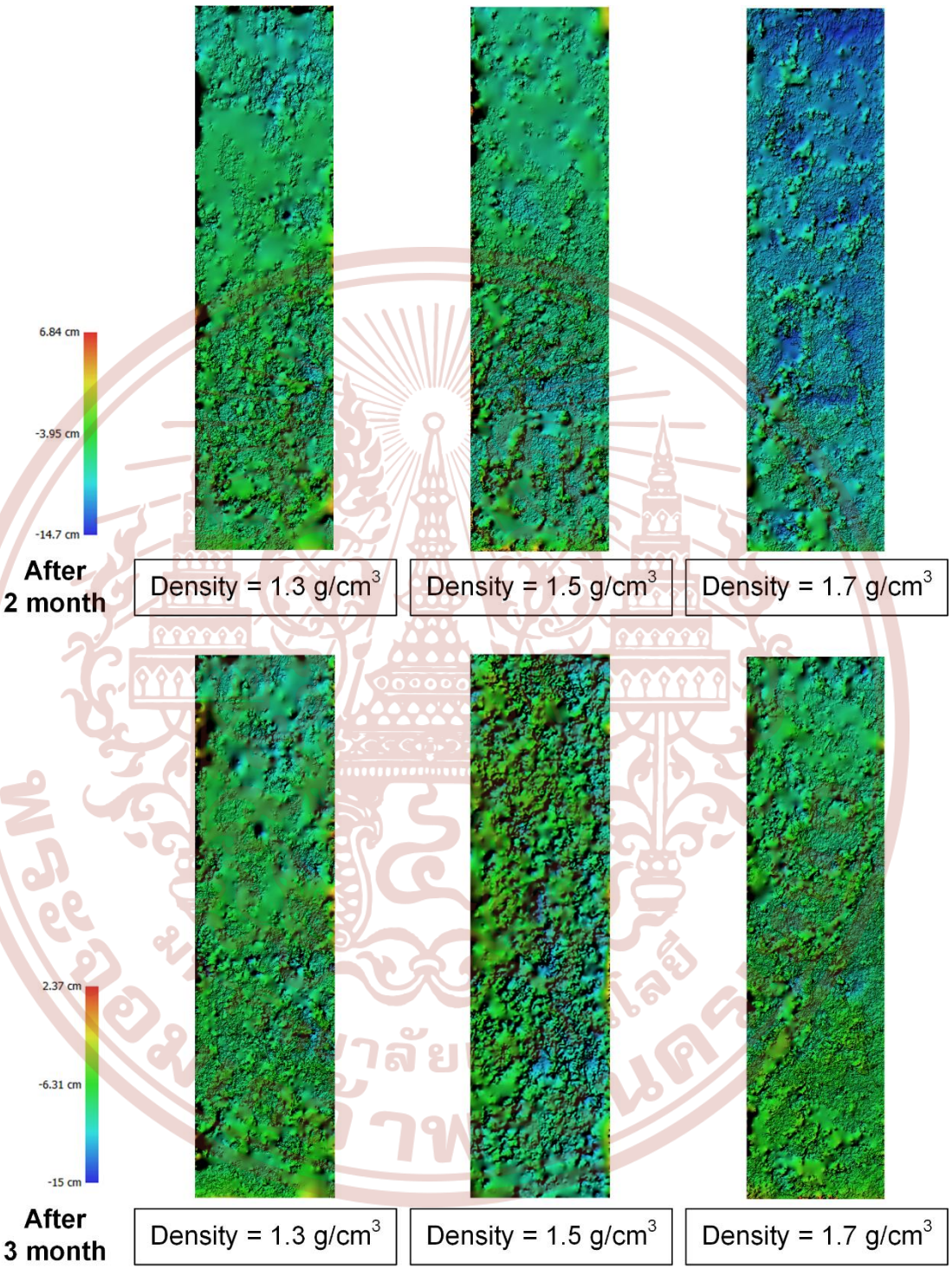


FIGURE C-7 DEM characteristics of the erosion process groundcover (2 and 3 months)

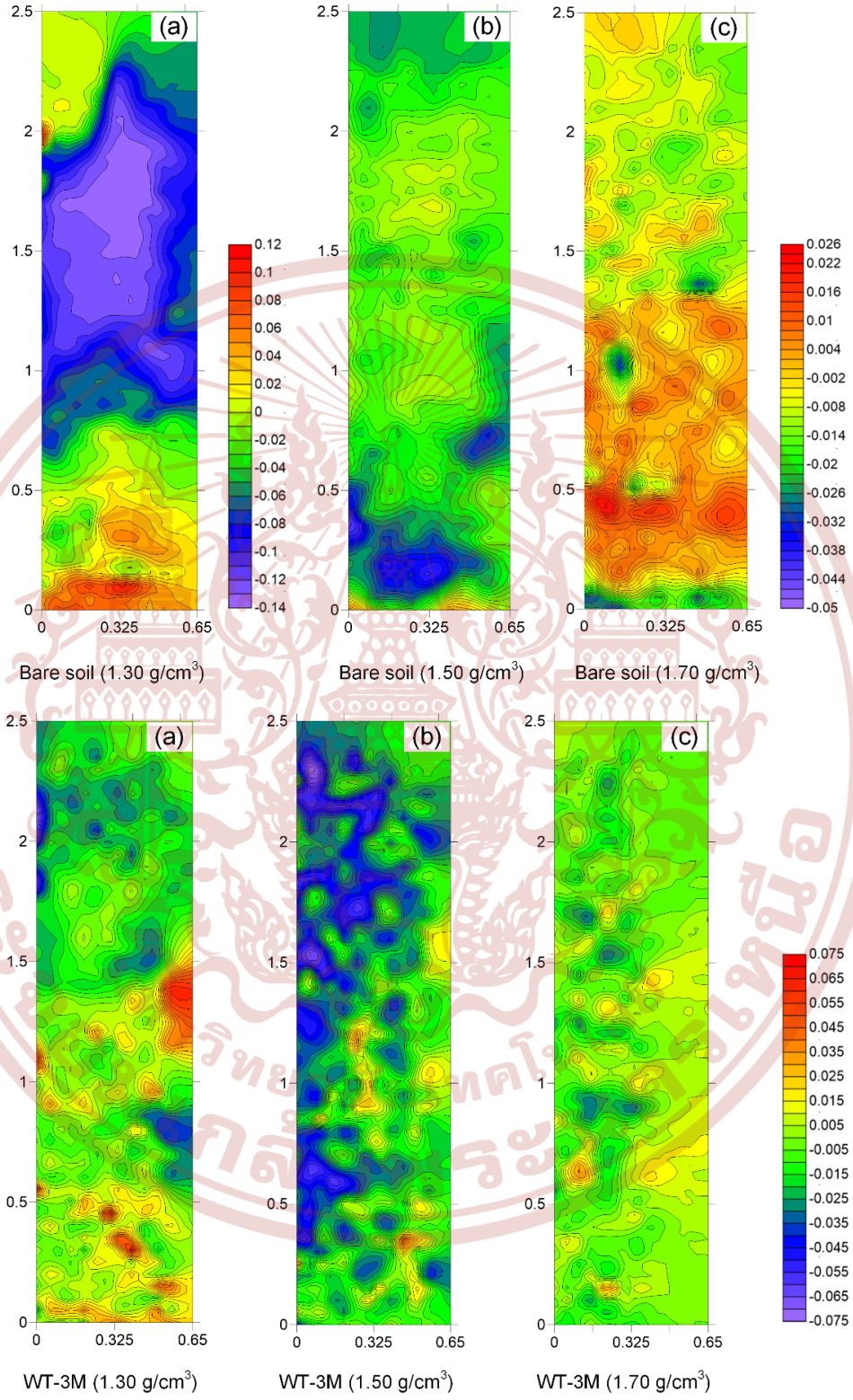


FIGURE C-8 Difference elevation form DEM

VITA

Name	Chinnakrit Ounjai
Thesis Title	Protecting embankments from erosion using Wedelia trilobata
Major Field	Geotechnical
Biography	Bachelor of Civil Engineering and Education King Mongkut's University of Technology North Bangkok (2020)

พระจอมเกล้าพระนครเหนือ
มหาวิทยาลัยเทคโนโลยี